FILTRATION OF ALUMINIUM
THEORY, MECHANISMS, AND EXPERIMENTS

BY

FREDE FRISVOLD

This thesis is submitted to the University of Trondheim, The Norwegian Institute of Technology, Department of Metallurgy, in partial fulfilment of the requirements for the degree of Dr. Ing.

December, 1990

NTH-Trykk
1991

PREFACE

The author - employed by SINTEF - wishes to acknowledge the financial support of this work by the Royal Norwegian Council for Scientific and Industrial Research under project number MT 10.01.18513 and by Hydro Aluminium a.s. and by Elkem Aluminium ANS.

The plant studies were carried out at the Lista plant. The Sunndal plant has performed the PoDFA analysis. The author is grateful for technical support and assistance.

Dr. Eirik Bathen is thanked for the careful metallographic analysis of the sampling filters from the Lista campaigns. Dr. Stein Tore Johansen has given me a number of helpful suggestions and discussions, and is acknowledged for this. The help during experiments and proof-reading of this thesis from Mr. Per Bakke is appreciated.

Most of all I am in debt to my supervisor Dr. Thorvald A. Engh whom through his guidance has brought me a long step forward as a researcher. I also feel that I have gained confidence and thereby ability to bring forward new ideas from working with him.

It should also be mentioned that parts of Chapters 1, 4, and 6 of this thesis have already been published as conference proceedings:

1. F. Frisvold, "Melt filtration", Aluminium Melt Refining - Theory and Practice, Melbourne, July 10-12, 1989
2. F. Frisvold, T.A. Engh, and E. Bathen, "Measurement of filtration efficiency of an Alcoa 528 filter", Light Metals 1990, Anaheim, February 19-22, 1990
3. F. Frisvold and T.A. Engh, "Measurement of efficiency of bed filters, Modelling", Symposium Stranggießen, Bad Nauheim, November 15-16, 1990

Trondheim, December 1990

Frede Frisvold

Frede Frisvold

Table of Contents

LIST OF SYMBOLS

A	- projection of collector normal to the mean particle flow direction
A	- cross section available for flow
A	- surface area
A	- projected area of the filter in the flow direction
A	- contact area between melt and refractories and top slag
A(x,r)	- number of inclusions deposited per unit volume melt and unit filter depth
A_i^σ	- surface area occupied by one mole of species i
A_v	- vertical projection of the collector
A_s	- collector surface area
a	- inclusion radius
a_s	- specific surface area (surface area per unit volume melt)
a_i	- activity of component i in the bulk phase
a_i^σ	- surface activity of component i
b	- ratio between the projected area normal to the particle velocity and the surface area
$b_2 = \frac{A_1 n_1}{A_1 n_1} - \frac{f_1}{f_2} e^{\frac{\Delta E^\sigma}{RT}}$	- parameter in surface tension model
c	- number of particles per unit volume melt
c(x,r)	- number of inclusions with radius r per cubic meter at depth x
$c_0(r)$	- number size distribution of inclusions per unit volume melt entering the sampling filter
c_i'	- concentration of component i in bulk phase 1
c_i''	- concentration of component i in bulk phase 2
c_0	- number concentration of inclusions entering the filter
c	- concentration of inclusions
c_L	- inclusion concentration at volume element outlet
c_0	- inlet inclusion concentration
$\Delta[\%C]$	- driving force for diffusion of carbon
$\vec{\vec{D}}$	- diffusion tensor
D	- diffusion coefficient

D - geometrical quantity defined on Figure 2.10

d_p - particle diameter

d_c - collector diameter

E - filtration efficiency

$\overline{E}$ - mean filtration efficiency

ΔE_{tot} - energy gain resulting from liquid metal withdrawal

ΔE_{lf} - the energy difference on the disk shaped area of the filter where liquid metal withdraws

ΔE_{lp} - the energy difference on the disk shaped area on the particle where liquid metal withdraws

ΔE_{lv} - the energy required for the formation of the cylindrical liquid metal surface

F - force pressing particle against the wall

F - London-van der Waals force

F^{σ} - Helmholtz free energy in the surface layer

F_D - drag force

F_L - mean lift force

f - friction factor (for packed bed)

f(a) - number size distribution of inclusions in the melt

$f_N(r)$ - number of inclusions per unit volume and unit size range

$f_{\sigma}(a)$ - number size distribution of inclusions deposited

f^{σ} - Helmholtz free energy per surface area

$f_i^{\sigma} = \frac{a_i}{[\%i]^{\sigma}}$ - activity coefficient at the surface

f_i - activity coefficient of component i in the bulk

ΔG^0 - free energy of adsorption

g - acceleration of gravity

H - Hamaker constant

H - filter thickness

H - filter depth

H - depth of sampling filter

H_s - geometrical quantity defined on Figure 2.10

h - distance of separation

h_j - height of the disk where measurements at depth j are assumed to be valid

$I(\beta_c, \theta)$ - measure of the volume flow at distance β_c at different angles θ from a cylinder

$I(\beta_s, \theta)$ - measure of the volume flow at distance β_s at different angles θ from a sphere

$[\%i]^\sigma$ - mass percent of component i at the surface

[%i] - mass percent of component i in the bulk

$\vec{j}$ - diffusion flux

K - kinetic parameter

K_C - kinetic parameter associated with capture

K_A - kinetic parameter associated with release

k - coefficient for transfer of particles

k - constant

k_c - mass transfer coefficient for carbide

k_t - mass transfer coefficient for removal

k_r - coefficient of re-entrainment

L - volume element length

L - length of packed bed

L - length of rod/cylinder

m_i - mass of component i

$N_A(r)$ - number size distribution per square meter melt

$N_V(r)$ - number size distribution per unit volume melt

n - cast number

n - number of measurements

n - rate expression order

n - number of recirculations

n - number of units

$\vec{n}$ - normal unit vector

n_i - number of component i in the bulk

n_i^σ - number of component i in the surface layer

n_j - number size distribution per square meter melt at depth j

O	- wetted perimeter
p	- probability of collision
p_i	- probability of collision with row i
$\overline{p}$	- mean probability of collision
p	- pressure
p_{atm}	- atmospheric pressure
$p\Delta V$	- the pV work against the surrounding pressure
Δp	- pressure drop
$\dot{q}$	- volume flow in cubic meter per second
R	- radius of tube
R	- collector radius
R	- radius of rod/cylinder
R	- molar gas constant
$R_H = \frac{A}{O}$	- hydraulic radius
R_s	- geometrical quantity defined on Figure 2.10
R_L	- radius of particle
r	- inclusion radius
r_c	- critical carbide inclusion radius
r_{met}	- metallic radius of element
r_p	- particle radius
Δr	- increase in inclusion radius due to salt
S	- surface of control volume V
S_n	- adjusted standard error
s	- standard deviation
s_n	- adjusted root mean square deviation
s^σ	- entropy per surface area
T	- temperature
t	- time co-ordinate
U_∞	- approach velocity (superficial velocity)
U_∞	- free-stream velocity
U_s	- settling velocity

x

$U(\theta)$ - ideal velocity in potential irrotational flow past a cylinder/sphere

u - particle velocity relative to collector

$\vec{u}$ - particle velocity

u_j - velocity components (u_1 = u, u_2 = v, u_3 = w)

u_c - critical velocity

u_p - velocity in plugging pathways

u_{np} - velocity in non-plugging pathways

u_r - relative velocity of particle with respect to fluid

u_f - fluid velocity in viscous sublayer

$u(\theta)$ - velocity in the boundary layer

V - control volume

V_f - volume of fluid

V_s - volume of solids constituting the filter

V - filter volume ($V = V_s + V_f$)

V - volume of melt

V(a) - volume of inclusion of size a

v - particle velocity

v - fluid velocity

W - adhesion energy

W - weight of melt

X - monolayer units

x - spatial co-ordinate

$x = \frac{R_L}{H_s}$ - dimensionless distance

x_j - spatial co-ordinates (x_1 = x, x_2 = y, x_3 = z)

x_i - mole fraction of component i in the bulk phase

y - spatial co-ordinate

y - distance from surface of cylinder/sphere

z - spatial co-ordinate

Greek symbols:

α - constant

α - wetting angle on inclusion

β - constant

β - wetting angle on filter

$\beta_c = \frac{y}{R}\sqrt{\frac{2U_\infty}{\nu}}$ - dimensionless distance from cylinder surface

$\beta_s = \frac{y}{R}\sqrt{\frac{3U_\infty}{\nu}}$ - dimensionless distance from sphere surface

$\Gamma_i = \frac{n_i^a}{A}$ - surface coverage of component i

δ - constant

ϵ - porosity

ϵ_i' - crosschemical potential of component i in bulk phase 1

ϵ_i'' - crosschemical potential of component i in bulk phase 2

ϵ_j - fraction of melt measured at depth j

η - collection efficiency

η_1 - collision efficiency of first collector

η_2 - collision efficiency of second collector

$\eta_{collision}$ - collision efficiency

η_i - collision efficiency due to interception where boundary layer has been taken into account

$\eta_{i,pot}$ - collision efficiency due to interception assuming potential flow

$\eta_{adhesion}$ - adhesion efficiency

$\eta_{i,sphere}$ - collision efficiency due to direct interception for a sphere

$\eta_{g,sphere}$ - collision efficiency due to sedimentation for a sphere

$\eta_{i,rod}$ - collision efficiency due to direct interception for a rod/cylinder

$\eta_{g,rod}$ - collision efficiency due to sedimentation for a rod/cylinder

η_g - collision efficiency due to sedimentation

$\eta_{g,1}$ - collision efficiency due to sedimentation at first collector

$\eta_{g,2}$ - collision efficiency due to sedimentation at second collector

η_{tot} - total collision efficiency (both gravity and interception)

θ - angle on cylinder/sphere

θ - wetting angle (contact angle)

θ - fraction of inclusions deposited

$\kappa = A_1^q / A_2^q$ - ratio

λ_0 - filter coefficient for the initial period

λ - filter coefficient

μ - (dynamic) viscosity ($\mu = \rho \cdot \nu$)

μ_i^s - chemical potential of component i in solid phase

μ_i^l - chemical potential of component i in liquid phase

μ_i^σ - chemical potential of component i in the surface layer

$\mu_i^{\sigma,0}$ - chemical potential of component i in the surface layer in the reference state

μ_i' - chemical potential of component i in bulk phase 1

$\mu_i'^{,0}$ - chemical potential of component i in bulk phase 1 in the reference state

μ_i'' - chemical potential of component i in bulk phase 2

ν - kinematic viscosity

ρ - constant

ρ - density

ρ_c - carbide moles per unit volume in aluminium carbide inclusion

ρ_m - melt density

$\Delta\rho$ - density difference between particles and fluid

σ - number of particles deposited per unit volume filter

σ - retained inclusion volume

σ_{np} - retained inclusion volume in non-plugging pathways

σ_{p} - retained inclusions in plugging pathways

σ_{sv} - interfacial tension between solid and fluid phase other than melt (usually vacuum)

σ_{lv} - interfacial tension between the two fluid phases (usually the surface tension of the melt)

σ_{sl} - interfacial tension between solid and melt

σ_{lv}^{p} - surface tension of one-component system

σ_{sl}^{p} - interfacial tension of one-component system

σ_{sl} - interfacial tension between filter and melt

σ_{sv} - surface tension of filter

σ_{pl} - interfacial tension between particle and melt

σ_{pv} - surface tension of particle

τ - normalized time

ψ - stream function

ABSTRACT

A common problem in the aluminium foundry is inclusions. Inclusions are particles in the melt that in the casting may have serious detrimental effects on machinability and physical properties.

The most effective, known, method to separate inclusions from melt is to send the melt through a mechanical filter prior to casting. A number of different kinds of mechanical filters exist. They can roughly be divided into "cake"-filters and deep-bed filters. Cake filters capture the inclusions by forming a cake of inclusions in front of the filter. Deep-bed filters entrap the inclusions down into the filter thereby attaining a higher capacity (lower pressure drop). Deep-bed filters have been studied here.

The filtration efficiency of a filter is deduced from first principles. An equation is proposed that takes 3-dimensional effects into account. A basic assumption is that the filter can be described in terms of a unit collector. For this collector the collection efficiency is calculated. The collection efficiency is the product of the collision efficiency and adhesion efficiency. The collection efficiency is related to the filtration efficiency through an equation involving geometrical quantities (volume of filter, specific surface, porosity, etc.) and flow velocities.

To determine the collection efficiency a water model experiment was designed. Near buoyant particles were used. They had a mean settling velocity of 0.06 cm/s. In order to make certain that the adhesion efficiency was 100% the particles were covered with a sticky coating. The 2-dimensional model filter consisted of 50 rods placed symmetrically in a matrix. Cylindrical and square rods were used, only one type at a time. A known number of particles were sent through the filter and the number of particles deposited on each collector (rod) were counted. Flow velocities from nearly zero to slightly above 1 cm/s were used.

It was found that at flow velocities less than about 0.6 cm/s, the mechanism controlling deposition is sedimentation. At flow velocities above 0.6 cm/s direct interception takes over. This is verified from theoretical calculations where the boundary layers have been taken into account. The square collectors gave a slightly higher filtration efficiency than the cylindrical. This might be due to their sharp edges and thereby larger back eddies.

The flow was observed to be laminar up to roughly 0.6 cm/s. After that the streamlines started to mix. At higher flow velocities the flow seemed to be in a transition regime resembling turbulence.

Industrial measurements of the filtration efficiency of an Alcoa 528 deep-bed filter have been made. It was found that:

The number size distribution of inclusions (Al_4C_3) can be determined metallographically from sampling filters employing image analysis. For the melts studied this distribution was found to be a decreasing exponential function of size (in the size-range studied).

For an Alcoa 528 filter the filtration efficiency as a function of particle size has been determined. As expected the efficiency increases with inclusion (Al_4C_3) size. The filtration efficiency obtained may be explained as removal of particles by interception with the filter grains.

It is felt that understanding the adhesion and the phenomena leading to adhesion between particle and filter immersed in melt is the key to a proper understanding of the problem of re-entrainment and filter long term behaviour.

Therefore a theoretical model for the effect of dissolved elements on the surface tension and interfacial tension has been developed and calibrated against measurements found in the literature. With knowledge concerning three fundamental handbook quantities the effect of metallic elements on the surface tension of aluminium and interfacial tension between aluminium and alumina is determined. These quantities are metallic radius, electronegativity, and the surface tension of the pure added element.

1 INTRODUCTION

1.1 Detrimental effects of inclusions in metal

Non-metallic impurities in the metal are a familiar problem in foundries. They affect in many ways the appearance, quality and properties of the castings as well as reducing yield of saleable castings and foundry productivity. In the modern foundry industry it is essential to produce clean metal in order to achieve the quality required by customers. The highest standards of cleanliness can only be achieved by good practices including the use of filtration.

Inclusions can have a catastrophic effect upon machining results and cutter life. The cost associated with downtime and lost cutters can exceed the casting selling price by a large multiplying factor (Groteke 1983). It thus becomes imperative that clean metal be present on a routine basis in even the simplest commercial casting, if machining or secondary operations are performed.

Groteke (1983) has illustrated that even though the total amount of shrinkage associated with solidification is independent of metal cleanliness, the type and quantity of each shrinkage formation can be changed dramatically by the presence of oxides. The major difference rests in the amount of pipe and sponge type shrinkage forms. Both are significantly increased by the presence of oxides and a major effect could be anticipated upon riser feeding efficiency and casting yield.

Removal of the high melting compounds and contaminants has been observed to confer a significant benefit upon fluidity of the metal. Diecasters using a filtering system have reported significant reductions in misruns and related defects from use of filtered metal (Groteke 1983).

Removal of inclusions from a melt will only have a minor direct impact upon the level of dissolved gas present in any liquid bath. A second indirect benefit is noticed that is usually more significant: removal of inclusions takes away nucleation sites for gas to congregate at upon solidification. Without these sites being present, the gas that is precipitated from solution will commonly diffuse through the melt and into the atmosphere. Thus, a higher level of gas can be tolerated in a production melt without visible evidence of porosity in the final product. The benefits are noticed both on machined surface and upon x-ray examination of castings (Groteke 1983).

Inclusions in the cast product cause problems in subsequent fabrication operations, and in service for products such as wheels. The inclusion causes a reduction in formability locally acting as a stress raiser. In some cases such as can sheet or foil the inclusion may be larger than the section size causing a hole. Hard inclusions can score the extrusion die which then creates die lines on the surface of the extrusion. Defects in can bodies can occur during the forming of flange. Pinholes in foil can be caused by cast in inclusions or rolled in particles which fall on the sheet. Typical pinhole rates are around 100 holes per square meter in foil less than 10 microns in thickness (Grandfield 1989).

Removal of inclusions has also been shown to allow increased pouring rates and lower pouring temperatures in commercial foundry operations (NN 1988).

In conclusion, inclusions have an adverse effect on surface appearance, a severe effect on mechanical properties and on machining.

1.2 Available filter systems

With the ever increasing demand for higher quality aluminium products it has been necessary continually to develop better processes for the removal of inclusions from molten aluminium. This has led to the development of several different filter systems mainly of two kinds: mechanical filters and filters combined with gas purging.

In this section some of these filters will be reviewed. Not only will mechanical filters be looked upon, but also floatation and settling units. Only particle removal in the unit is of principal interest here although some of the units are primarily designed to remove solved elements with inclusion removal only a side-effect.

Settling in casting furnaces

Inclusions with a density greater than the aluminium melt may sediment due to gravity. Martin et al. (1988) have studied settling phenomena in casting furnaces and concludes with: 1) settling, unless otherwise upset, proceeds for many hours; however, its rate varies in time in such a way that it remains productive only for approximately the first two hours. 2) Experimental measurements with in-line analysis techniques do not fit the predictions of a simple "static" model based on Stokes' law; in particular the predictions for the relative behaviour of stationary and tilting furnaces are not verified. Predictions based on the addition of an inclusion capture mechanism to a well-mixed bath correspond better with the observed trends. 3) It appears that the contributions of metal currents inside the casting furnace are significant.

Alcoa 622

One to three reactor chambers in series where small bubbles are produced by revolving nozzles. Inclusions are removed by floatation.

AlPur

The major element of the AlPur system is a counter-current gas injection by the AlPur rotary mixer (Hicter 1983). Inclusions are removed by floatation.

SNIF (Szekeley et al. 1976)

In the reactor chamber small bubbles produced by upright nozzles are intensively mixed with the melt. Inclusion removal is by floatation.

Hydro impeller

A specially designed impeller produces well dispersed small bubbles. The impeller is smooth and giving minimal surface disturbance. Inclusion removal is by floatation.

MINT

In the MINT system, metal from the furnace enters the "swirling tank" reactor through a tangential port at the top and flows in a helical fashion downward. Small bubbles of treatment gas are injected into the melt by high pressure nozzles located in the conical section at the bottom of the reactor. These bubbles float upward counter-current to the metal flow.

The metal leaves the reactor trough a port at the bottom, flows horizontally through a cross-over section and up a riser pipe to the filter bowl. Non-metallic inclusions are removed by a disposable ceramic foam filter of SELEE structure located in the bowl.

DUFI: Durchlauffilter (Bornand and Buxmann 1985)

The DUFI filter is almost always used with petrol coke, and equipped with porous graphite diffusers ensuring the counter flow degassing of the metal in the presence of argon inert gas. Corundum is used to ballast the coke (i.e. prevent it from floating to the surface of the melt). Its filter bed ensures a very homogeneous distribution of gas and facilitates intimate contact with the flow of liquid metal. It also has the effect of capturing non-metallic inclusions by mechanical filtration.

Alcoa 94 and Alcoa 181

Some of the first systems to receive significant foundry application are the Alcoa 94 and 181 processes. The Alcoa 94 process is a filtration method where molten aluminium alloy is passed through a packed bed of tabular alumina balls and flakes. Inclusions are removed by mechanical filtration. When coupled with a countercurrent degassing device, the method is identified as the 181 process. According to Groteke (1983): "This equipment has until recently been the most widely used production filtration device".

Alcoa 527, 528, and 469 (527+528) (Blayden and Brondyke 1974)

The Alcoa 469 process utilizes two types of filter beds, primary and secondary, with a mixture of chlorine and nonreactive gas flowing counter-current to the metal passing through each unit. The most important part of the system is the unit with the packed bed filter which has been designated the primary unit. A roughing type filter, designated the secondary unit, is generally employed upstream of the primary unit to extend process life. Both units remove sodium, hydrogen, and inclusions, with the primary unit having the higher efficiency. Used as single separate units the primary unit is designated the Alcoa 528 filter and the secondary unit the Alcoa 527 filter.

Packed refractory beds serve both to distribute the fluxing gas mixture and act as impingement type filters. The filter bed may be of any refractory inert to molten aluminium, sufficiently hard to prevent fracturing or powdering during use, and of specific gravity greater than molten aluminium. The material must also be inert to chlorine at the operating temperature of molten aluminium. Of the several materials which suit these requirements, tabular alumina is the preferred refractory, although any form of calcined alumina may be considered.

Multicast (Neff and Stankiewics 1986)

Multicast filters is comprised of refractory grains such as alumina, silicon carbide, or other ceramics, and a proprietary binder. A variety of pore sizes, metal flow and filtration characteristics can be developed in the filters by appropriately

varying the grain size, or grit, of the material. The bonded particle filter exists in three configurations, (1) the cartridge filter, (2) the plate filter, and (3) Multicast Filtration System.

The Multicast filter assembly is a three dimensional bonded particle filter combining the larger surface area of a cartridge filter with the ease of use of a plate filter. By constructing a filter assembly of vertical closed end filter tubes cemented to a filter media sealing plate, filter surface area is more than three times that of the plate filter with the same dimensions of the sealing plate. It is designed for large tonnage metal throughput before clogging. Inclusions are removed by mechanical filtration.

Ceramic foam filters (Selee, Sivex)

Ceramic foam filters are produced by impregnating reticulated polyurethane foam with ceramic slurry plus binder followed by subsequent burn out of the organic foam material and firing of the ceramic to produce a high temperature bond. This gives a filter with a porous open cellular structure. While the ceramic foam filter is light weight and easy to use, it can have certain disadvantages, such as lack of sufficient strength for a given application, excessive porosity in order to achieve a desired level of fine particle filtration. In general they exist for single use - that is a ceramic foam filter is spent on a single cast and then must be replaced with a fresh filter for the next cast. Inclusions are removed by mechanical filtration.

Metaullics filters

The cartridge filter consists of a rigid media composed of a glass bonded aggregate of mullite ($3Al_2O_3 \cdot 2SiO_2$). In one application, the filter consists of cartridge tubes that are connected to a front dip-out well of the holding furnace. Metal is filtered by passing through the cartridge, with the residue forming a cake on the outside of the tube. When the throughput falls below a required production level, or the head difference to achieve flow reaches a critical height, the unit is shut down and the cartridge elements replaced as an assembly.

Electromagnetic purification (Barglik and Sajdak 1985)

An electromagnetic force is produced in a conductive medium such as the melt, but not in a non-conducting medium such as non-metallic inclusions. It can be stated that the influence of electromagnetic field upon the mixture conducting liquid metal - non-metallic inclusions is selective. The statement is not very precise, but convenient for a simplified description of the effect of an electromagnetic field on the removal of non-metallic inclusions.

In most electromagnetic devices the removal of non-metallic inclusions is mostly obtained in two ways: 1) Through causing the so-called effect of the apparent change of the weight density of the liquid metal. 2) Through causing the movement (transportation) of liquid metal for example using electromagnetic channels.

1.3 Previous work

1.3.1 Classification of mechanical filters

Apelian et al. (1982) have carried out a property evaluation of commercially available porous media for molten metal treatment. The media were classified into the following five generic types: ceramic monoliths, unbonded ceramic particulate, ceramic foams, bonded ceramic particulate, and woven ceramic fiber. No attempt was made to evaluate the filter performance in terms of inclusion removal efficiencies.

For tabular media it was implied that production variables have a significant effect on the surface characteristics since the sample of fine tabular medium supplied did not possess the highest number of micropores, surface area or pore volume. A similar finding was that manufacturing techniques can affect both the surface area as well as the mediums surface porosity. The structural characterizations showed that filters within one generic type have vastly differing surface properties.

1.3.2 Fundamental filtration mechanisms

Possible capture processes in filtration are:

Mechanical retention. The inclusions get stuck in pores smaller than their own size. Not to be considered in depth filtration, but typical for cake filtration.

Sedimentation or floatation. If the particles have a density different from that of the liquid, they are subjected to gravity and their velocity no longer is that of the fluid; thus, by sedimentation or floatation they can meet the filter medium.

Inertia. Still owing to their apparent weight, the particles cannot follow the same trajectories as the fluid, they deviate from the streamlines (when the directions of the trajectories change suddenly) and can be brought into contact with the filters internal surface.

Hydrodynamic effects. Owing to the non-uniform shear field and/or the non-sphericity of particles, hydrodynamic effects may occur; these effects cause a lateral migration of suspended particles which may be brought into contact in this way with the retention sites.

Direct interception. Even with exactly the same density as the fluid, the particles would not be able, owing to their size, to follow the smallest tortuousities of the streamlines of the carrier fluid and they will thus collide with the walls of the convergent areas of the pores.

Diffusion by Brownian motion. The particles diffuse and can reach areas which are not normally irrigated by the suspensions, and they are retained there.

Effects of turbulence. The Brownian deposition is only of importance for very small (submicron) particles. When the particles become larger, their Brownian diffusivity becomes smaller, but their inertia will result in an increased slip velocity between particles and the turbulent fluctuations of the fluid. The increased slip velocity resulting from increased particle inertia is then believed to be the mechanism which drives the heavy particles through the quiet "laminar sublayer" which is located extremely close to the wall.

1.3.3 Effects of liquid inclusions and salts

Apelian et al. (1986) have conducted water model filtration experiments to visualize the flow behaviour (capture, coalescence, migration, and release) of liquid inclusions in a filter medium, and to quantify the effect of hydrodynamics and filter surface (wetting) characteristics on filtration behaviour.

Three regimes of filter performance were identified:

1. Total capture: during this regime all incoming liquid inclusions are captured by the filter, and there is no release.

2. Onset of release: liquid inclusions are released by the filter, and the amount released increases with time. Here the filter is operating in a transient mode, partial release is taking place.

3. Coalescer mode: there is no capture by the filter. All inclusions which enter the filter also exit. In this regime the filter acts as a coalescer by causing 100% release of inclusions.

At low Reynolds numbers (< 20), most inclusions are preferentially captured near the entrance to the filter, and slowly coalesce into a layer which then progresses toward the exit of the filter. At high Reynolds numbers (30) the inclusions are captured randomly throughout the filter. As the bulk melt velocity increases, the volume of liquid inclusions captured in the bed prior to release decreases. There exists a maximum bulk velocity where the critical hold-up is zero.

The two most critical operating parameters are: bulk melt velocity and wettability of the filter with respect to liquid inclusions.

At low inertial forces, i.e. low Reynolds numbers, when the filter bed is non-wetting, a larger volume of inclusions are captured than in the case when the inclusions wet the filter. The reverse is observed at high inertial forces, i.e. high Reynolds numbers.

Brant et al. (1971) have investigated a "sticky" ball filter consisting of 3/4 inch balls. The flux consisted of KCl and NaCl pre-fused in approximately eutectic proportions with a small addition of CaF_2. During the two weeks of operation there were not at any time signs of partial releases of inclusions from the filter. The coated balls themselves had become covered by adherent inclusions. The effect of the flux on the inclusion removal seems to be favourable in this case.

It was found unnecessary to pre-coat the balls, since the upper balls in the degassing chamber acquired an adequate flux coating in the first few minutes of operation; thereafter the coating spread slowly over the rest of the balls so that, as the initially coated areas became covered with inclusions, new areas of sticky surface was generated.

Eady et al. (1986) have investigated the effects of flux on the filtering efficiency of ceramic foam tiles, and it was shown that the flux commonly used with molten aluminium can seriously reduce the effectiveness of ceramic foam filters from 70% to 30%.

They suggest that the reduction in efficiency can be explained by a reduced effective density of the flux covered inclusions. Flux is almost always found to be associated with inclusions. This agglomeration therefore reduces the effective density of the (flux covered) inclusion. Because the density of the

flux-contaminated inclusion is closer to that of the carrier molten metal, there is less likelihood of the inclusion leaving the metal stream, by gravitation effects.

The association of flux with inclusions also appear to alter the surface energy and the shape of the inclusion. It is well known that molten salts of the type used in fluxes are easily wetted by aluminium (Grjotheim et al. 1982) which indicates a very low interfacial energy for flux or flux coated inclusions in the melt. The effect of this is two-fold. The reduced interfacial tension of the molten aluminium around an inclusion in contact with the filter surface would have the effect of reducing the force with which it is held onto the surface. In addition, the less compact shape of a flux-contaminated inclusion would enable it to be washed away from the filter surfaces more easily, due to larger drag forces.

1.3.4 Mathematical models of filtration

Engh et al. (1986) and Rasch (1987) developed a model based on fluid mechanics and adhesion forces for a single spherical collector. Finally single collectors are put together to constitute a packed bed. This model is divided into three steps:

Step 1 is the calculation of the probability of collision between a single spherical collector and a (spherical) particle - the collision efficiency.

Step 2 is the calculation of the probability that the particle stays with the collector after touching it - the adhesion efficiency.

Step 3 Single collectors are put together to form a packed bed with a known geometry. Scaling up from one to many collectors is done by using a volume density of collectors.

The collision efficiency is calculated in three different flow regimes; potential flow, boundary layer flow, and viscous flow, and for different capture processes; direct interception, inertia, sedimentation, and Brownian diffusion.

The model does not include the effect of inclusions previously deposited, i.e. it is a theory describing the initial filtration efficiency. Likewise, in its present formulation, it does not consider re-entrainment.

Initial filter efficiencies were calculated by Conti (1983) using Payatakes, Tien, and Turian's (1973, 1974) method of trajectory calculations.

Gauckler et. al (1985) take the probability of adhesion to be 1. Using an unit cells model in the flow direction, the filter bed can be divided into a series of identical unit elements. It is assumed that the concentration of particles at the beginning of each cell is uniform perpendicular to the flow.

Thus it is possible to calculate the probability of particle attachment by distinguishing particles on trajectory lines colliding with the cell-surface from particles which simply pass through the cell.

The filter efficiency E can be calculated from the trajectory lines (Conti and Jacob 1984), and the filter coefficient for the initial period λ_0 can be calculated from E:

$$E = 1 - e^{-\lambda_0 \cdot H}$$

H being the filter thickness.

The calculation of the trajectory lines along which inclusions follow in suspension requires solution of the Navier-Stokes equation. As the model has been formulated it only applies to the case where the direction of gravity settling is the same as the direction of flow.

An excellent review of depth filtration in general is given by Herzig et al. (1970). Mass balance equations for the particle or for the carrier fluid give the same results. The first application of a mass balance combined with a rate equation to describe deposition in melts was performed by Apelian and Mutharasan (1980). The kinetic rate expression relating the change of retained inclusion volume, σ, with respect to time is:

$$\frac{\partial \sigma}{\partial \tau} = K \cdot c^n$$

where τ is a normalized time, K a kinetic parameter, and n a rate expression order. c is the concentration of inclusions.

n is assumed to be 1 as in chemical reaction kinetics of the 1^{st} order.

Eckert et al. (1984) have solved this system of equations, with appropriate boundary conditions, with the result

$$c_L = c_0 e^{-\lambda \cdot L}$$

where c_L is the inclusion concentration at the volume element outlet, c_0 is the inlet inclusion concentration, λ the filter coefficient, and L the volume element length.

Eckert et al. believe that filter releases (of inclusions) occur when the filtrate interstitial velocity exceeds a threshold limit, and that experimental evidence strongly indicates that this is the case for the long term behaviour of aluminium melt filters.

They propose a method of improving the kinetic model by including a release term in the kinetic rate expression. The expression should be of the form

$$\frac{\partial \sigma}{\partial \tau} = K_C c - K_A$$

where K_C is the kinetic parameter associated with capture and K_A is the kinetic parameter associated with release.

Gruesbeck and Collins (1982) have an even more sophisticated theory where they use a concept of so-called plugging and non-plugging pathways (pores):

$$\frac{\partial \sigma_{np}}{\partial \tau} = \alpha \ (u_{np} - u_C) \ \sigma_{np} + \beta \cdot c$$

$$\frac{\partial \sigma_p}{\partial \tau} = (\delta + \rho \sigma_p) \ u_p c$$

where α, β, δ, and ρ are constants and u_C is a critical velocity.

Experiments confirm their theory for flow in the proximity of a well-bore.

1.3.5 Measurements

Steel versus aluminium. From a fluid mechanical point of view the main difference is that in steel melts the inclusions have lower density than the molten metal while it is vice versa in aluminium melts. So where we talk of sedimentation in aluminium it would be reasonable to think of floatation in steel. Else the difference in density and viscosity between aluminium and steel is taken care of if the Reynolds numbers are kept equal.

A much more important difference is due to the high temperature of steel melts. According to Apelian et al. (1985) the deposited inclusions rapidly sinter to the filter surface and act as new filter sites for further capture of inclusions. This is not believed to be the case for aluminium melts.

Keeping this in mind we can exploit experiments performed on steel to learn something about aluminium filtration. Ali et al. (1985) have carried out experiments (with laboratory prepared melts) in refining of aluminium and steel melts using multicellular extruded ceramic filters. The inclusion removal efficiency, E, was obtained by spectrographic analysis, of all inlet and outlet samples for TiB_2 content in the case of aluminium melts. The inclusions in the steel melts were Al_2O_3. The differences between the steel-system and the aluminium-system can be explained by the combined effects, sintering in steel and re-entrainment in aluminium.

Initial filtration of a clean filter for steel or aluminium can be described by the same models. But the time-evolution is different as the geometry of the steel-filter probably changes permanently due to sintering.

It should be mentioned that there may be re-entrainment in steel melts also if the timescale of sintering is long compared to the timescale of re-entrainment.

Experiments. A laboratory investigation of aluminium filtration through deep-bed and ceramic open-pore filters was conducted by Mutharasan et al. (1981). Three different deep-bed filter configurations were used also allowing a direct comparison between a ceramic foam filter and a deep-bed filter. Tracer inclusions were TiB_2. It was indicated that the efficiency of each filter decreases from nearly 100% at low melt velocities to a lower limiting value with increasing melt velocity. The efficiencies of the ceramic foam and tabular medium differed distinctly in the respect that the efficiency versus interstitial melt velocity declines less rapidly for the deep-bed than that of the ceramic foam. It should be noted that the measured efficiencies are characteristic of short-time behaviour of the beds.

Gauckler et al. (1985) have also investigated the initial filter efficiencies of different filter types experimentally using TiB_2 particles as tracers in aluminium melts. Efficiencies increase for decreasing melt velocities. Efficiencies are higher for fine filters (55 ppi) and lower for coarser filters (30 ppi).

Deposition of inclusions down through a sandwich type foam filter has been studied by automatic image analysis by Bathen and Engh (1988). The experiments were performed at an aluminium foundry.

The melt quality was "pure aluminium". TiB_2 only was added, as a grain refiner. The main object for image analysis was aluminium carbide particles in the melt.

Ceramic sandwich filters were placed in a case between runners from the holding furnace to a casting machine. The filter type was SELEE MULTIPORE filter, with two layers of different pore sizes referred to as 20 and 40 pores per inch respectively, designated 20/40 filter. A series of charges were filtered, each about 50 tons.

The distribution of particles by depth showed the following characteristics: Relatively wide depth regions in both the 20 ppi and 40 ppi parts of the filter show an apparent constant amount of particles deposited. The content of particles is highest in the first regions of the two parts of the filter.

Bathen and Engh conclude that their results indicate that the "entrance regions" are the areas where removal of particles is most pronounced. They explain this as follows: When there is a radical change in the geometry of the filter, the boundary layers have to build up anew. It is then easier for the inclusions to penetrate the boundary layer and hit the walls of the filter medium. This is the case near the inlet and around the interface.

2 THEORY OF FILTRATION

2.1 Introduction

Inclusions moving through a filter can either collide with the filter surface or escape entirely. With a single-filter system the escaped inclusions will remain in the melt. If the inclusions touch the filter surface is determined by fluid flow and surface phenomena. On the other hand there is a certain possibility of re-entrainment of previously deposited inclusions. This is mainly a question of adhesion between inclusion and filter surface. Inclusions can of course be deposited in back eddies, but this is a highly unstable situation and probably does not contribute much to the removal. Back eddies may manifest themselves as a time delay mechanism.

In the following filtration will be looked upon as a two step process. Fluid mechanics will give a probability of collision (collision efficiency) and wettability and adhesion will determine a probability of adhesion (adhesion efficiency). The collection efficiency equals the product of collision and adhesion efficiencies. Re-entrainment would be a third step.

2.2 Fluid mechanics

From a macroscopic point of view only the pressure drop versus flow rate is of importance. On the other hand, to fully understand and utilize mechanical filtration a microscopic model is needed. A proper understanding of the deposition mechanisms gives a basis to further the understanding of the pressure drop (absolute value, time evolution, etc). In the following subsection we will start out by having a look at the "black box" approach to flow through porous media and then in the next subsections have a closer look at flow patterns and particle deposition inside a filter.

2.2.1 Pressure drop

In many applications in the aluminium industry today the metallostatic head at disposal is limited. Often 0.1 or 0.2 m of metal head must suffice to force the metal through the filter. Pressure drop initially depends on the properties of the fluid and the filter. As filtration proceeds the pressure drop becomes dependent also on the properties of particles deposited on or in the filter. If the particles are deposited on the filter it is said that we have "cake mode" filtration. In this case particles deposited previously act as a filter for the last particles approaching the filter. When the inclusions are deposited inside the filter we speak of deep-bed filtration. If the size of the inclusions are comparable to the filter pore size, cake filtration is inevitable. Even if the inclusions are one or two orders of magnitude smaller than the pore size, the section of the filter closest to the inlet gradually fills up so that the mechanism here more and more resembles cake-mode filtration.

Filter capacity is defined as the quantity of deposited particles which the filter is capable of accumulating before reaching a certain pressure drop (loss of metallostatic head). The filter capacity clearly depends on the type and size of the particles.

Problems with cake mode filtration is that it gives rise to a high pressure drop and a limited filter capacity. It can be shown that the pressure drop is caused essentially by the small inclusions, deposited only on the inlet surface of the filter.

If particles can be deposited on the walls inside a filter with collector dimensions much larger than the particles, the pressure

drop is drastically reduced. Also, if the total surface area within the filter is much greater than the inlet surface , filter capacity is much improved. Deep bed filters operate in this mode.

Generally speaking, there have been two main theoretical approaches for studying pressure drops through packed beds. In one method the packed column is regarded as a bundle of tangled tubes of weird cross section; the theory is then developed by applying results for single straight tubes to the collection of crooked tubes. In the second method the packed bed is visualized as a collection of submerged objects, and the pressure drop is calculated by summing up the resistances of the submerged particles (Ranz 1952).

The friction factor (or drag factor) f for the packed bed is defined as:

$$\frac{\Delta p}{\frac{1}{2}\rho U_\infty^2} = \frac{L}{d_c} \cdot 4f \tag{2.1}$$

in which d_c is the particle diameter and U_∞ is the "superficial velocity" (this is the average linear velocity the fluid would have in the column if no packing were present). L is the length of the packed bed. Δp is the pressure drop across the bed.

When the Blake-Kozeny equation for laminar flow and the Burke-Plummer equation for turbulent flow are simply added together the result is (Bird, Stewart, and Lightfoot 1960)

$$\frac{\Delta p}{L} = \frac{3.50}{12} \cdot \rho U_\infty^2 \cdot \frac{1}{\epsilon^2} \cdot \frac{1}{R_h} + \frac{25}{6} \cdot \frac{\mu}{\epsilon} \cdot U_\infty \cdot \frac{1}{R_h^2} \tag{2.2}$$

where the hydraulic radius, R_h , is defined as

$$R_h = \frac{\text{cross section available for flow}}{\text{wetted perimeter}} = \frac{A}{O} \qquad (2.3)$$

For a tube of radius R, $R_h = \frac{R}{2}$.

Rewritten in a dimensionless form Equation (2.2) is known as Ergun's equation. This equation represents an "analytical" solution, but it does have several deficiencies. The use of empirically determined parameters is a weakness. In particular, the parameters have been determined for beds of spherical and equal sized particles. There is no guarantee that the equation is valid for non-spherical particles.

Another approach to determine the pressure drop is to solve the Navier-Stokes equation numerically. Johansen and Anderson (1990) have done this for an Alcoa-528 filter.

2.2.2 Number balance

Engh has given an excellent discussion of inclusion removal from melts. The collision efficiency is defined as

$\eta_{collision}$ = number of particles that collide with collector per unit time / (number of particles per unit volume * cross-sectional area of collector normal to particle velocity * velocity of particles relative to collector)

If the particles have the same velocity as the melt, the definition reduces to

$\eta_{collision}$ = volume flow of melt containing particles that will collide with collector / volume flow approaching collector

A coefficient for transfer of particles, k, is introduced by defining it so that the number of particles transferred to the collector surface A_s per unit time is k*A*c - c being the concentration of inclusions. Engh has shown that the coefficient for transfer of particles is related to the collection efficiency η by

$$k = \eta \cdot u \cdot b \tag{2.4}$$

Here u is the particle velocity relative to the collector. b is equal to the ratio between the projected area normal to the particle velocity and the surface area. It has been assumed that removal is proportional to particle concentration and surface area. The efficiencies are interrelated by

$$\eta = \eta_{collision} \cdot \eta_{adhesion} \tag{2.5}$$

Assuming that a representative control volume, V, can be defined, the number of particles in V is:

$$\int\int_V\int (\sigma + \epsilon c)dV = \text{number of particles in control volume} \tag{2.6}$$

σ is the number of particles deposited per unit volume filter. ϵ is the porosity and c the number of particles per unit volume melt. The convective net flow of particles in/out of the control

volume is given by integrating over the control volume surface. The surface integral is rewritten in terms of a volume integral by employing the divergence theorem (Gauss);

$$\int_S \int \epsilon c(\vec{u}\cdot\vec{n})dS = \int_V \int \int \nabla\cdot(\epsilon c\vec{u})dV \qquad (2.7)$$

Here $\vec{u}$ is the particle velocity and $\vec{n}$ is the unit normal vector pointing out of the control volume. The diffusion flux is:

$$\vec{j} = -\vec{\vec{D}}\cdot\nabla(\epsilon c) \qquad (2.8)$$

$\vec{\vec{D}}$ is the diffusion tensor, and is assumed to be isotropic i.e. $\vec{\vec{D}} = D\cdot\vec{\vec{1}}$. The net exchange of particles in the control volume then becomes

$$\frac{\partial}{\partial t}\int_V \int \int (\sigma+\epsilon c)dV = -\int_V \int \int \nabla\cdot(\epsilon c\vec{u})dV - \int_V \int \int \nabla\cdot\vec{j}dV \qquad (2.9)$$

Or in a differential form:

$$\frac{\partial}{\partial t}(\sigma+\epsilon c) + \nabla\cdot(\epsilon c\vec{u}) - D\nabla^2(\epsilon c) = 0 \qquad (2.10)$$

Herzig et al. (1970) have considered both particle balance and liquid balance in the control volume and shown that both formulations lead to the same equation. This equation in x, y, z, and t is to complicated to be solved in general without employing a number of simplifying assumptions.

They found that Brownian motion always is insignificant with respect to bulk flow and is negligible in normal deep filtration conditions. A number of investigators support the view that Brownian diffusion is only of importance for particle radii less than 1 μm in fluids. Neglecting also turbulent diffusion Equation (2.10) then becomes

$$\frac{\partial}{\partial t}(\sigma + \epsilon c) + \nabla \cdot (\epsilon c \vec{u}) = 0 \qquad (2.11)$$

Normal conditions when filtering molten aluminium lead to the assumption

$$\sigma \gg \epsilon \cdot c \qquad (2.12)$$

This assumption is not valid before deposition has occurred at least once, i.e. $\sigma \geq 1 m^{-3}$. c is ordinarily of the order of 1 ppm or less. We will not attempt to describe the initial penetration of the filter by melt containing inclusions. Using (2.12) we get

$$\frac{\partial \sigma}{\partial t} + \sum_{j=1}^{3} \frac{\partial}{\partial x_j}(\epsilon c u_j) = 0 \qquad (2.13)$$

The particles leaving the melt are deposited on the collector and the particles leaving the collector are re-entrained by the melt. Using the subindex d for deposition and r for re-entrainment we get

$$\frac{\partial \sigma}{\partial t} = \left(\frac{\partial \sigma}{\partial t}\right)_d - \left(\frac{\partial \sigma}{\partial t}\right)_r - c \cdot \frac{\partial \epsilon}{\partial t} \qquad (2.14)$$

The first term can be expressed in terms of the coefficient for transfer of particles, k, given by Eq. (2.4):

$$\left(\frac{\partial \sigma}{\partial t}\right)_d = k \cdot a_s \cdot c \cdot \epsilon \tag{2.15}$$

where a_s is the specific collector surface and c the number concentration of inclusions.

Likewise it may be assumed that the re-entrainment can be expressed by a coefficient of re-entrainment, k_r:

$$\left(\frac{\partial \sigma}{\partial t}\right)_r = k_r \cdot a_s \cdot \sigma \tag{2.16}$$

The third term expresses the change in deposition due to previous deposition. The porosity ϵ is defined as

$$\epsilon = \frac{V_f}{V} = \frac{V - V_s}{V} = 1 - \frac{V_s}{V} \tag{2.17}$$

Here V_f is the volume of fluid and V_s is the volume of solids constituting the filter. V is the filter volume, $V = V_f + V_s$, and is a constant. Differentiation of Eq. (2.17) with respect to t:

$$\frac{\partial \epsilon}{\partial t} = -\frac{1}{V}\frac{\partial V_s}{\partial t} \tag{2.18}$$

The increase in the volume of solids is given by the coefficient for transfer of particles, k, and the decrease is given by the coefficient for re-entrainment, k_r. That is:

$$\frac{\partial V_s}{\partial t} = k a_s \int_0^\infty f(a) \cdot V(a) da - k_r a_s \int_0^\infty f_\sigma(a) \cdot V(a) da \qquad (2.19)$$

f(a) is the number size distribution of inclusions in the melt, $f_\sigma(a)$ is the number size distribution of inclusions deposited, and V(a) is the volume of inclusions of size class a.

Inserted in Eq. (2.17) this gives

$$\frac{\partial \epsilon}{\partial t} = -\frac{k a_s}{V} \int_0^\infty f(a) \cdot V(a) da + \frac{k_r a_s}{V} \int_0^\infty f_\sigma(a) \cdot V(a) da \qquad (2.20)$$

From the above discussion it is seen that deposition, re-entrainment, and the effect of previous deposition may be described mathematically in terms of some (unknown) parameters. Deposition can be determined via Eq. (2.4), but a description of re-entrainment presupposes that a value for the coefficient of re-entrainment may be found. For normal filtration conditions it is assumed that only deposition must be taken into account. Equation (2.13) then reduces to

$$k a_s c \epsilon + \sum_{j=1}^{3} \frac{\partial}{\partial x_j} (\epsilon u_j c) = 0 \qquad (2.21)$$

Most investigators assume that removal only depends on the major flow direction. u is supposed to be a mean velocity independent of x. In this case Eq. (2.21) reduces to

$$k a_s c + u \frac{\partial c}{\partial x} = 0 \qquad (2.22)$$

Inserting Eq. (2.4)

$$\eta a_s b c + \frac{\partial c}{\partial x} = 0$$

On integration:

$$\frac{c(x)}{c_0} = e^{-\eta a_s b x} \qquad (2.23)$$

where c_0 is the number of inclusions per unit volume melt that enters the filter. If the filter depth is H the filtration efficiency, E, is determined by

$$E = \frac{c_0 - c(H)}{c_0} = 1 - \frac{c(H)}{c_0} = 1 - e^{-\eta a_s b H} \qquad (2.24)$$

a_s is the specific surface area, or surface area collector per unit volume melt, i. e. :

$$a_s = \frac{A_s}{V_f} = \frac{A_s}{V_s} \cdot \frac{1-\epsilon}{\epsilon}$$

because $V_f = V \cdot \epsilon$ and $V = V_f + V_s$ giving

$$V_f = V_s \cdot \frac{\epsilon}{1-\epsilon}$$

Here A_s is the collector surface area. Inserting for a_s in Eq. (2.24) gives

$$E = 1 - e^{-\eta \cdot \frac{A_s}{V_s} \cdot \left(\frac{1-\epsilon}{\epsilon}\right) \cdot b \cdot H} \tag{2.24}$$

Returning to Eq. (2.21) letting $\vec{u}$ depend on the spatial co-ordinates we have

$$k a_s c \epsilon + \sum_{j=1}^{3} \frac{\partial}{\partial x_j}(\epsilon u_j c) = 0 \tag{2.21}$$

Now the coefficient for transfer of particles, k, depends on all three spatial directions, and we postulate that Eq. (2.4) is valid for every direction separately, giving

$$k = \sum_{j=1}^{3} \eta b u_j \tag{2.25}$$

b is equal to the ratio between the projected area normal to the mean particle velocity and the surface area collector. An isotropic filter medium has been assumed. We then get

$$\sum_{j=1}^{3} \left[\epsilon \eta b u_j a_s c + \frac{\partial}{\partial x_j}(\epsilon u_j c) \right] = 0 \tag{2.26}$$

Information about the flow field u_j is necessary in order to be able to solve this equation. Previously we used the assumption that there was a dominating flow direction and that the velocity in that direction was constant. This velocity was chosen in a

manner that took care of the volume flow (continuity fulfilled). In other words we were using an artificial "mean" velocity in one direction.

In order to determine the flow field the Navier-Stokes momentum equation and the continuity equation for the liquid phase must be solved. That is beyond the scope of this discussion. We instead postulate that there is a "mean" velocity in the x-, y-, and z-directions. There is of course no net flow in directions perpendicular to the major flow direction (here: x) for the filter as a whole, but in a porous medium the flow must follow conduits not only along the major direction, but also perpendicular to it. The flow along y- and z-directions will also contribute to the removal of inclusions and we take this into account by assigning separate collision efficiencies to each direction. Equation (2.26) then becomes

$$\sum_{j=1}^{3}\left[\epsilon\eta b u_j a_s c + \epsilon u_j \frac{\partial c}{\partial x_j}\right] = 0 \qquad (2.26)$$

The final assumption is that the concentration only depends on the major flow direction, i.e. x. We then get an equation which can be solved;

$$\frac{\partial c}{\partial x} = -\sum_{j=1}^{3} \eta b a_s c \frac{u_j}{u_1} \qquad (2.27)$$

Integration gives

$$\frac{c(x)}{c_0} = e^{-\sum_{j=1}^{3} \eta b a_s x \frac{u_j}{u_1}} \qquad (2.28)$$

The analogy with Eq. (2.23) is clear and we get a filtration efficiency, E (Eq. (2.24));

$$E = 1 - e^{-\sum_{j=1}^{3} \eta \cdot \frac{A_s}{V_s} \cdot \left(\frac{1-\epsilon}{\epsilon}\right) \cdot b \cdot H \frac{u_j}{u_1}} \qquad (2.29)$$

Summary of assumptions that led to Eq. (2.29)

1. Removal is proportional to particle concentration and surface area.

2. Brownian and turbulent diffusion are neglected.

3. $\sigma \gg \epsilon \cdot c$

4. Assumption 3 means that the equation is not valid before deposition has occurred.

5. The filter medium is homogeneous. And if 3-dimensional effects shall be taken into account it is isotropic also.

6. Velocities are assumed to be independent of spatial co-ordinates.

7. A major flow direction and "mean" flows in all three spatial directions can be defined.

8. Concentration only depends on the spatial co-ordinate in the major flow direction.

9. Deposition can be described by $k \cdot a_s \cdot c \cdot \epsilon$.

10. Re-entrainment is neglected.

11. The effect of previous deposition is neglected.

12. A coefficient for transfer of particles can be defined as

$$k = \sum_{j=1}^{3} \eta b u_j .$$

So far we have postponed discussing collision mechanisms and how to calculate the geometric quantities (A_s, V_s, b, etc.) for the filter medium. For a filter with a complicated internal geometry this may prove to be an intractable problem. The question then arises can the filter medium be described in terms of a "simple" unit filter medium or a unit collector?

2.2.3 Unit collectors

Unit collectors must exhibit the properties of the medium they are meant to describe, such as collection efficiency, porosity, and A_s/V_s-ratio and b. Implicitly this means that the flow field also must match, if the same collision efficiency is to be obtained.

In the literature a number of different unit collector models exist. Some exhibit internal flow and some external flow. The geometries differ significantly. The simplest external flow collector model is a sphere. For an isolated spherical collector

$$\frac{A_s}{V_s} = \frac{4\pi R^2}{\frac{4\pi R^3}{3}} = \frac{3}{R} \qquad (2.30)$$

$$b = \frac{\pi R^2}{4\pi R^2} = \frac{1}{4} \tag{2.31}$$

R is the collector radius.

Most investigators consider only direct interception and sedimentation to be of importance within filtration of molten metals. These efficiencies will be calculated assuming potential flow.

The collision efficiency due to direct interception is

$$\eta_{i,\,sphere} = \frac{\left(\frac{3}{2}U_\infty\right)2\pi R a}{U_\infty \pi R^2} = \frac{3a}{R} \tag{2.32}$$

According to Rasch (1987) the collision efficiency due to sedimentation is

$$\eta_{g,\,sphere} = \frac{A_v \cdot U_s}{A \cdot U_\infty + A_v \cdot U_s} = \frac{U_s}{U_\infty + U_s} \tag{2.33}$$

where U_s is Stokes settling velocity and U_∞ is the particle approach velocity. A_v is the vertical projection of the collector and A is the projection normal to the mean particle flow direction.

In Chapter 3 a two dimensional water model consisting of circular rods will be presented. The above properties for a circular rod of length L and radius R are therefore calculated still assuming potential flow.

$$\frac{A_s}{V_s} = \frac{2\pi RL}{\pi R^2 L} = \frac{2}{R} \tag{2.34}$$

$$b = \frac{2RL}{2\pi RL} = \frac{1}{\pi} \tag{2.35}$$

The collision efficiency due to direct interception is

$$\eta_{i,rod} = \frac{(2U_\infty)2aL}{U_\infty 2RL} = \frac{2a}{R} \tag{2.36}$$

where U_∞ is the approach velocity. The collision efficiency due to sedimentation is

$$\eta_{g,rod} = \frac{A_v \cdot U_s}{A \cdot U_\infty + A_v \cdot U_s} = \frac{U_s}{U_\infty + U_s} \tag{2.37}$$

2.2.4 The influence of boundary layers

Above we assumed potential flow which is valid only at Reynolds numbers less than 1. Realistic conditions give Reynolds numbers far above 1. In these cases a core flow will develop and a boundary layer will take care of the no-slip condition by reducing the velocity from the velocity, U, in the potential flow in the core to zero at the wall. This boundary layer will affect particle deposition. Schlichting (1968) gives the velocity profiles in the boundary layer around both a sphere and a circular cylinder. From this information we calculate the reduction in deposition due to the boundary layer.

Circular cylinder

The ideal velocity distribution in potential irrotational flow past a circular cylinder of radius R and free-stream velocity U_∞ is given by

$$U(\theta) = 2U_\infty \sin\theta \tag{2.38}$$

θ is zero at the stagnation point. The distance from the surface of the cylinder is

$$y = \beta_c R \sqrt{\frac{\nu}{2U_\infty R}} \tag{2.39}$$

in terms of the dimensionless distance, β_c, from the cylinder surface. ν is the kinematic viscosity. Differentiation gives

$$dy = d\beta_c R \sqrt{\frac{\nu}{2U_\infty R}} \tag{2.40}$$

Introducing the velocity $u(\theta)$ in the boundary layer and the stream function ψ ($u = \frac{\partial\psi}{\partial y}$) we get:

$$\frac{u}{U} = \frac{1}{U} \cdot \frac{\partial\psi}{\partial\beta_c} \cdot \sqrt{\frac{2U_\infty}{\nu R}} \tag{2.41}$$

Rewriting (2.41) and inserting (2.38):

$$\frac{\partial\psi}{\partial\beta_c} = \sqrt{2\nu R U_\infty} \cdot \frac{u}{U} \cdot \sin\theta \tag{2.42}$$

Integrating over β_c:

$$\psi = \sqrt{2\nu RU_\infty}\sin\theta \int_0^{\beta_c} \frac{u}{U} d\beta_c = \sqrt{2\nu RU_\infty}\cdot I(\beta_c, \theta) \qquad (2.43)$$

u/U as a function of β_c is tabulated by Schlichting (1968, p. 154). $I(\beta_c, \theta)$ has been calculated as a function of θ for some β_c values shown in Figure 2.1.

$I(\beta_c, \theta)$ is a measure of the volume flow at distance β_c at different angles θ. We see that a maximum angle (θ_{max}) exists. θ_{max} increases with increasing β_c. The physical implications of this is that inclusions of different sizes have maxima in removal by pure interception at different angles. All calculated θ_{max} are less than 90°.

Then the collision efficiency due to interception is

$$\eta_i = \frac{2L\psi(y=a)}{2RLU_\infty} \qquad (2.44)$$

where the boundary layer has been taken into account through the stream function. Potential flow gives

$$\eta_{i,pot} = \frac{2La(2U_\infty)}{2RLU_\infty} = \frac{2a}{R} \qquad (2.45)$$

where a is the inclusion radius and L the length of the cylinder.

Inserting (2.43) in (2.44) and dividing by (2.45):

$$\frac{\eta_i}{\eta_{i,\,pot}} = \frac{I(\beta_c(\alpha), \theta_{max})}{\beta_c(\alpha)} \tag{2.46}$$

$\eta_i/\eta_{i,\,pot}$ is plotted in Figure 2.2 as a function of β_c.

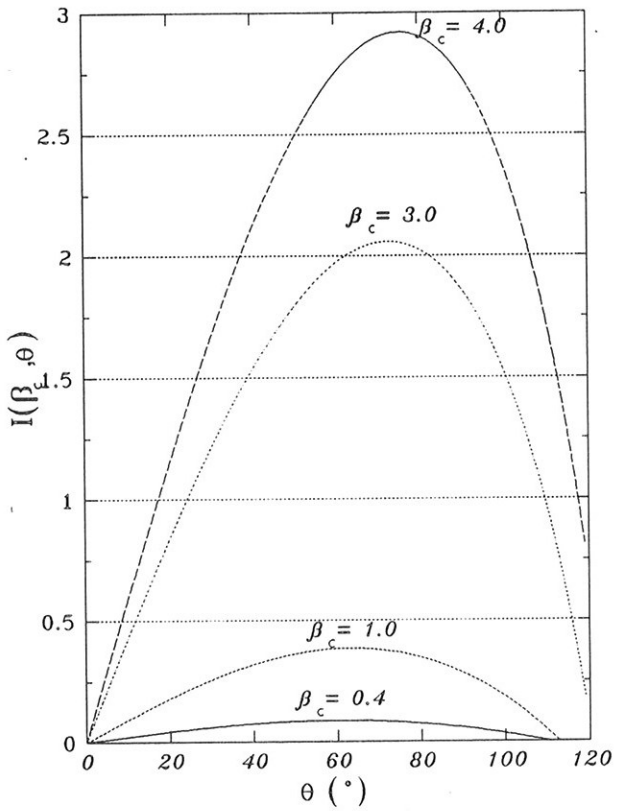

Figure 2.1 $I(\beta_c, \theta)$ as a function of θ for some β_c $(=\frac{\gamma}{R}\sqrt{\frac{2U_\infty R}{\nu}})$ values.

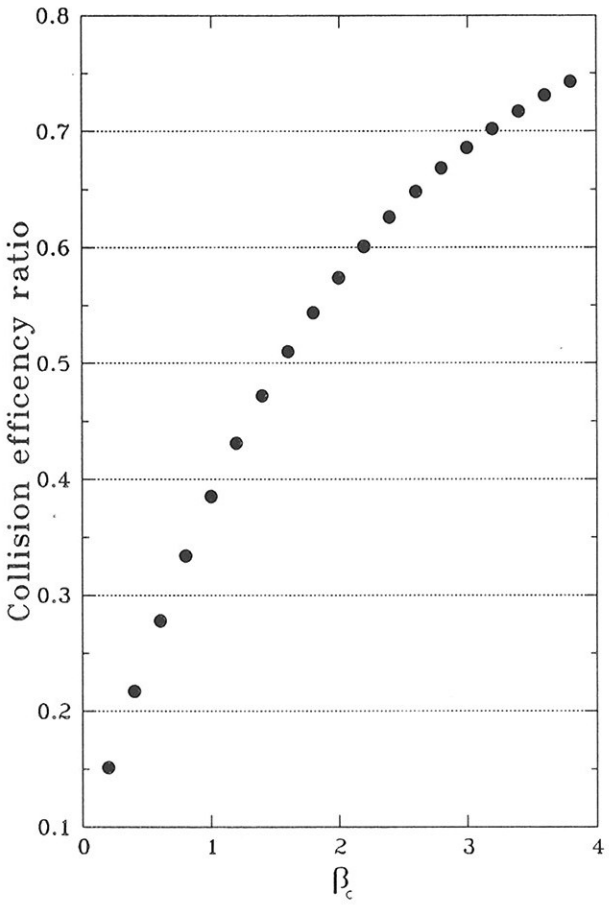

Figure 2.2 $\eta_i/\eta_{i,pot}$ as a function of β_c ($=\frac{\nu}{R}\sqrt{\frac{2U_\infty R}{\nu}}$).

Sphere

For a sphere of radius R, kept at rest in a free stream velocity U_∞, the ideal potential velocity distribution is given by

$$U(\theta) = \frac{3}{2} U_\infty \sin\theta \tag{2.47}$$

θ is zero at the stagnation point. The distance from the surface of the sphere is

$$y = \beta_s R \sqrt{\frac{\nu}{3U_\infty R}} \tag{2.48}$$

where β_s is the dimensionless distance from the sphere surface. In analogy with the above we find that

$$\psi = \sqrt{3\nu R U_\infty} \sin\theta \int_0^{\beta_s} \frac{u}{U} d\beta_s = \sqrt{3\nu R U_\infty} \cdot I(\beta_s, \theta) \tag{2.49}$$

The integral I is solved by using u/U as a function of β_s as tabulated by Schlichting (1968, p. 227). $I(\beta_s, \theta)$ as a function of θ for some β_s values is shown in Figure 2.3.

Calculations similar to these for a sphere were made by Rasch (1987, p. 35). However, it seems that he has assumed that $\theta_{max} = 90°$ for all β_s. Thus his results differ somewhat from the calculations given here.

Taking into account that the maximum flow for most inclusion sizes are at angles less than 90°, the collision efficiency due to interception is

$$\eta_i = \frac{2\pi R \sin(\theta_{max})\psi(y=a,\theta_{max})}{\pi R^2 U_\infty} \tag{2.50}$$

where the boundary layer has been taken into account through the stream function. Potential flow gives

$$\eta_{i,pot} = \frac{2\pi R a\left(\frac{3}{2}U_\infty\right)}{\pi R^2 U_\infty} = \frac{3a}{R} \tag{2.51}$$

Inserting (2.49) in (2.50) and dividing by (2.51):

$$\frac{\eta_i}{\eta_{i,pot}} = \frac{\sin(\theta_{max})I(\beta_s(a),\theta_{max})}{\beta_s(a)} \tag{2.52}$$

$\eta_i/\eta_{i,pot}$ is plotted in Figure 2.4 as a function of β_s.

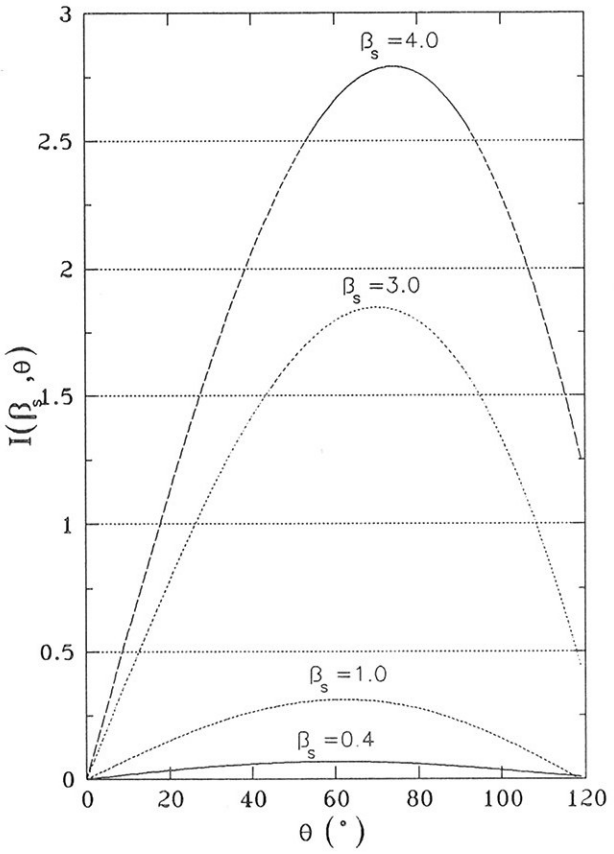

Figure 2.3 $I(\beta_s, \theta)$ as a function of θ for some β_s $(=\frac{y}{R}\sqrt{\frac{3U_\infty R}{\nu}})$ values.

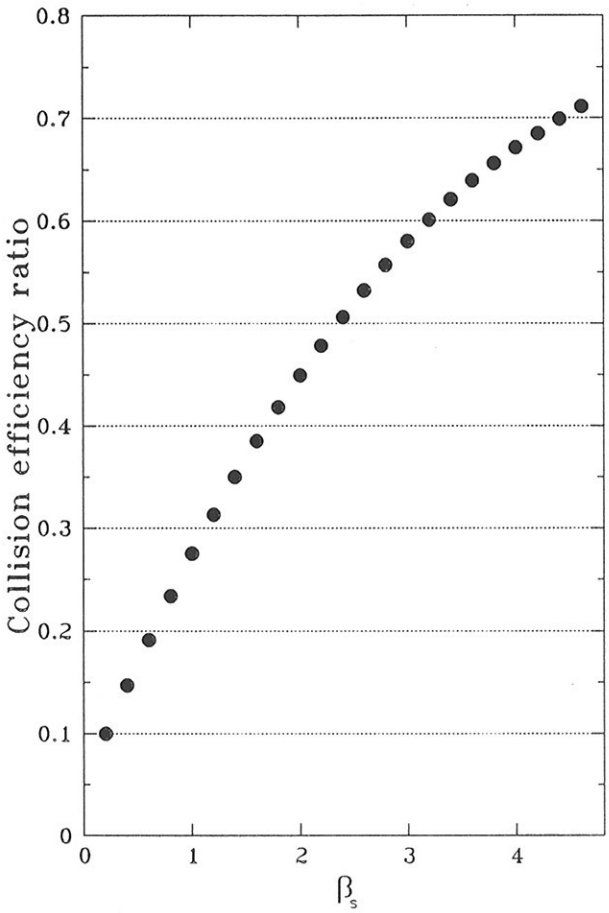

Figure 2.4 $\eta_i/\eta_{i,pot}$ as a function of β_s $(\frac{\gamma}{R}\sqrt{\frac{3U_\infty R}{\nu}})$.

2.3 Wettability and adhesion

The phenomena of wettability and adhesion describe the interaction between two fluid phases (gas/liquid/vacuum) and a solid. Solid-solid interaction must be treated separately (see Section 5.4). A large number of papers have been published on wettability of a molten metal on a crystal, mainly with production of composites in mind. In this case it is obvious that the objective is good wetting between the ceramic and the molten metal.

Within filtration the problem is more complex. Ideally inclusions should not wet the melt because the inclusions are removed from it. On the other hand the melt should perhaps wet the filter because inclusions are removed by forcing the melt through a filter. Filters frequently used by the aluminium industry are made of alumina (aluminium oxide). Alumina inclusions are also the major problem for the industry. This may seem to be a paradox.

In the following perfect wetting deignates that the liquid spreads completely over the solid. By partial wetting we mean that the wetting angle is less than 180°.

In the ideal filter inclusions should get stuck completely to the filter surface on first contact. With perfect wetting between both melt and filter and melt and inclusions, the inclusion-filter (solid-solid) interaction would have to be very strong (Figure 2.5).

The most realistic situation though is illustrated on Figure 2.6. Here we have partial wetting between both melt and filter, and melt and inclusion. Here a second fluid phase (gas or salt) wets filter and inclusions better than the melt does. With no second

fluid phase we might get the situation in Figure 2.7 where a vacuum or gaseous phase is generated on contact between filter and inclusion.

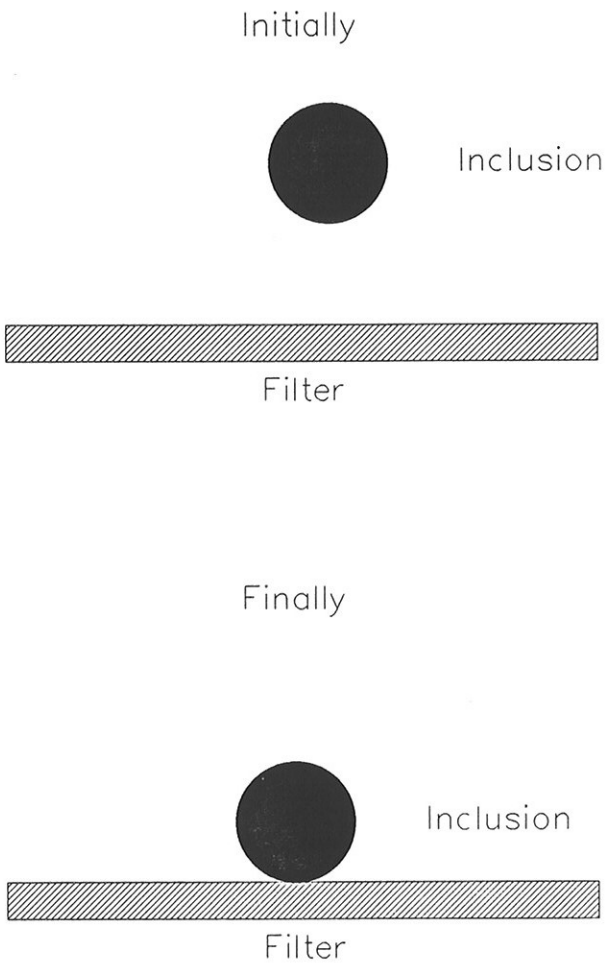

Figure 2.5 Perfect wetting between melt and filter, and melt and inclusion (no 2. fluid phase)

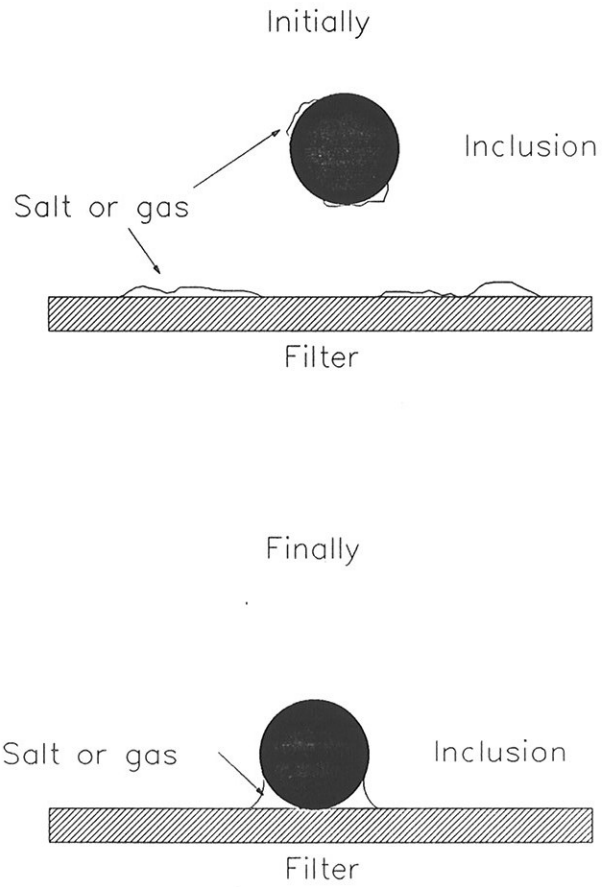

Figure 2.6 **Partial wetting between melt and filter, and melt and inclusion (with 2. fluid phase)**

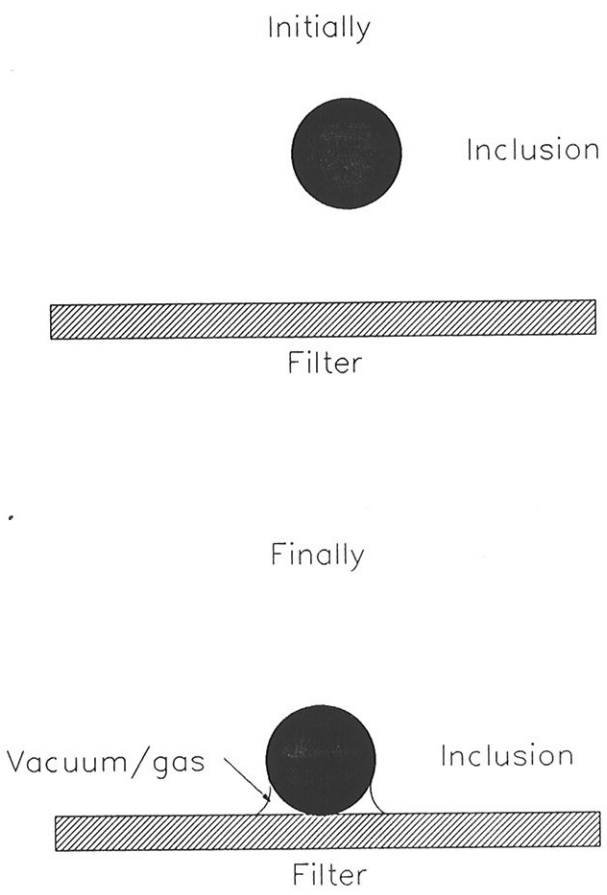

Figure 2.7 Partial wetting between melt and filter, and melt and inclusion (no 2. fluid phase)

Wetting is controlled by interfacial tensions (Figure 2.8). σ_{sl} is the interfacial tension between the solid and one of the fluid phases (usually the melt). σ_{sv} is the interfacial tension between the solid and the other fluid phase (usually vacuum). σ_{lv} is the interfacial tension between the two fluid phases (usually the surface tension of the melt). θ is the wetting angle (contact angle). A force balance along the solid surface gives Young's equation:

$$\cos\theta = \frac{\sigma_{sv} - \sigma_{sl}}{\sigma_{lv}} \tag{2.53}$$

The force component normal to the surface is only important for soft (deformable) solids.

The adhesion energy expresses the energy gained when two interfaces are replaced by a single interface. If a liquid/gas-interface and a gas/solid-interface are replaced by a liquid/solid-interface the adhesion energy is (Dupré's equation):

$$W = \sigma_{lv} + \sigma_{sv} - \sigma_{sl} \tag{2.54}$$

The adhesion energy should be large and positive to give good adhesion. It is well known that solved elements may change the interfacial tensions and thereby the adhesion energy (Naidich 1981, Delanney et al. 1987). We will consider the effects of adding elements next.

The theoretical equations presented above are valid for thermodynamic equilibrium or pseudo-equilibrium. According to Naidich (1968) wetting phenomena should be divided into

equilibrium systems and non-equilibrium systems. If the chemical potential of all components are equal in both phases ($\mu_i^s = \mu_i^l$) the system is in equilibrium. We will assume equilibrium and use thermodynamics to look into the change in interfacial tensions when alloying elements are added.

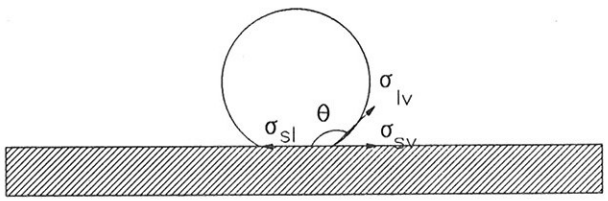

Figure 2.8 Interfacial tensions

2.3.1 Effects of solved elements on interfacial tensions

The surface tension of the pure metal is often known and we would like to determine the effect of various alloying additions and impurity levels. For systems with several components σ_{lv} is in general different from the Helmholtz free energy per surface area f^σ (Defay and Prigogine 1966).

$$\sigma_{lv} = \left(\frac{\partial F^\sigma}{\partial A}\right)_{n_i} = \left(\frac{\partial (A f^\sigma)}{\partial A}\right)_{n_i} = f^\sigma + A\left(\frac{\partial f^\sigma}{\partial A}\right)_{n_i} \qquad (2.55)$$

σ_{lv} is equal to f^σ only if $\left(\frac{\partial f^\sigma}{\partial A}\right)_{n_i} = 0$, i.e. only if f^σ does not change when the surface area is changed. This is the case only for a one-component system in general, i.e. for a pure melt

$$\sigma_{lv}^{p} = f^{\sigma} \tag{2.56}$$

If the concentration of the various components at the surface is given by:

$$\Gamma_i = \frac{n_i^{\sigma}}{A}$$

then

$$\left(\frac{\partial f^{\sigma}}{\partial A}\right)_{n_i} = \sum_{i=1}^{r}{}^{k} \frac{\partial f^{\sigma}}{\partial \Gamma_i}\left(\frac{\partial \Gamma_i}{\partial A}\right)_{n_i}$$

The convention that component 1 is the solvent metal is adopted.

$$\frac{\partial f^{\sigma}}{\partial \Gamma_i} = \mu_i^{\sigma}$$

is the chemical potential of component i at the interface. Furthermore

$$\left(\frac{\partial \Gamma_i}{\partial A}\right)_{n_i} = \left(\frac{\partial\left(\frac{n_i^{\sigma}}{A}\right)}{\partial A}\right)_{n_i} = -n_i^{\sigma}\frac{\partial A^{-1}}{\partial A} = -\frac{n_i^{\sigma}}{A^2} = -\frac{\Gamma_i}{A}$$

Then Eq. (2.55) becomes

$$\sigma_{lv} = f^{\sigma} - \sum_{i=1}^{k} \mu_i^{\sigma}\Gamma_i \tag{2.57}$$

σ_{lv} depends on the chemical potential at the surface μ_i^σ and on the surface coverage Γ_i. It will be seen that the ratio between the n_i^σ's at the surface in general is different from the molar ratio in the bulk. Elements that tend to accumulate at the surface are called surface active.

Differentiation of Eq. (2.57) gives

$$d\sigma_{lv} = df^\sigma - \sum_{i=1}^{k} \mu_i^\sigma d\Gamma_i - \sum_{i=1}^{k} \Gamma_i d\mu_i^\sigma \qquad (2.58)$$

f^σ depends on T, c_i', c_i'' *and* Γ_i. It has a total differential

$$df^\sigma = \left(\frac{\partial f^\sigma}{\partial T}\right)dT + \sum_{i=1}^{k}\left\{\left(\frac{\partial f^\sigma}{\partial \Gamma_i}\right)d\Gamma_i + \left(\frac{\partial f^\sigma}{\partial c_i'}\right)dc_i' + \left(\frac{\partial f^\sigma}{\partial c_i''}\right)dc_i''\right\}$$

$$= -s^\sigma dT + \sum_{i=1}^{k} \mu_i^\sigma d\Gamma_i + \sum_{i=1}^{k}\{\epsilon_i' dc_i' + \epsilon_i'' dc_i''\} \qquad (2.59a)$$

where $\left(\frac{\partial f^\sigma}{\partial T}\right) = -s^\sigma$ and ϵ_i' and ϵ_i'' are the so-called cross-chemical potentials because they represent the influence on the surface free energy of the concentration of i on either side of the surface. At equilibrium (Defay and Prigogine 1966)

$$df^\sigma = -s^\sigma dT + \sum_{i=1}^{k} \mu_i^\sigma d\Gamma_i \qquad (2.59b)$$

Summing Eqs. (2.58) and (2.59b):

$$d\sigma_{lv} = -s^{\sigma}dT - \sum_{i=1}^{k}\Gamma_i d\mu_i^{\sigma}$$

At constant temperature

$$d\sigma_{lv} = -\sum_{i=1}^{k}\Gamma_i d\mu_i^{\sigma} \qquad (2.60)$$

To obtain the surface tension σ_{lv} when there are several components in addition to the solvent metal, the surface area occupied by one mole of species i, A_i^{σ} is introduced. Then

$$\Gamma_i = \frac{n_i^{\sigma}}{\sum_{j=1}^{k} n_j^{\sigma} A_j^{\sigma}}$$

or in terms of mass percent at the surface

$$\Gamma_i = \frac{[\%i]^{\sigma}/m_i}{\sum_{j=1}^{k}[\%j]^{\sigma} A_j^{\sigma}/m_j}$$

The activity coefficient at the surface (Lupis 1983) f_i^{σ} is introduced

$$f_i^{\sigma} = \frac{a_i}{[\%i]^{\sigma}}$$

where the activity a_i is given in mass percent. When $[\%i]^{\sigma}$ -> 100, then f_i^{σ} -> 1.

Since the mass percentages on the surface sum up to 100%:

$$\sum_{i=1}^{k} [\%i]^{\sigma} = 100 \tag{2.61}$$

or in terms of activities and surface activity coefficients

$$\sum_{i=1}^{k} \frac{a_i}{f_i^{\sigma}} = 100 \tag{2.62}$$

Similarly for the bulk phase

$$\sum_{i=1}^{k} \frac{a_i}{f_i} = 100$$

According to the Gibbs-Duhem equation ($\sum x_i d\mu_i = 0$)

$$\sum_{i=1}^{k} x_i \frac{da_i}{a_i} = 0$$

Now for the mole fraction

$$x_i = \frac{[\%i]/m_i}{\sum_{j=1}^{k} [\%j]/m_j} \tag{2.63}$$

This inserted in the Gibbs-Duhem equation gives

$$\sum_{i=1}^{k} \frac{[\%i]da_i}{m_i a_i} = 0$$

or

$$\sum_{i=1}^{k} \frac{da_i}{m_i f_i} = 0 \qquad (2.64)$$

To obtain an equation for the surface tension, expressions for Γ_i and $d\mu_i^\sigma$ are introduced in Eq. (2.60). Furthermore, concentrations are replaced by activities. At equilibrium the chemical potentials for component i are equal in all phases, giving:

$$\mu_i^\sigma = \mu_i' = \mu_i''$$

In accordance with Lupis (1983, p.401) it is assumed that the monolayer behaves ideally, i.e.

$$\mu_i^\sigma = \mu_i^{\sigma,0}(T,p) + RT\ln(a_i^\sigma) - \sigma_{lv} A_i^\sigma$$

and

$$\mu'_i = \mu'^{,0}_i(T,p) + RT\ln(a_i)$$

giving

$$d\mu_i^\sigma = RT\, d(\ln a_i)$$

$$\frac{d\sigma_{lv}}{RT} = \frac{-\sum_{i=1}^{k} \frac{a_i}{m_i f_i^\sigma} d(\ln a_i)}{\sum_{i=1}^{k} \frac{a_i A_i^\sigma}{m_i f_i^\sigma}}$$

or

$$\frac{d\sigma_{lv}}{RT} = \frac{-\sum_{i=1}^{k} \frac{da_i}{m_i f_i^\sigma}}{\sum_{i=1}^{k} \frac{a_i A_i^\sigma}{m_i f_i^\sigma}} \tag{2.65}$$

We notice that if $f_i^\sigma = f_i$ then according to the Gibbs-Duhem equation $d\sigma_{lv} = 0$. This means that if the activity coefficients were the same in the bulk as on the surface, surface tension would not change with position. In general $f_i^\sigma \neq f_i$. In this case Eq. (2.65) may be written

$$\sum_{i=1}^{k} \frac{a_i A_i^\sigma}{m_i f_i^\sigma} + \sum_{i=1}^{k} \frac{da_i}{d\sigma_{lv}} \frac{RT}{m_i f_i^\sigma} = 0 \tag{2.66}$$

We wish to study the effect of the solute additions. Therefore, the solvent component, i = 1, is eliminated from Eq. (2.66). To accomplish this Eq. (2.64) is multiplied by $\frac{f_1 RT}{f_1^\sigma} \frac{1}{d\sigma_{lv}}$ to give

$$\sum_{i=1}^{k} \frac{da_i}{d\sigma_{lv}} \frac{RT f_1}{f_1^\sigma m_i f_i} = 0$$

Furthermore, Eq. (2.62) is multiplied by A_1^σ / m_1 to give

$$\sum_{i=1}^{k} \frac{A_1^\sigma a_i}{m_1 f_i^\sigma} = 100 \frac{A_1^\sigma}{m_1}$$

If these two equations are subtracted from Eq. (2.66), one obtains:

$$\frac{100A_1^\sigma}{m_1} + \sum_{i=2}^{k}\left\{\left(A_i^\sigma - \frac{A_1^\sigma m_i}{m_1}\right)a_i + RT\left(1 - \frac{f_1 f_i^\sigma}{f_1^\sigma f_i}\right)\frac{da_i}{d\sigma_{lv}}\right\}\frac{1}{m_i f_i^\sigma} = 0 \quad (2.67)$$

For a dilute binary system f_1 and f_2 are constants with respect to a_2.

f_2^σ and f_1^σ depend on a_2. This relationship must be determined before Eq. (2.67) can be integrated. A Langmuir model where the adsorption is limited to a monolayer on the surface gives the "exchange equation":

$$(component\ 2\ in\ bulk) + (component\ 1\ on\ surface) = (component\ 2\ on\ surface) + (component\ 1\ in\ bulk) \quad (2.68a)$$

This layer is regarded as an ideal two-dimensional solution of equal size solvent and solute molecules. Alternatively surface areas could be taken into account by writing the exchange equation as:

$$\frac{(component\ 2\ in\ bulk)}{A_2^\sigma} + \frac{(component\ 1\ on\ surface)}{A_1^\sigma} = \frac{(component\ 2\ on\ surface)}{A_2^\sigma} + \frac{(component\ 1\ in\ bulk)}{A_1^\sigma} \quad (2.68b)$$

The equilibrium constant for the first exchange equation is expressed by, ΔG°, the energy gained by moving one mole of component 2 from the bulk to the surface - the "free energy of adsorption".

$$\frac{a_2 \cdot [\%1]^{\sigma}}{[\%2]^{\sigma} \cdot a_1} = e^{\frac{\Delta G^{\circ}}{RT}} \qquad (2.69a)$$

where a_1 and a_2 are the solvent and solute activities in solution and, by virtue of the model, the activities in the adsorbed layer are given by the respective weight percents (Adamson 1982, p. 371). The second exchange equation avoids the assumption that activities in the adsorbed phase can be represented by weight percents (Adamson 1982, p. 386):

$$\left(\frac{a_2}{a_2^{\sigma}}\right)^{\kappa} \frac{a_1^{\sigma}}{a_1} = e^{\frac{\Delta G^{\circ}}{RT}} \qquad (2.69b)$$

where $\kappa = A_1^{\sigma}/A_2^{\sigma}$.

In the following Eq. (2.69a) will be used, but the inconsistency introduced by neglecting κ will partly be compensated by empirical determination of ΔG°.

To eliminate component 1 from the exchange Equation (2.69a) use that, in general,

$$\sum_{j=1}^{k} [\%j] = 100$$

$$\sum_{j=1}^{k} [\%j]^{\sigma} = 100$$

Combined with the definition of the surface activity coefficients inserted in Eq. (2.69a) and writing weight percent instead of activities in the bulk phase also give:

$$f_2^\sigma = \frac{a_2}{100}\left(1 - \frac{f_1}{f_2}e^{\frac{\Delta G^\circ}{RT}}\right) + f_1 e^{\frac{\Delta G^\circ}{RT}} \qquad (2.70a)$$

If Eq. (2.69a) is written in activities only, we find that

$$\frac{f_2^\sigma}{f_1^\sigma} = e^{\frac{\Delta G^\circ}{RT}} \qquad (2.70b)$$

Eq. (2.67) for a two-component system (k=2) can then be integrated to give

$$\sigma_{lv} = \sigma_{lv}^p - \frac{m_1}{A_1^\sigma m_2}\cdot\frac{RT}{b_2}\cdot\left(1-\frac{f_1}{f_2}e^{\frac{\Delta G^\circ}{RT}}\right)\cdot\ln\left(b_2\frac{f_2}{f_1}e^{\frac{-\Delta G^\circ}{RT}}\frac{[\%2]}{100}+1\right) \qquad (2.71a)$$

where

$$b_2 = \frac{A_2^\sigma m_1}{A_1^\sigma m_2} - \frac{f_1}{f_2}e^{\frac{\Delta G^\circ}{RT}} \qquad (2.71b)$$

σ_{lv} is given in terms of a_2 and the surface tension of the pure solvent σ_{lv}^p. This may be regarded as a further development of an equation given by Belton (1976).

This far we have considered a melt surface in contact with vacuum. In principle the argumentation above could have been carried out for a melt surface in contact with a solid. Therefore

$$\sigma_{sl} = \sigma_{sl}^p - \frac{m_1}{A_1^\sigma m_2}\cdot\frac{RT}{b_2}\cdot\left(1-\frac{f_1}{f_2}e^{\frac{\Delta G^\circ}{RT}}\right)\cdot\ln\left(b_2\frac{f_2}{f_1}e^{\frac{-\Delta G^\circ}{RT}}\frac{[\%2]}{100}+1\right) \qquad (2.72)$$

were σ_{sl}^{p} is the interfacial tension between the pure melt and the solid and σ_{sl} is the interfacial tension when the melt contains [%2] weight percent component 2. b_2 is defined in analogy with Eq. (2.71b). The free energy of adsorption, ΔG°, and the activity coefficients must of course be determined for each solid-melt system.

Summary of assumptions that led to Eqs. (2.71) and (2.72)

1. The system is in chemical equilibrium.

2. Constant temperature.

3. The activity coefficient at the surface is defined in terms of the activity in the bulk:

$$f_i^{\circ} = \frac{a_i}{[\%i]^{\circ}}$$

4. The surface is described as a monolayer and this monolayer is assumed to behave ideally.

5. Dilute solution is assumed.

6. A Langmuir model for adsorption is used, i.e. the monolayer is regarded as an ideal two-dimensional solution of equal size solvent and solute molecules.

7. It is assumed that the activities in the adsorbed layer are given by the respective weight percents. This is consistent with assumption 6.

2.4 Interaction between flow and surface forces

This far fluid flow and wettability and adhesion have been considered independently. The dynamics of the interaction between the flow and the surface forces holding the particle at the surface are very complex. In this section only the simple static situation shown in Figure 2.9 will be considered. Wieser (1984) considered this problem in the case of filtration of steel. His approach was to consider the energy gained by the particle sitting on the surface instead of being suspended in the melt. This approach has also been applied by researchers on penetration of particles into a melt (Engh et al. 1972, Farias and Robertson 1982, Ozawa and Mori 1983).

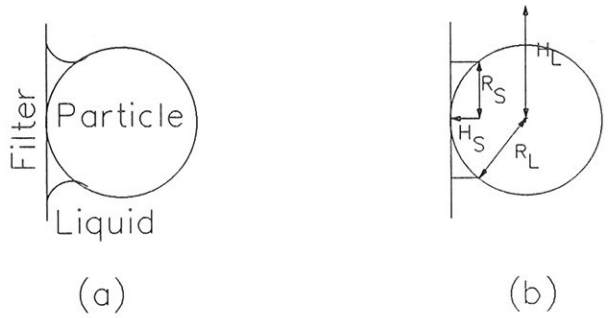

Figure 2.9 Schematic view of liquid metal withdrawal from the filter and contacting particle (a), and of geometry used for energy balance calculations (b).

The energy gain, ΔE_{tot}, which result from liquid metal withdrawal can be calculated with the following energy balance:

$$\Delta E_{tot} = \Delta E_{lf} + \Delta E_{lp} - \Delta E_{lv} - p\Delta V \qquad (2.73)$$

where

ΔE_{lf} = the energy difference on the disk shaped area of the filter where liquid metal withdraws

ΔE_{lp} = the energy difference on the corresponding spherical particle segment

ΔE_{lv} = the energy required for the formation of the cylindrical liquid metal surface

$p\Delta V$ = the PV work against the surrounding pressure, after neglecting the pressure of vaporising metal and alloy species

These expressions are further defined below in terms of the geometrical parameters given in Figure 2.10, and the interfacial and surface tensions σ_{sl}, σ_{pl}, σ_{sv}, and σ_{pv} for the metal-filter, the metal-particle, the filter, and the particle respectively:

$$\Delta E_{lf} = \pi R_s^2(\sigma_{sl} - \sigma_{sv}) \qquad (2.74)$$

where

$$(\sigma_{sl} - \sigma_{sv}) = -\sigma_{lv} \cos\beta$$

β = wetting angle on the filter.

$$\Delta E_{lp} = 2\pi R_L H_S(\sigma_{pl} - \sigma_{pv}) \qquad (2.75)$$

where

$$(\sigma_{pl} - \sigma_{pv}) = -\sigma_{lv} \cos\alpha$$

α = wetting angle on the particle.

$$\Delta E_{lv} = 2\pi R_S(D + H_S)\sigma_{lv} \tag{2.76}$$

where

$$R_S = \sqrt{H_S(2R_L - H_S)}$$

$$p\Delta V = (p_{atm} + \rho g H)\left(\pi H_S^2\left(R_L - \frac{2}{3}H_S\right) + \pi R_S^2 D\right) \tag{2.77}$$

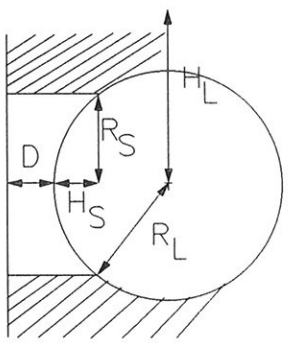

Figure 2.10 Schematic view of a particle approaching a filter wall following collapse of liquid metal film.

When the energy gain is positive the particle may be drawn towards the filter surface. If this will happen depends on the wetting conditions. It can be seen from the above equations that a positive energy gain is achieved if both or at least one of the particle or filter is non-wetting with respect to the melt. If ΔE_{tot} is differentiated with respect to the distance D from the wall we get the force pressing the particle towards the filter:

$$F = \frac{d\Delta E_{tot}}{dD} = -\pi R_S^2(p_{atm} + \rho g H) - 2\pi R_S \sigma_{lv} \qquad (2.78)$$

It is seen that the force depends on the surface tension of the melt, the metallostatic head, and the size of the particle. The flow field exerts a drag force on the particle along the filter surface. O'Neill (1968) calculated the drag force on a sphere in contact with a plane wall in a slow linear shear flow:

$$F_D = 1.7009 \cdot 6\pi\mu v R_L \qquad (2.79)$$

Whether a particle will stick to the wall or be re-entrained is a question of the relative magnitude of the above forces and the roughness of the filter surface.

Experimentally wetting conditions have been shown to affect the fluid flow through a packed bed (Luk et al. 1987). When a flowing liquid wets the solid surface with which it is in contact, the liquid molecules adhere to the solid surface, resulting in zero velocity at the interface. The classical fluid-mechanical relationships, such as Poiseuille's and Ergun's equations, are based on theoretical and experimental studies in which the no-slip boundary condition has been invoked. Consider the case when the liquid phase does not wet the solid surface with which it is in

contact. Use of the no-slip boundary conditions in this situation leads to differences between experimentally observed and theoretically predicted values.

Luk et al.'s experimental data show that the no-slip condition at the wall is invalid at low flow rates (Re = 42) in tube flow. Farther away from the wall, the velocity profiles follows a near parabolic shape. The flow rates in the non-wetting cases were 5-15% higher than the wetting cases. Since the available pressure drop for the flow was constant, these observations can be caused only by slip at the wall. The results show that the magnitude of wall slip decreased significantly at higher Reynolds numbers (Re > 140) and that there was virtually no difference in the velocity profiles for the wetting and non-wetting cases. For both the transient and turbulent regimes, or even at the upper end of the laminar regime, no experimental evidence of wall slip was found.

For packed bed flow, it was found that at a constant flow rate the required pressure head decreases as the surface become more and more non-wetting. It has been shown that Ergun's equation is not valid when the liquid phase does not wet the packing at low Reynolds numbers. The friction factor is reduced by as much as 33% below that of a wetting packing surface.

3 WATER MODEL

In this chapter a two-dimensional filter model showing flow and particle deposition processes inside a filter is presented. The results are used to determine the relative importance of different deposition mechanisms. It will also give a qualitative view of the flow. Possibly the flow is laminar, in the transition zone between laminar and turbulent, or turbulent for realistic flow velocities.

3.1 Description of 2-D filter model

A two-dimensional plexiglas model has been built (Figure 3.1). It has a total length of 0.99 m with an inlet section of 0.12 m to distribute the water and a 0.54 m open channel to establish a uniform flow in front of the filter section. The cross-section available for flow is 0.2 m * 0.2 m. The length, height, and width of the filter section are all 0.2 m. The filter section consists of fifty (50) plexiglas rods placed in a matrix. The centres are 2 cm apart vertically and 4 cm apart horizontally. There are ten (10) horizontal rows of rods each with five (5) rods in depth facing the flow direction. Every second row is displaced 2 cm (see Figure 3.1). The rods are fixed to the walls by screws through their centres. The outlet and inlet sections are separated from the section with the filter by perforated plexiglas plates. The perforation consists of holes with diameter 3 mm. The outlet separation plate is positioned 4.5 cm behind the filter section.

Two types of collectors were used. One type was cylindrical rods with diameter 2 cm. The other was quadratic rods with sides 2 cm. The quadratic rods were placed with an edge facing the flow. This means that they somehow acted as cylindrical collectors with bulky protrusions. Both types of collectors were placed with their centres in the same positions. This leads to a porosity of 0.61 for the cylindrical collectors and 0.5 for the quadratic.

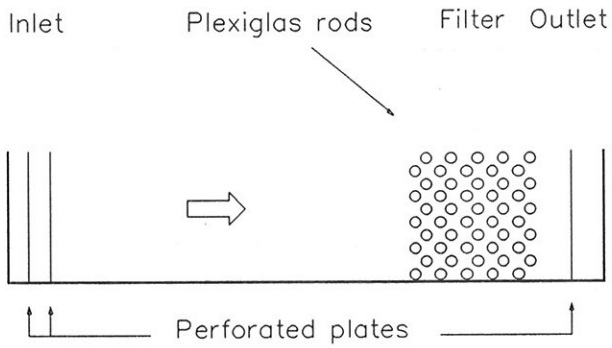

Figure 3.1 Water model (schematic side view)

Water was used to simulate aluminium melt. Polystyrene particles employed to simulate inclusions. To get a particle density as close as possible to the density of the liquid these particles had to be expanded by heating. This is described below.

Water was taken from the water tap and led from the outlet of the model into the drain. Flow volume was measured by a rotameter on the inlet side. Water temperature was approximately 9°C.

3.2 Preparation of particles

The "neutrally" buoyant particles were produced from polystyrene particles by heating them in water in a heating cabinet. Before heating their density was about 1040 kg/m^3 so they settled rapidly in water. After heating a large number of particles, 100 suitable particles were chosen by observing their settling behaviour in a water tank. These particles were used in all the experiments. A very fine masked filter at the outlet of the model ensured that the particles were retained. But even with these precautions some particles were lost and eventually the last experiments were run with only 75 particles. The particles had a diameter of approximately 1 mm. A rough measurement of the settling velocity gave a mean of 0.06 cm/s.

In order to get good adhesion between particles and collectors, the particles were suspended for half an hour in Magnafloc 292 (Allied Colloids Ltd., Low Moor, Bradford, Yorkshire BD12OJZ, England) before each experiment. Observations confirmed that this gave a very good adhesion.

Before introducing the particles into the model they were suspended in water and mixed completely. This suspension was then carefully poured into the model in a position just behind the inlet section dividing plate.

3.3 Particle removal - experimental results

Experiments with cylindrical and square collectors were performed. For both collectors several tests with (approach) velocities ranging from nearly zero to slightly above 1 cm/s were run. Every test was run twice. For each test the following data were recorded:

1. Type of collector.

2. Flow velocity.

3. Number of particles injected and number of particles "settling" out in front of the filter. The difference gives the number of particles entering the filter.

4. Number of particles deposited on each of the fifty rods. The sum for each row is given in Appendix B.

5. For all of the square collector experiments the position of the deposited particles on the collectors were noted. This was also done for some of the cylindrical collector experiments.

The filtration efficiency is defined as the number of particles deposited over the number of particles entering the filter. Using this definition the filtration efficiency has been calculated from the experiments in Table III.1.

It should be noted that the velocity given is the approach (superficial) velocity. Since the porosity for the cylindrical collectors is 0.61 and 0.50 for the square collectors, the interstitial velocities are different. The simplest possible way to estimate the interstitial velocity is to use Dupuit's law:

interstitial velocity = approach velocity divided by porosity

TABLE III.1 Filtration efficiency

U_∞ [cm/s]	Cylinder		Square	
0.03	0.698	0.586	0.900	0.869
0.06	0.581	0.643	0.695	0.820
0.10	0.557	0.514		
0.11			0.646	0.671
0.19	0.321	0.316	0.543	0.500
0.37	0.172	0.140	0.171	0.192
0.56	0.047	0.070	0.090	0.096
0.67	0.133	0.073	0.038	0.110
0.74	0.069	0.159	0.136	0.122
0.82	0.250	0.162	0.136	0.181
0.89	0.205	0.197	0.155	0.145
0.96	0.122	0.167	0.242	0.327
1.03	0.194	0.133	0.224	0.254
1.10	0.222	0.186		

This means that flow velocities inside the cylindrical collector filter is only 82% of the flow velocities inside the square collector filter for the same approach velocities.

In Figure 3.2 the depth distribution of particles is shown. To produce this figure the number of particles deposited on rows number 1,2,..,10 for all experiments have been added. Then these numbers have been summed up to give a total number of deposited particles (square: 537, cylinder: 483). The mean percentage deposited on each row has then been calculated. The distributions seem to be exponential functions of distance through filter.

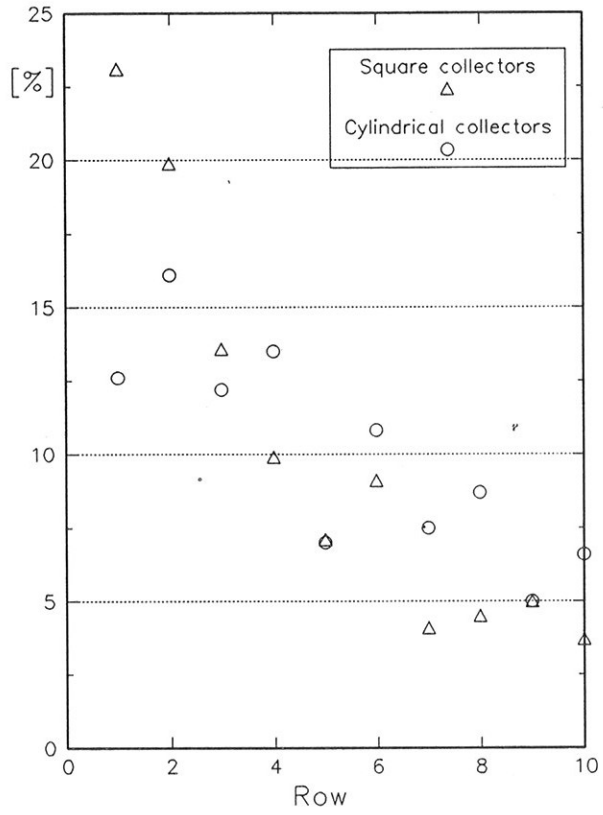

Figure 3.2 Depth distribution of particles. Percentage of particles on each row.

As mentioned above, the position of the deposited particles was registered for all experiments with square collectors (24) and for the last 10 (of 26) of the experiments with cylindrical collectors. The following information can be extracted:

1. The number of particles over and under the collectors.

2. The number of particles in front and behind the collectors.

3. For the square collectors it is also of interest to know whether the particles were sitting on an edge or not.

4. Two sides of the square collectors were rough and two were smooth i.e., every second face of the collector were smooth. The first row had a rough side upwards facing the flow and the second row a smooth side upwards. This pattern was continued throughout the filter. The number of particles on rough sides versus the number on smooth sides have been counted.

This information has been tabulated in Table III.2. All numbers are mean percentages over all experiments. The percentages for square and cylindrical collectors individually fulfil: (over) + (under) = 100%, (in front) + (behind) = 100%, (on edge) + (not on edge) = 100%, and (rough) + (smooth) = 100%. Particles on top are counted as behind.

TABLE III.2 Distribution of particles on collectors

Position	Cylinder [%]	Square [%]
over / under	84.7 / 15.3	90.4 / 9.6
in front / behind	41.6 / 58.4	34.6 / 65.4
on edge / not on edge	-	31.8 / 68.2
rough / smooth	-	50.6 / 49.4

The roughness of the collector surface has no measurable effect on deposition. A major part of the inclusions deposit on the top side of the collectors due to their being slightly heavier than the carrier fluid.

A larger number of particles deposit at the back of the collectors than at the front. An explanation for this is that there is a separation zone at the back of the collectors. In this separation zone the particle residence time over the collector increases and thereby enhances the probability of deposition due to settling.

3.4 Statistics

In Table III.1 the filtration efficiency was presented as the total number of particles deposited over the number of particles entering the filter. As can be seen in Appendix B this approach only utilizes a small number of the available information. It is a "black box" approach. In order to use all the information we need a model for the deposition processes inside the filter.

Several such models may be proposed. The information available consists of the number of particles deposited on every collector inside the filter. From Figure 3.1 we see that there are 10 rows each with 5 collectors along the flow direction. Every second row is vertically above each other. Summing the 5 rows that are directly above each other we get two rows each with 5 collectors. Because every velocity has been measured twice we then get four rows from which collision probabilities can be estimated. The number of particles approaching the two collector rows in each experiment is n. By assuming complete mixing the number of particles approaching one row is n/2.

Three models will be tested against the "black box" model. All of the models assume that the particles see 5 collectors in series and that the collectors are statistically independent - complete mixing is assumed. The models are:

1. The probability, p, of collision are the same for all collectors. The relationship between the filtration efficiency and the probability is

$$E = 1 - (1-p)^5$$

2. The probability of collision on the first row is p_1 and for the other rows p_2. This gives:

$$E = 1 - (1-p_1)(1-p_2)^4$$

3. Each row has its own probability of collision, p_i (i=1,..,5). The relationship then becomes:

$$E = 1 - (1-p_1)(1-p_2)(1-p_3)(1-p_4)(1-p_5)$$

The mean value, $\overline{p}$, the "adjusted" root mean square deviation, s_n, and adjusted standard error, S_n, are given by

$$\overline{p} = \frac{1}{n}\sum_{i=1}^{n} p_i$$

$$s_n = \frac{1}{\sqrt{n-1}}\sum_{i=1}^{n}\sqrt{(p_i-\overline{p})^2}$$

$$S_n = \frac{s_n}{\sqrt{n}}$$

According to the three models these values have been calculated for 1 parameter in model 1, 2 parameters in model 2, and 5 parameters in model 3. From these estimated values the mean filtration efficiency and its adjusted standard error have been calculated for every model.

In Tables III.3 and III.4 the mean values of the filtration efficiencies from Table III.1 and the mean filtration efficiencies calculated from the mean probabilities in the three models are given.

TABLE III.3 Mean filtration efficiency - cylinder

U_∞ [cm/s]	"Black box"	Model 1	Model 2	Model 3
0.03	0.642	0.887	0.717	0.642
0.06	0.612	0.867	0.647	0.612
0.10	0.536	0.875	0.549	0.535
0.19	0.319	0.311	0.317	0.318
0.37	0.156	0.157	0.159	0.156
0.56	0.059	0.060	0.059	0.058
0.67	0.103	0.105	0.106	0.103
0.74	0.114	0.116	0.116	0.114
0.82	0.206	0.215	0.208	0.206
0.89	0.201	0.201	0.202	0.201
0.96	0.145	0.147	0.147	0.144
1.03	0.164	0.166	0.166	0.164
1.10	0.204	0.213	0.213	0.204

TABLE III.4 Mean filtration efficiency - square

U_∞ [cm/s]	"Black box"	Model 1	Model 2	Model 3
0.03	0.885	0.869	0.891	0.884
0.06	0.758	0.956	0.857	0.757
0.11	0.659	0.760	0.779	0.658
0.19	0.522	0.584	0.618	0.522
0.37	0.182	0.185	0.183	0.182
0.56	0.093	0.094	0.093	0.093
0.67	0.074	0.075	0.075	0.073
0.74	0.129	0.128	0.129	0.129
0.82	0.159	0.154	0.156	0.158
0.89	0.150	0.144	0.149	0.150
0.96	0.285	0.283	0.298	0.285
1.03	0.239	0.221	0.232	0.239

Using the "black box" as the reference, it is seen that models 1 and 2 overestimates the filtration efficiencies for velocities below 0.20 cm/s. Model 3 on the other hand fits the reference perfectly, the discrepancy, if any, always in the third figure.

In Tables III.5 and III.6 we have used model 3 to represent the adjusted standard error in the filtration efficiency. Assuming that the measurements follow a Gaussian distribution this means that the true value is roughly twice as likely to fall within the interval $(\overline{E} - S_n, \overline{E} + S_n)$ as outside it. If only the black box model were to be used nothing could be said about how well the mean value estimates the true value.

TABLE III.5 Mean filtration efficiency and adjusted standard error (Model 3) - cylinder

U_∞ [cm/s]	Mean	Minimum	Maximum
0.03	0.642	0.518	0.741
0.06	0.612	0.455	0.733
0.10	0.535	0.413	0.638
0.19	0.318	0.234	0.396
0.37	0.156	0.096	0.214
0.56	0.058	0.011	0.104
0.67	0.103	0.035	0.167
0.74	0.114	0.062	0.164
0.82	0.206	0.141	0.267
0.89	0.201	0.147	0.254
0.96	0.144	0.075	0.209
1.03	0.164	0.100	0.225
1.10	0.204	0.109	0.291

TABLE III.6 Mean filtration efficiency and adjusted standard error (Model 3) - square

U_∞ [cm/s]	Mean	Minimum	Maximum
0.03	0.884	0.588	0.991
0.06	0.757	0.441	0.920
0.11	0.658	0.578	0.727
0.19	0.522	0.409	0.619
0.37	0.182	0.112	0.247
0.56	0.093	0.048	0.136
0.67	0.074	0.013	0.132
0.74	0.129	0.060	0.194
0.82	0.158	0.023	0.278
0.89	0.150	0.021	0.266
0.96	0.285	0.148	0.405
1.03	0.239	0.145	0.325

3.5 Flow patterns

For both square and cylindrical collectors it was found that the flow was laminar at the lower flow velocities and developed into a flow that could be described as turbulent. However there is no evidence that the flow is not just an unstable laminar transition flow regime.

The model with the cylindrical collectors mounted is shown on Figure 3.3. Figures 3.4 to 3.6 illustrate the flow with this configuration. The first figure (Fig. 3.4) shows laminar flow with streamlines clearly visible. Next a picture of the beginning mixing of the streamlines is shown (Fig. 3.5). Lastly the unstable flow regime, resembling turbulence, is shown (Fig. 3.6).

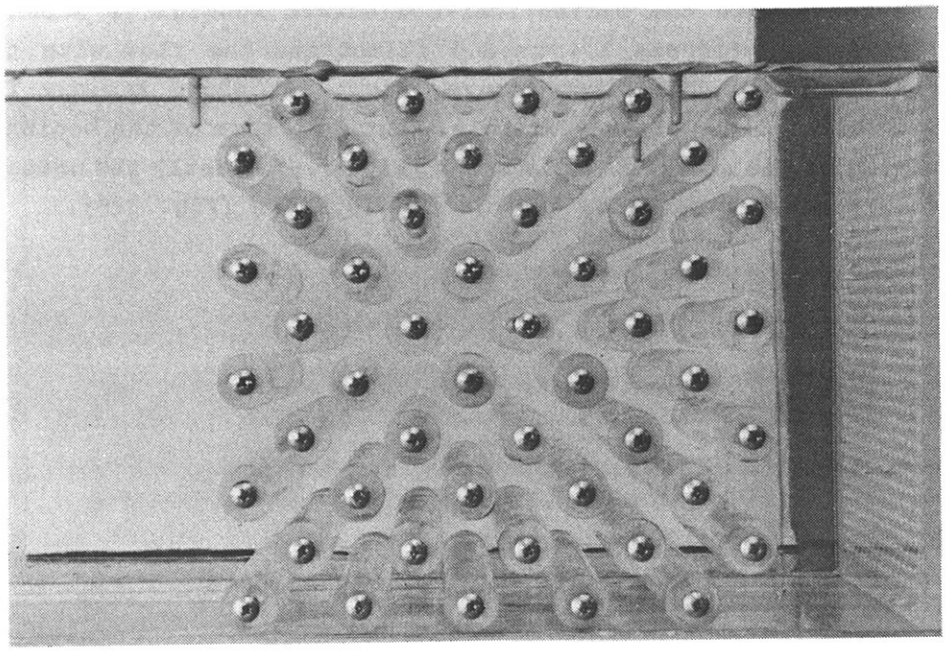

Figure 3.3 Water model with cylindrical collectors mounted.

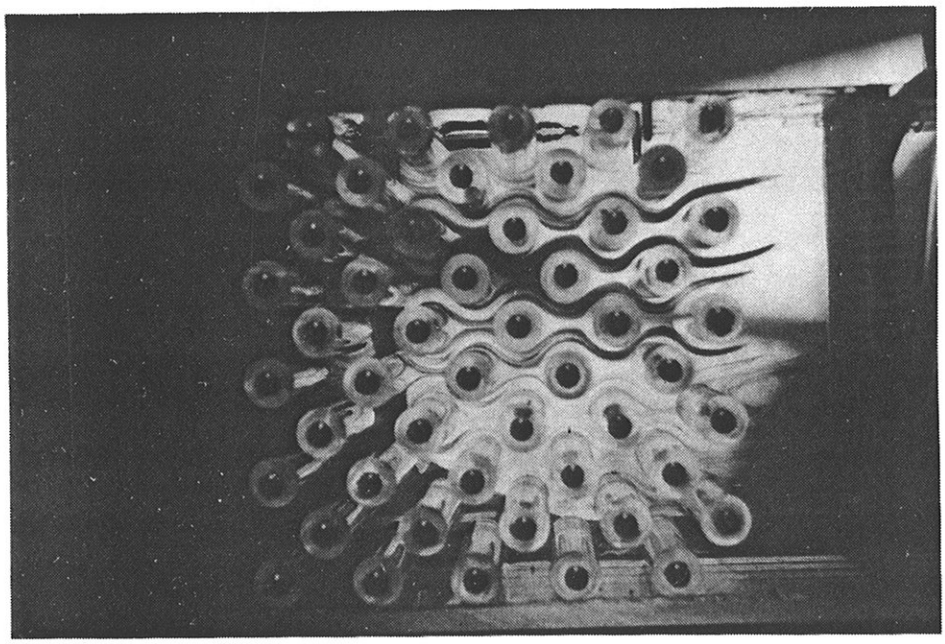

Figure 3.4 Laminar flow regime (U_∞ = 0.27 cm/s).

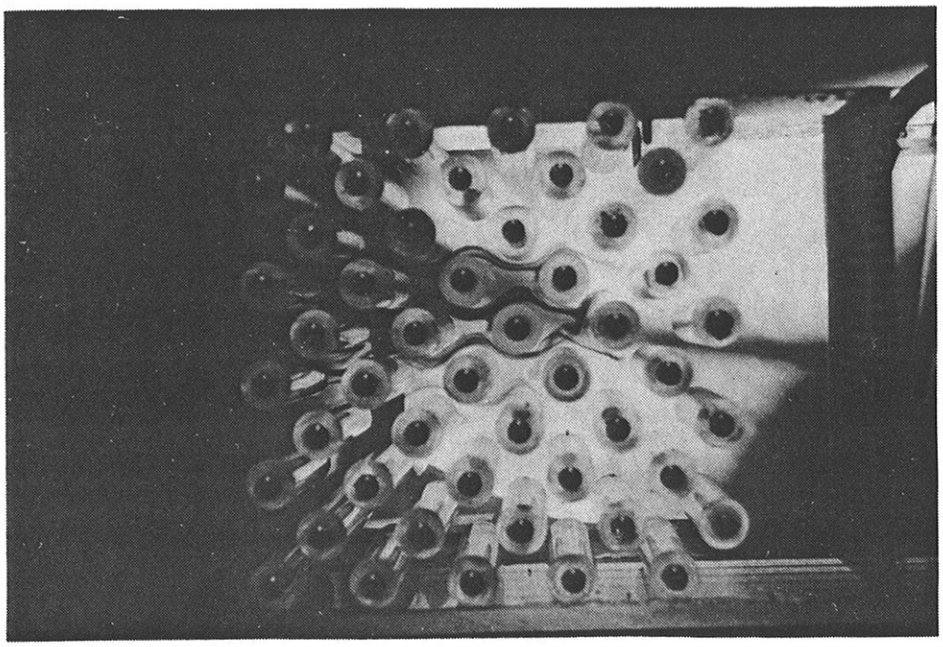

Figure 3.5 Mixing of streamlines begins (U_∞ = 0.55 cm/s).

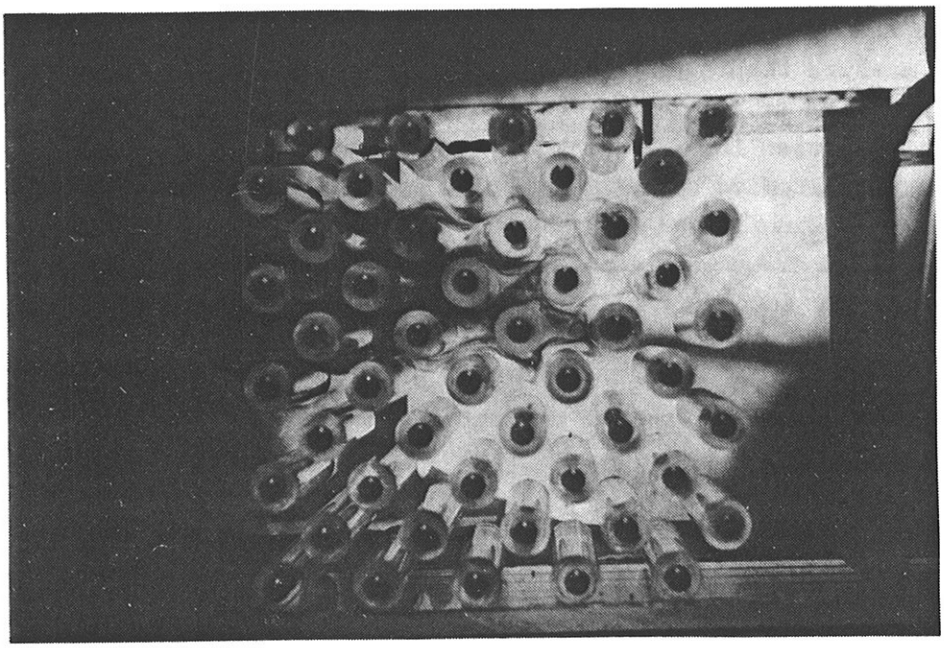

Figure 3.6 Unstable flow regime resembling turbulence (U_∞ = 0.82 cm/s).

4 INDUSTRIAL MEASUREMENTS

Metallographic methods are used to study filtration of inclusions from molten aluminium. This involves the use of sampling filters in order to examine the behaviour of industrial filters. The mechanisms of filtration must be understood for both sampling filters and industrial filters.

4.1 Measurement techniques

The next two subsections will describe the two techniques used to measure the level of inclusions in the melt. Both methods use filtration of the melt as a means to concentrate a large amount of impurities in a relatively small volume. The sampling filters are then studied by metallographic methods in order to determine impurity levels. We have used the Alcoa sampler combined with automatic image analysis (Bathen 1985a,b) and the PoDFA method (Simensen and Hartvedt 1985) to measure levels of aluminium carbide and aluminium oxide respectively.

Hydrogen was measured by the Telegas method.

4.2 Alcoa sampler method

Using a device called the Alcoa sampler (Figure 4.1) samples of 0.5 - 1.0 kg of melt is sucked through an immersed sampling filter by a vacuum pump. As can be seen from Figure 4.1 filtered melt is collected in a chamber and is weighed afterwards. The sampling filter and its socket are removed. Filter and filter socket are cut in half revealing a plane cut through the entire filter from inlet till outlet (Figure 4.2). This area is then prepared for metallographic analysis.

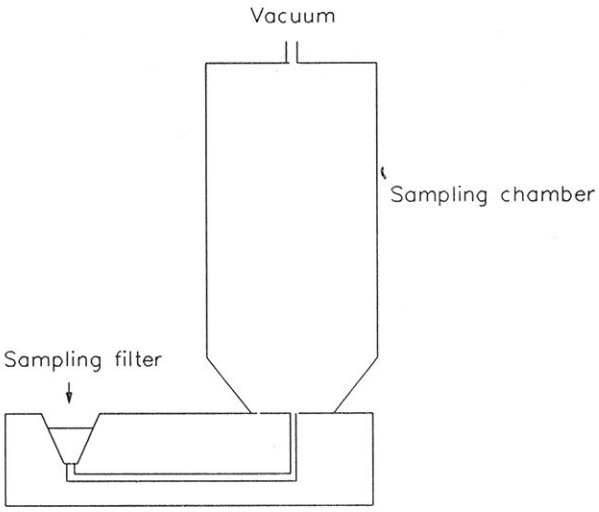

Figure 4.1. Alcoa sampler (principle)

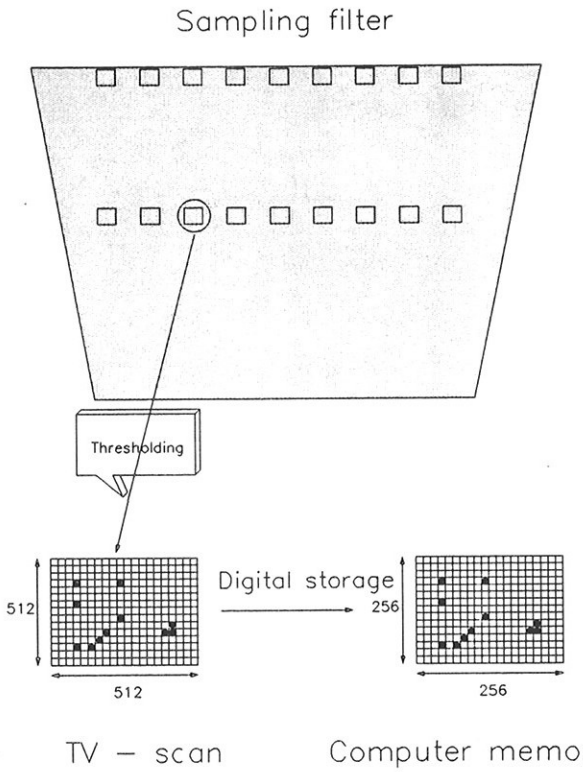

Figure 4.2. **Plane cut through sampling filter and sampling procedure from thresholding to computer storage**

4.2.1 Automatic image analysis

The equipment was a Leitz TAS (Texture Analysis System), an automatic image analyser incorporating a computer for controlling hardware, and for data treatment. A working monitor with lightpen allows user interaction such as modifying the image, etc.

Image acquisition of features for measurement was by way of television camera. The TV scan signal was thresholded according to intensity (grey value) or intensity gradient change surpassing a fixed level (edge detection). The thresholded images have two intensity levels only: for features to be investigated value 1 and for background 0, so called binary images. Digitized images can be stored in binary image memories allowing transformations of images and interactions between them.

One sampling field consists of 512 x 512 binary points, but the computer stores it as 256 x 256 points. This means that this resolution is halved, but the optical resolution limit is usually decisive.

The chosen preparation and microscope imaging method results in a presentation showing two kinds of inclusions in melts, particles appearing as dark features and features of light hue. The former may be borides, carbides, oxides and salt. The latter consist of solidification precipitates and some boride particles. Observations by SEM (Scanning Electron Microscope) have confirmed that dark particles largely contain Al, but a few only contain Ti.

Figure 4.2 illustrates the image analysis process from a sampling filter ready for analysis to the computer image stored on disk. Compared to the size of the cut the measuring field is small and we have to select a fraction only of the area for analysis. The entire area can of course be analysed, but this is a trade off between time of analysis and statistical accuracy. With

considerations like this in mind measuring fields have been arranged in parallel rows over a chosen range in the specimens. Typical filter depths are about 6 mm while the length of a measuring field in the depth direction is in the order of 0.1 mm.

Two nominal magnifications have been used: 410x and 200x. In most cases 200x have been used due to reduction in time of analysis and because it is better statistically with same number of measuring fields for both magnifications. The field size in this case is 179.00 μm * 161.57 μm which means that the distance between binary points is 0.35 μm in the primary image. In the stored image distance is twice this. Optical resolution limit may be assumed to be 0.70 - 0.75 μm and is thereby decisive.

4.2.2 Size distribution of inclusions

Successive transformations (described below) exclude particle groups below given sizes on an inscribed sizing basis. This image processing also results in particle groups splitting-up. Number of separate groups can be registered, and in addition number of convexities met with in image features in the sweep direction of the TV-camera.

The smallest particle size is a hexagon consisting of seven image points. Particle size number two have one image point layer extra, number three have two extra layers (relative to size one), etc.

Transformations consist of two main operations: first one or more erosions then the same number of dilatations. An erosion is removal of the outer layer of image points in each contour in the image. After this erosion image points are added such that every remaining image point is surrounded by six other image points. One such adding operation is a dilatation. For each particle size class the number of dilatations equals the number of erosions.

We register inclusion area, number of separate figures, and number of convexities met for each size class. Registrations are per square mm of melt. Of the number registrations the number of convexities is most reliable for all sizes. Number of separate figures tends to give too low numbers for smaller sizes.

4.2.3 Depth distribution of inclusions

As a step in the determination of inclusions in melts inclusion amounts and particle size distributions are investigated at varying depths in sampling filters.

We measure at certain depths within, or close to the filter on evenly spaced fields on a line traversing the open diameter of the filter. Field dimension, 0.1 - 0.2 mm in the depth direction, is relatively small compared to filter depth. About 15 fields are measured in one traverse.

The filters do not show clearly defined front edges, a jagged, incised outline starts the section, often bulging slightly outward. Depth is measured from a level of maximum particle content at the inlet, designating the position of this level as zero depth.

An inlet zone can be defined by the transition of solid filter to melt ratio from zero to a mean value. Inlet maximum level of inclusions is found in this zone which is about 0.25 mm deep. Solid filter to melt ratio where this maximum level is may vary considerably.

4.2.4 Calculation of the number size distribution in the melt

Measurements involve number of inclusions per square meter melt at a certain depth in the sampling filters. The concentration of inclusions, per unit volume melt, in and out of the industrial filter has to be determined from this information. It is assumed that all the inclusions in the melt are collected by the sampling filter.

Denoting the number size distribution per square meter melt, $N_A(r)$, and the number size distribution per unit volume melt, $N_V(r)$, they are related by

$$N_V(r) = \frac{N_A(r)}{2r}$$

where r is the inclusion radius.

All measurements are referred to the projected area of the filter in the flow direction, A. The fraction of melt, ϵ_j, is measured at depths j. n_j denotes $N_A(r)$ at depth j and h_j is the height of the cylinder where the measurements at depth j are assumed to be valid. Summation over the entire sampling filter and division by the weight, W, of melt sampled gives the number size distribution per unit melt in/out of the industrial filter, $N_V(r)$;

$$N_V(r) = \frac{A}{2r \cdot W} \sum_j n_j \cdot \epsilon_j \cdot h_j$$

The concentration of inclusions, c, is given by

$$c = \sum_r N_V(r)$$

4.3 PoDFA method

The PoDFA samples were analysed at Hydro Aluminium, Sunndal Verk. Simensen and Hartvedt (1985) have described the method in detail. We will only give a summary of main elements of the method:

Samples of the melt are remelted and poured into a pressure chamber. In the bottom of this chamber there is a porous disk - called PoDFA filter. Masking the filters gives them a constant open diameter of 11.8 mm. Overpressure in the chamber above the melt forces melt through the filter. By continuously measuring

the amount of melt filtered, the process is stopped when 300 g is left in the chamber - thereby avoiding contamination by the top oxide layer. From a normal sampling volume of 2 kg this gives approximately 1.7 kg through the filter. The sampling filter is then cut in half along the flow direction. A light microscope is used to measure amounts of oxide inclusions and films.

4.4 The campaigns

Measurements were taken in two campaigns at Elkem Aluminium, Lista Aluminiumverk. Samples of the melt were obtained before and after an industrial in-line Alcoa 528 bed filter. The first campaign was performed when the filter was practically unused, while the second campaign took place after three weeks of (industrial) running of the same filter.

When the first samples were taken, 66.6 tons of aluminium had passed through the filter. This series of measurements will be addressed as cast no. 1. After 152.3 tons cast no. 2 was sampled. Cast no. 3 was carried out after 2842.7 tons and cast no. 4 after 2980.3 tons.

Samples were taken four times per cast - one pair, in and out, at the start of the cast and one pair at the end of the cast. PoDFA samples were taken in pairs. Hydrogen levels were measured only twice per cast, in and out.

In casts 1 and 2 the product was "pure" aluminium, while during cast 3 and 4 the alloy contained 4.6 weight% magnesium.

The purge gas was argon - 100 l/min. During casts 3 and 4 the purge gas also contained 5 l/min of chlorine.

Figure 4.3 shows a schematic (side) view of the filter.

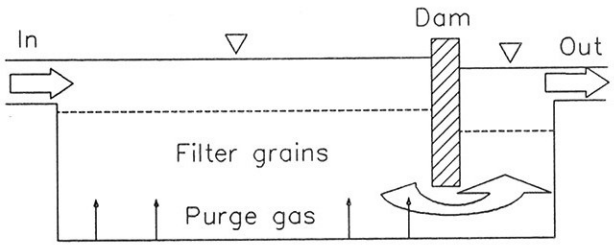

Figure 4.3. Alcoa bed filter (schematic side view)

4.5 Oxides and hydrogen

Tables IV.1 and IV.2 give the analysis results for total amounts of inclusions and films. Numbers n.1 or n.2 refer to sampling at start and end of cast number n, respectively. Filtration efficiency, E, is:

$$\frac{\text{amount in} - \text{amount out}}{\text{amount in}}$$

It seems that films move more easily through the filter than inclusions. An explanation could be that films are very flexible and collapsible and will follow streamlines closely. Furthermore, a film plugging a pore should be subject to drag forces that are large compared to adhesion forces.

Figures 4.4 - 4.6 show number size distributions of film lengths.

Table IV.3 shows the measured concentration of hydrogen. Efficiency of hydrogen removal has been calculated.

TABLE IV.1 Oxide films

Cast	In [ppm]	Out [ppm]	E [%]
3.1	1.185	0.675	43
3.2	0.65	0.675	-
4.2	0.775	0.755	-

TABLE IV.2 Oxide inclusions

Cast	In [ppm]	Out [ppm]	E [%]
3.1	0.81	0.155	81
3.2	0.485	0.35	28
4.2	0.55	0.35	36

TABLE IV.3 Hydrogen

Cast	In $[\frac{ml}{100g}]$	Out $[\frac{ml}{100g}]$	E [%]
1	0.16	0.11	31
2	0.152	0.085	44
3	0.20	0.14	30
4	0.22	0.15	32

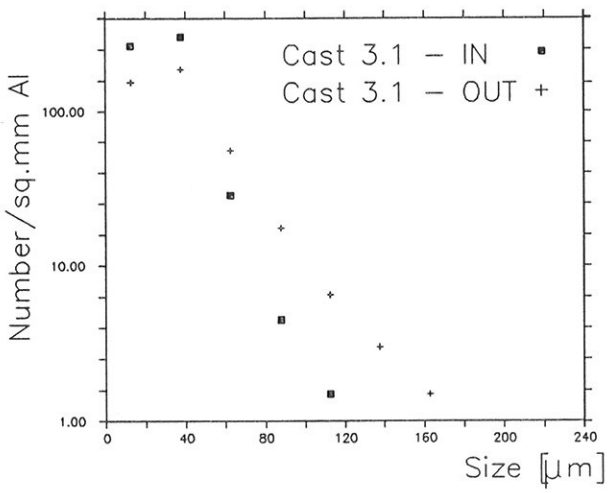

Figure 4.4. Number size distribution of films

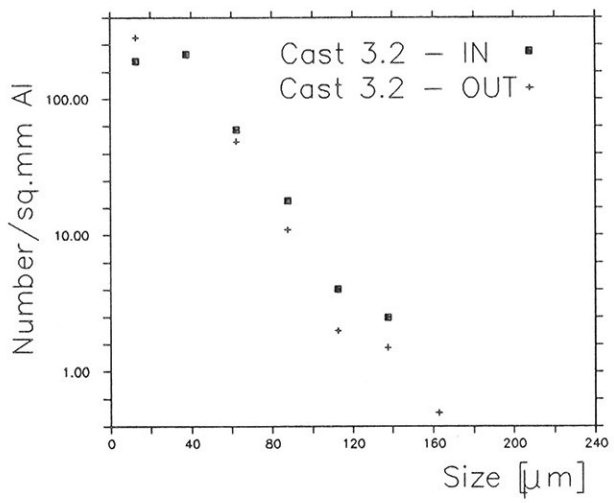

Figure 4.5. Number size distribution of films

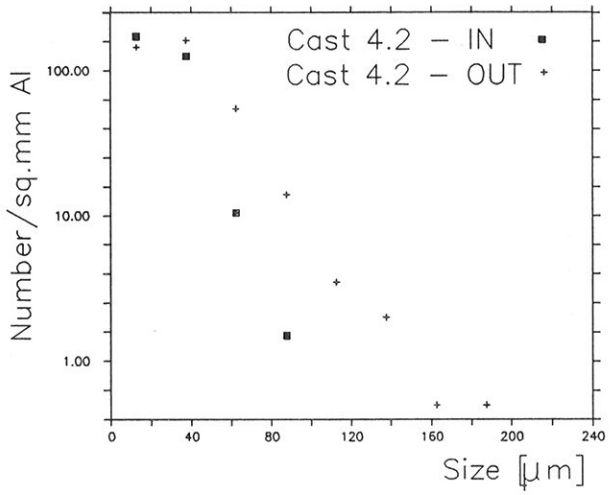

Figure 4.6. Number size distribution of films

4.6 Carbides

Tables IV.4 and IV.5 give total impurity levels before and after the 528-filter, and calculated filtration efficiencies.

TABLE IV.4 Carbide inclusions (in "pure" Al)

Cast	In [ppm]	Out [ppm]	E [%]
1.2	14.0	2.7	81
2.1	3.8	1.0	74

TABLE IV.5 Carbide inclusions (in Al + 4.6 w% Mg)

Cast	In [ppm]	Out [ppm]	E [%]
3.1	2.9	0.11	96
4.1	2.4	0.4	83

We observe an increase in filtration efficiency when the melt contains magnesium and the purge gas contains chlorine. If this increase in filtration efficiency should be ascribed to the fact that the filter is older and possibly clogged, then we would expect the oxide filtration efficiency to be high also. Table IV.2 does not indicate this. A probable explanation for the increase in carbide filtration efficiency is formation of salts leading to more favourable wetting conditions. Sticking of salts to oxide inclusions may have the undesirable effect of reducing their density. Then a smaller relative difference in density between oxide inclusions and melt, leads to a lower filtration efficiency (Eady et al. 1986). Sticking should not affect aluminium carbide inclusions in this manner as they already have a density close to the melt.

Figures 4.7 and 4.8 show examples of number size distributions. Notice that the scale on the y-axis is logarithmic while the x-axis is linear. The diagram shows that the number of inclusions drops exponentially with size. Sampling in itself bias distributions in both ends. There is a tendency to underestimate the number of smallest inclusions while the largest inclusions may be overestimated due to clustering and statistical overrepresentation.

Figures 4.9 and 4.10 show depth distributions down through Alcoa sampling filters. Notice the second peak at depth 1.8 mm in Fig. 4.9. An explanation for this peak is that particles deposited at the inlet of the filter have been re-entrained in the melt and then re-deposited.

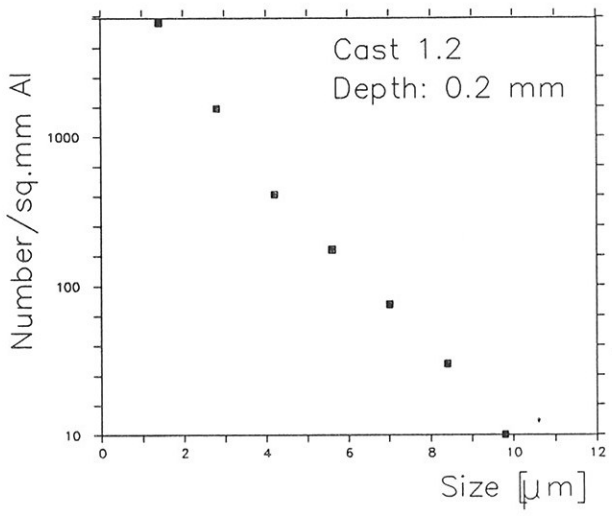

Figure 4.7. **Number size distribution of carbides in sampling filter**

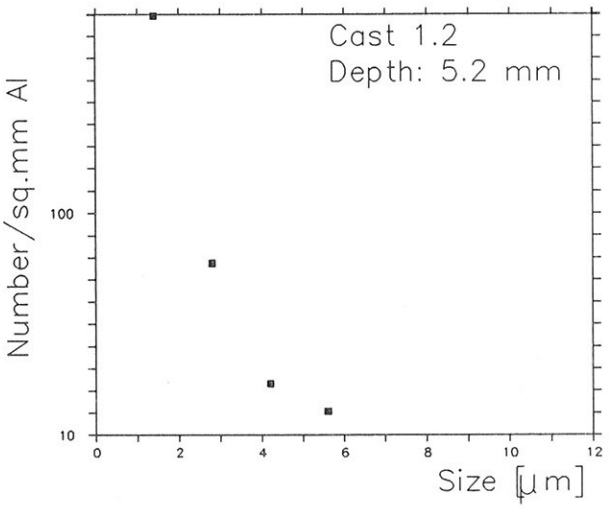

Figure 4.8. **Number size distribution of carbides in sampling filter**

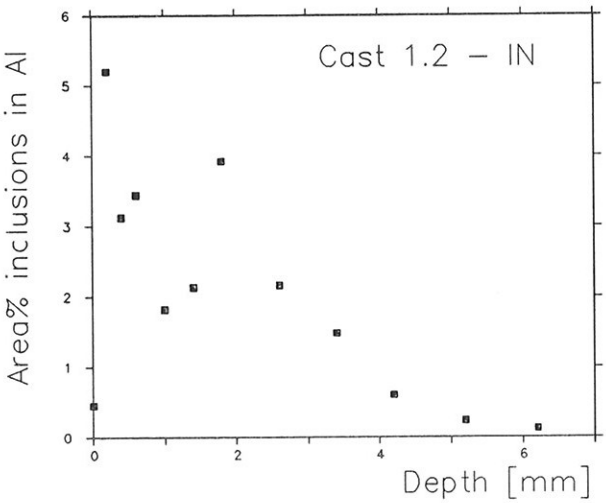

Figure 4.9. **Depth distribution of carbides in sampling filter**

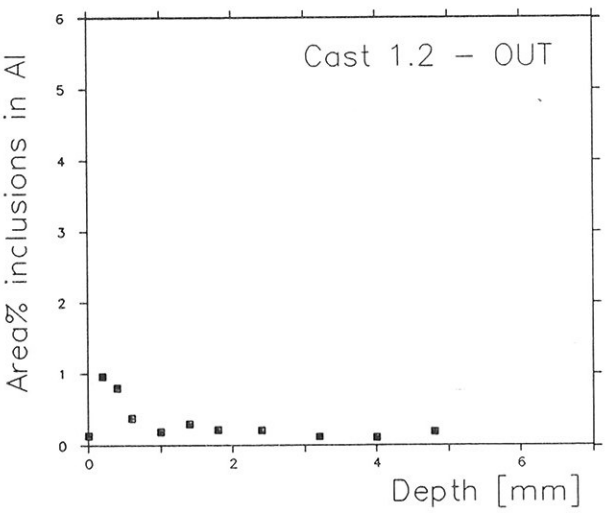

Figure 4.10. **Depth distribution of carbides in sampling filter**

4.6.1 Model for deposition in sampling filters

Depth Distributions

Let us consider a slice dx in the flow direction of a sampling filter of depth H. $\dot{q}$ is volume flow in cubic meter per second and c(x,r) is number of inclusions with radius r per cubic meter at a depth x. θ is fraction of inclusions deposited in dx. A number balance across dx gives:

$$-\dot{q}\ dc = \theta\ dx\ \dot{q}\ c \tag{4.1}$$

$$c(x,r) = c_o(r)\ e^{-\theta x} \tag{4.2}$$

$c_o(r)$ is the number size distribution per unit volume of inclusions entering the sampling filter. Note that c(x,r) is the number of inclusions per unit volume in the melt.

We have measured the number of inclusions deposited per unit volume melt and unit filter depth, A(x,r), giving the number balance:

$$c(x,r) = c_o(r) - \int_0^x A(x',r)dx' \tag{4.3}$$

Differentiation of Eq. (4.3) with respect to x and comparison with Eq. (4.2) gives:

$$A(x,r) = \theta\ c_o(r)\ e^{-\theta x} \tag{4.4}$$

This gives that depth distributions through a sampling filter are exponential with respect to depth x.

Number Size Distribution

When we know the number of inclusions of size r per unit volume melt and unit filter depth throughout the sampling filter, A(x,r), we can integrate over depth x:

$$\int_0^H A(x,r)dx = c_o(r) \tag{4.5}$$

$c_o(r)$ is the number size distribution per unit volume in the melt entering or leaving the industrial filter. This is consistent with the previous statement that $c_o(r)$ is the number size distribution of inclusions per unit volume entering the sampling filter.

Integrating once more, this time over size r, we get the total number of inclusions per unit volume in the melt:

$$\int_0^\infty c_o(r)dr = c \tag{4.6}$$

4.6.2 Industrial filter

By integrating A(x,r) over the entire depth of the sampling filter we get the inclusion number size distribution per unit volume melt before and after the industrial filter as shown in Figures 4.11 to 4.14. Points in parentheses have higher statistical uncertainty.

These figures confirm the assumption that number size distributions of inclusions in the melt are exponential in the size range we observe. Not only are distributions that enter the industrial filter exponential, but this is also the case for inclusions leaving the filter.

From this we calculate the filtration efficiency, E(r), for each size (-range) of inclusions. Table IV.6 lists E(r) for some casts.

We observe that filtration efficiencies increase with increasing inclusion size. Observations in size classes above no. 4 are less reliable than classes 1 to 4, so the points in parentheses are probably due to "clustering" or statistical overrepresentation.

TABLE IV.6 Filtration efficiency (E(r))

Cast	Size range [μm]							
	1.40	2.80	4.20	5.60	7.00	8.40	9.80	11.2
1.2	0.73	0.77	0.88	0.93	0.97	1	1	1
2.1	0.72	0.74	0.75	0.83	(0.50)	1	-	-
3.1	0.98	0.98	0.97	1	1	1	1	1
4.1	0.89	0.90	0.83	0.82	(0.75)	-	-	-

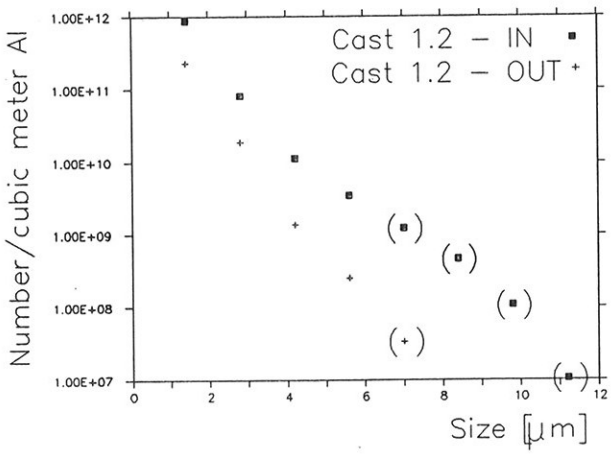

Figure 4.11. Number size distribution per unit volume melt of carbides in and out of the industrial filter

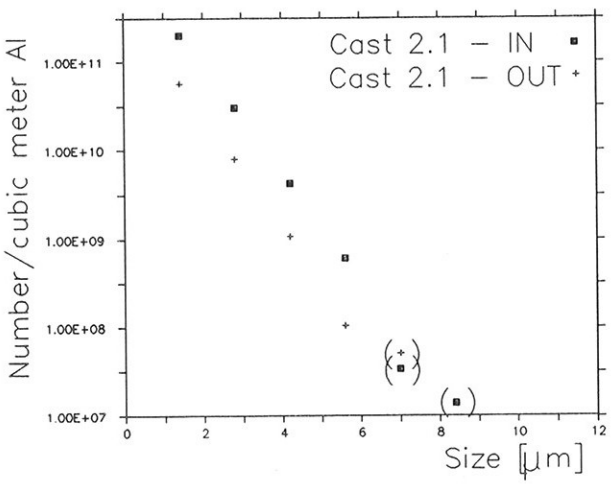

Figure 4.12. Number size distribution per unit volume melt of carbides in and out of the industrial filter

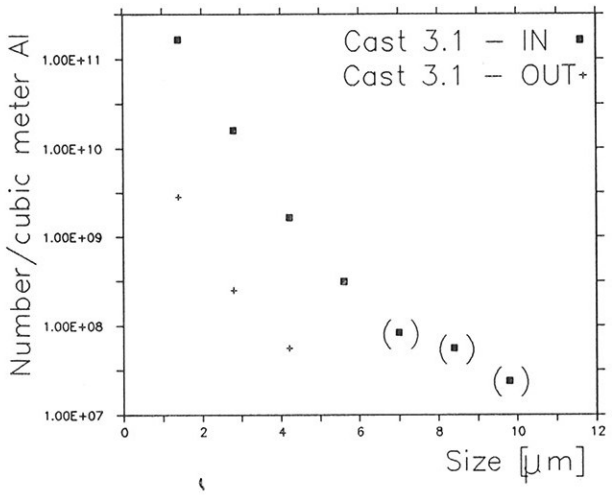

Figure 4.13. Number size distribution per unit volume melt of carbides in and out of the industrial filter

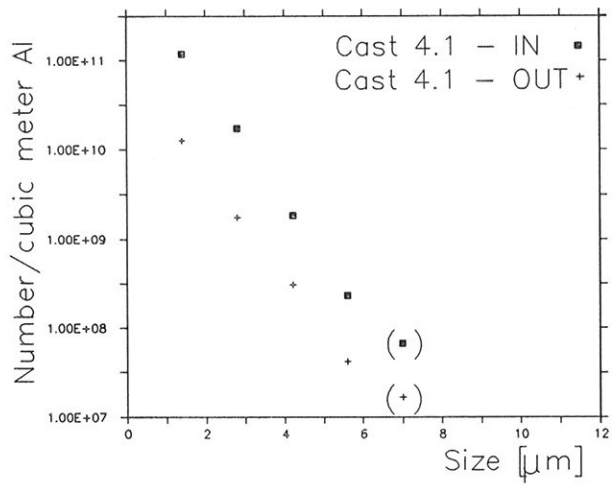

Figure 4.14. Number size distribution per unit volume melt of carbides in and out of the industrial filter

5 WETTABILITY AND ADHESION

In Chapter 2 a theoretical deduction of the effects of solved elements on interfacial tensions was presented. It will be shown that the final equations give reasonable results when compared to measurements taken from the literature. Compared to the equation given by Belton (1976) we find that he has to fit <u>two</u> parameters empirically while we only need to determine the free energy of adsorption empirically.

5.1 Interfacial tensions of pure systems

A number of investigators have measured the surface tension of pure aluminium. Some results are given in Table V.1. Values vary from 0.760 N/m (Rhee 1970) to 0.915 N/m (Körber and Löhberg 1971) at the melting point. This scatter is probably due to the strong affinity of aluminium for oxygen. The oxide, presumably Al_2O_3, would form at room temperature in air and remain in a meta-stable state on melting under vacuum. Surface tension data are usually obtained in vacuum of the order of 10^{-8} Pa with a liquid nitrogen cold trap. Goumiri and Joud (1982) report that under such normal vacuum conditions it was impossible to remove completely the oxide film covering the liquid aluminium droplet. Using Auger electron spectroscopy they determined the surface tension of aluminium as a function of oxide coverage.

TABLE V.1 Surface tension values of pure aluminium at melting point

Investigator	σ_{lv}^{P} [N/m]	$\frac{d\sigma_{lv}^{P}}{dT}$ [N/mK]
Rhee (1970)	0.760	-0.000202
Körber and Löhberg (1971)	0.915	-0.00051
Yatsenko et al. (1972)	0.865	-0.00016
Lang (1973)	0.855	-0.000104
Eustathopoulos et al. (1974)	0.860	-0.00019
Dawihl and Federmann (1974)	0.788	-0.000286
Lang et al. (1977)	0.865	-0.00015
Goumiri et al. (1979)	0.865	-0.00012

From Figure 5.1 it can be seen that the surface tension of pure aluminium is σ_{lv}^{P} = 1.050 N/m at 973 K. It is seen that the surface tension decreases strongly at initial oxidation and remains rather constant for coverages up to one monolayer. At this stage ($X \approx 1$) the measured surface tension is appreciably close to the mean value obtained by various investigators σ_{lv}^{P} = 0.865 N/m. It seems reasonable to admit that this mean value of σ_{lv}^{P} corresponds to the saturation of the surface layer by oxide. Thus the decrease of the surface tension would be due to the formation of oxide islands up to approximately the saturation coverage (by "an homogeneous oxide layer") of the liquid surface. When the oxide layer is present beyond a thickness of approximately one monolayer the surface tension decreases slightly as long as the oxide thickness still permits the drop to exhibit the fluidity characteristic of a molten metal.

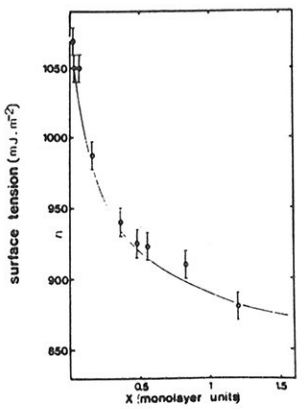

Figure 5.1 Aluminium surface tension versus oxide coverage (Goumiri and Joud 1982)

The wettability of Al_2O_3 single crystals and polycrystalline material by molten aluminium has been investigated by many authors (Livey and Murray 1955, Carnahan et al. 1958, Wolf et al. 1966, Brennan and Pask 1968, Champion et al. 1969, Sebo et al. 1973, and Dawihl and Federmann 1974). The results obtained show significant differences (Fig. 5.2), especially at temperatures below 1000 °C, which are probably caused by different experimental conditions of the various investigations. Brennan and Pask (1968) suspected that the characteristic sudden decrease of the contact angle at a specific temperature, as observed by many authors, is connected with the presence of an oxide layer on the metal surface.

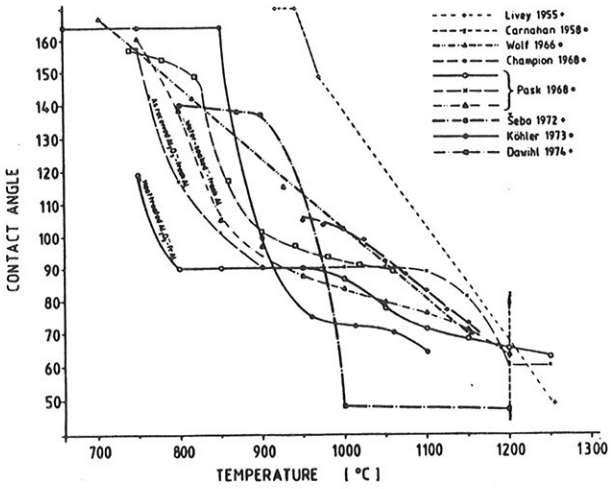

Figure 5.2 Contact angle in the system Al-Al_2O_3. Sessile drop experiments, vacuum. +, polycrystalline Al_2O_3; o, single crystal Al_2O_3 (John and Hausner 1986)

John and Hausner (1986) have investigated the influence of different oxygen partial pressures on the wetting behaviour in the system Al/Al_2O_3. Using different metal crucibles as oxide getters they obtained the wetting angles on Figure 5.3 (the metal/metal-oxide indicates crucible type). As can be seen at very low oxygen partial pressures in the region of 10^{-49} bar (i.e. 10^{-44} Pa) the wetting angle at 973 K was as low as 90°. Using Eq. (2.53) we find that

$$\sigma_{sl}^{p} = \sigma_{sv}$$

where σ_{sv} is the surface tension of the alumina solid.

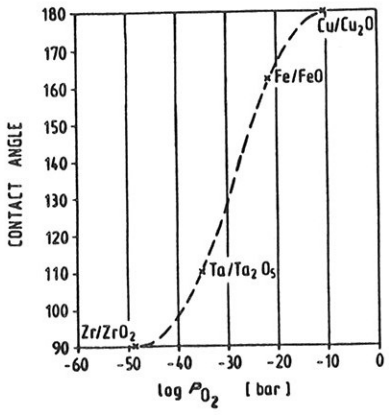

Figure 5.3 Contact angle and oxygen partial pressure (700°C, 2h.) (John and Hausner 1986)

Like Mehrotra and Chaklader (1985) we assume σ_{su} to be independent of oxygen partial pressure. On the other hand according to Brennan and Pask the nature of the sapphire surfaces is of critical importance for the surface tension measured. They claim that the value of 0.905 N/m reported by Kingery (1960), which was determined at 2073 K and low pressures, would be expected to correspond to the HTH-surface. A HTH-surface is an oxygen-deficient surface of some unknown thickness containing some AlO in a spinel-type structure. Other surface structures should have lower surface energies.

According to Campbell and Sherwood (1967) pure alumina may exist in several forms at low temperature, but all these forms are converted to high-temperature α-alumina (corundum) at temperatures from 750 to 1200 °C depending on time, crystal size, and atmosphere. Heating to temperatures above 1600 °C assures rapid conversion. The change to the α form is irreversible.

Most measurements of the surface tension of Al_2O_3 (regardless of surface structure) have been performed at elevated temperatures (Kingery 1960, Bondi 1953, Bruce 1965, Rasmussen and Nelson 1971, McLean and Hondros 1971). Rhee (1972) has developed a formula for the surface tension of $\alpha - Al_2O_3$ as a function of temperature:

$$\sigma_{sv} = 0.892 - 1.2 \cdot 10^{-4} T(°C) \qquad (5.1)$$

At 973 K this formula gives

$$\sigma_{sv} = \sigma_{sl}^{p} = 0.808 \ N/m$$

5.2 Surface tensions of "contaminated" systems

In Chapter 2 it was found that the effect of solved elements on the surface tension of a melt can be expressed as:

$$\sigma_{lv} = \sigma_{lv}^{p} - \frac{m_1}{A_1^{\sigma} m_2} \cdot \frac{RT}{b_2} \cdot \left(1 - \frac{f_1}{f_2} e^{\frac{\Delta G^{\circ}}{RT}}\right) \cdot \ln\left(b_2 \frac{f_2}{f_1} e^{\frac{-\Delta G^{\circ}}{RT}} \frac{[\%2]}{100} + 1\right) \qquad (2.71a)$$

where

$$b_2 = \frac{A_2^{\sigma} m_1}{A_1^{\sigma} m_2} - \frac{f_1}{f_2} e^{\frac{\Delta G^{\circ}}{RT}} \qquad (2.71b)$$

The free energy of adsorption, ΔG°, must be determined empirically. Above it was found that the surface tension of pure aluminium is 1.050 N/m. However, most investigators seem to have "pure" melts contaminated by oxygen. Incorporating this oxygen in the model would make the system a three-component type. Although possible, we feel that there is little to be gained by solving the more complicated three-component equation. The system will therefore

be treated as two-component in spite of the oxygen. Oxygen will be taken into account only through the use of the "pure" surface tension measured by the individual investigator.

To determine the free energy of adsorption of a solved element in aluminium the surface tension of "pure" aluminium and of contaminated aluminium, at a specific contamination level, must be known. Lang (1973, 1974) has measured the surface tension in a number of binary aluminium alloys. These data will be used to determine the free energy of adsorption. Only metals will be investigated. Lang's data are given as curve fitted functions of weight percent element added. Table V.2 lists Lang's functions.

When solving Eq. (2.71) one must know the surface area per mole of solvent and solute. It is assumed that there is no chemical reaction or formation of chemical compounds between solute and solvent. Surface areas are therefore calculated from metallic radii. The surface area per mole is then given by

$$A_i^o = \pi \cdot r_{met}^2 \cdot Avogadros\ number = \pi \cdot r_{met}^2 \cdot 6.022 \cdot 10^{23}$$

Metallic radii are listed in Table V.3.

For cobalt-, chromium-, gallium-, and iron-additions the surface tension increases with the additions, but the change is small. According to our model this is impossible because it would give a positive free energy of adsorption. The "driving force" in the model is the energy gain by moving atoms of component 2 from the bulk to the surface, i.e. a negative ΔG^o. Cobalt, chromium, gallium, and iron are therefore given a free energy of adsorption equal to zero.

Numerical calculations have been carried out to determine the free energy of adsorption for the rest of the elements. In this case ΔG^o has been calculated for two different weight percent

additions, and the mean value taken as the "correct" answer. These calculated free energies of adsorption are presented in Table V.4.

The surface coverage of component 2 can be determined by rearranging Eq. (2.71a):

$$\frac{[\%2]^{\sigma}}{100} = \left\{ 1 + \frac{f_1}{f_2} e^{\frac{\Delta G^{\circ}}{RT}} \left(\frac{100}{[\%2]} - 1 \right) \right\}^{-1}$$

In Table V.4 we have calculated the surface coverage at two weight percent component 2 in bulk.

TABLE V.2 Surface tension of aluminium as a function of weight percent added element. Data from Lang (1973, 1974) at 973 K.

Element	Surface tension (N/m)	Valid in range (w.%)
Antimony	0.862-0.06569*ln(11.43*x + 1)	0 - 0.7
Barium	0.862-0.08093*ln(37.87*x + 1)	0 - 0.5
Beryllium	0.851-0.00138*x	0 - 0.7
Bismuth	0.851-0.0862*ln(70.4*x + 1)	0 - 0.7
Cadmium	0.851-0.1083*ln(0.23*x + 1)	0 - 0.7
Calcium	0.862-0.04949*ln(3.93*x + 1)	0 - 0.5
Cerium	0.862-0.00405*x	0 - 1.0
Chromium	0.862+0.00940*x	0 - 0.5
Cobalt	0.862+0.00053*x	0 - 1.0
Copper	0.851-0.00212*ln(22.4*x + 1)	0 - 8.0
Gallium	0.862+0.00234*x	0 - 0.5
Indium	0.849-0.04693*x	0 - 0.7
Iron	0.851+0.00062*x	0 - 2.0
Lead	0.851-0.112*ln(11.8*x + 1)	0 - 0.8
Lithium	0.862-0.13908*ln(9.06*x + 1)	0 - 0.6
Magnesium	0.851-0.04190*x	0 - 1.5
Manganese	0.851-0.00066*x	0 - 1.6
Nickel	0.851-0.00005*x	0 - 0.7
Silver	0.862-0.00743*x	0 - 5.0
Strontium	0.862-0.03784*ln(46.09*x + 1)	0 - 0.4
Thallium	0.851-0.1653*ln(4.62*x + 1)	0 - 0.5
Tin	0.851-0.0922*ln(0.98*x + 1)	0 - 2.0
Titanium	0.862-0.01284*x	0 - 0.2
Vanadium	0.862-0.0105*x	0 - 0.3
Zinc	0.842-0.00144*x	0.3 - 60
Zirconium	0.862-0.00340*x	0 - 0.25

TABLE V.3 Physical data for the elements added (Aylward and Findlay 1978)

Element	Metallic radius (Å)	Atomic weight	Electronegativity (Pauling scale)
Aluminium	1.43	26.98	1.61
Antimony	1.45	121.75	2.05
Barium	2.17	137.34	0.89
Beryllium	1.12	9.01	1.57
Bismuth	1.55	208.98	2.02
Cadmium	1.49	112.40	1.69
Calcium	1.97	40.08	1.00
Cerium	1.83	140.12	1.12
Chromium	1.25	52.00	1.66
Cobalt	1.25	58.93	1.88
Copper	1.28	63.55	1.90
Gallium	1.22	69.72	1.81
Indium	1.36	114.82	1.78
Iron	1.24	55.85	1.83
Lead	1.75	207.20	2.33
Lithium	1.52	6.94	0.98
Magnesium	1.60	24.31	1.31
Manganese	1.37	54.94	1.55
Nickel	1.25	58.71	1.91
Silver	1.44	107.87	1.93
Strontium	2.15	87.62	0.95
Thallium	1.70	204.37	2.04
Tin	1.51	118.69	1.96
Titanium	1.45	47.90	1.54
Vanadium	1.31	50.94	1.63
Zinc	1.33	65.38	1.65
Zirconium	1.59	91.22	1.33

TABLE V.4 The free energy of adsorption and the equivalent surface coverage of solute at 2 weight percent solute in bulk

Element	ΔG° (J/mol)	$[\%2]^\sigma$ (%)
Antimony	-55 163	64.7
Barium	-70 661	92.6
Beryllium	- 3 670	0.3
Bismuth	-72 513	93.9
Cadmium	-31 972	9.4
Calcium	-38 180	22.5
Cerium	-20 430	2.4
Chromium	0	0.2
Cobalt	0	0.2
Copper	-19 985	2.3
Gallium	0	0.2
Indium	-37 091	16.4
Iron	0	0.2
Lead	-66 916	88.7
Lithium	-39 224	20.4
Magnesium	-24 677	4.1
Manganese	- 3 999	0.3
Nickel	- 433	0.2
Silver	-22 256	3.0
Strontium	-55 753	66.4
Thallium	-64 567	85.4
Tin	-42 534	27.8
Titanium	-21 166	2.7
Vanadium	-19 246	2.1
Zinc	- 8 803	0.6
Zirconium	-16 937	1.6

The question then arises how well does the theoretical function for the surface tension fit the experimental data? Figures 5.4 - 5.5 show examples of very good fit within the range of weight percents where Lang's data are valid. The other elements are given in appendix A. Engh has investigated binary systems of iron, nickel, copper, silver, and cobalt as solvents and sulphur, oxygen, tellurium, and selenium as solutes, and obtained good agreement between the theory and experimental data.

Note that for zinc the experimental data are not valid for [%Zn] < 0.3. According to Lang (1973, p. 234) the surface tension of zinc drops strongly from 0 to 0.3 weight percent zinc and is linear thereafter. The free energy of adsorption calculated from Eq. (2.71) from the function given by Lang is therefore too low. If this drop, in the range 0 to 0.3 w.% Zinc, is used ΔG° = -29 150 J/mol.

As can be seen from Figure 5.6 it seems as though the theoretical function does not fit the data well for copper. Naidich, Eremenko and Kiritschenko (1962) have measured the effect of copper on the surface tension of aluminium and claim that copper is inactive. Also Korolkow (1956), Korolkow and Bytschkowa (1960), and Korolkow and Igumnowa (1961) have found that up to about 7 weight percent copper there is no effect on the surface tension of aluminium. These data would give a free energy of adsorption equal to zero for copper.

To test the model the free energy of adsorption has been varied as $\Delta G^\circ \pm 20\% \cdot \Delta G^\circ$. Based on these values surface tensions have been calculated from Eq. (2.71). The results have been plotted in Figures 5.4 - 5.6 and Figures A.1 -A.20. This sensitivity analysis shows, not surprisingly, that a variance of +/- 20% in ΔG° have the largest effect on the surface tension of the most surface active elements.

Table V.5 lists the maximum error, compared to Lang's data, in the theoretical surface tension for + 20% and - 20% in the free energy of adsorption respectively. Naturally the error increases with increasing weight percent addition, and the largest errors are found for the maximum weight percent valid. Underestimating the free energy of adsorption in most cases give a far lower error in the calculated surface tension.

If the free energy of adsorption is plotted as a function of metallic radius, as in Figure 5.7, there seems to be an increase in ΔG° with increasing r_{met}. Be aware that the neglected parameter $\kappa = A_1^\sigma / A_2^\sigma$ (see Section 2.2) is proportional to r_{met}^{-2}. The relationship between ΔG° and r_{met} could partly be due to κ.

Plotting ΔG° as a function of electronegativity (Figure 5.8) shows that the free energy of adsorption increases with increasing difference between the elements electronegativity and aluminiums electronegativity. Three branches may be identified - a) elements with lower electronegativity than aluminium, b) elements with higher electronegativity than aluminium and low free energy of adsorption, and c) same as b), but higher free energy of adsorption.

Finally we have investigated a possible connection between the free energy of adsorption and the surface tension of the pure elements at their melting points. (Data from Iida and Guthrie (1988, p. 134).) Figure 5.9 shows elements with a electronegativity lower than aluminium. In the bottom of the "well" we find manganese with a surface tension of 1.090 N/m, very close to the surface tension of pure aluminium. A lower surface tension of pure element leads to higher adsorption, through decreasing the surface tension of the binary system.

TABLE V.5 Maximum error in surface tension when the free energy of adsorption is varied

Element	Error (%) (+20% in ΔG°)	Error (%) (-20% in ΔG°)	Weight percent at maximum error
Antimony	28	9	0.7
Barium	18	15	0.5
Beryllium	0	0	0.7
Bismuth	42	21	0.7
Cadmium	2	1	0.7
Calcium	7	3	0.5
Cerium	0	0	1.0
Chromium	1	1	0.5
Cobalt	0	0	1.0
Copper	3	0	2.0
Gallium	0	0	0.5
Indium	5	2	0.7
Iron	0	0	2.0
Lead	26	18	0.8
Lithium	19	12	0.6
Magnesium	4	3	1.5
Manganese	0	0	1.6
Nickel	0	0	0.7
Silver	1	1	2.0
Strontium	13	7	0.4
Thallium	23	15	0.5
Tin	17	5	2.0
Titanium	0	0	0.2
Vanadium	0	0	0.3
Zinc	0	0	2.0
Zirconium	0	0	0.25

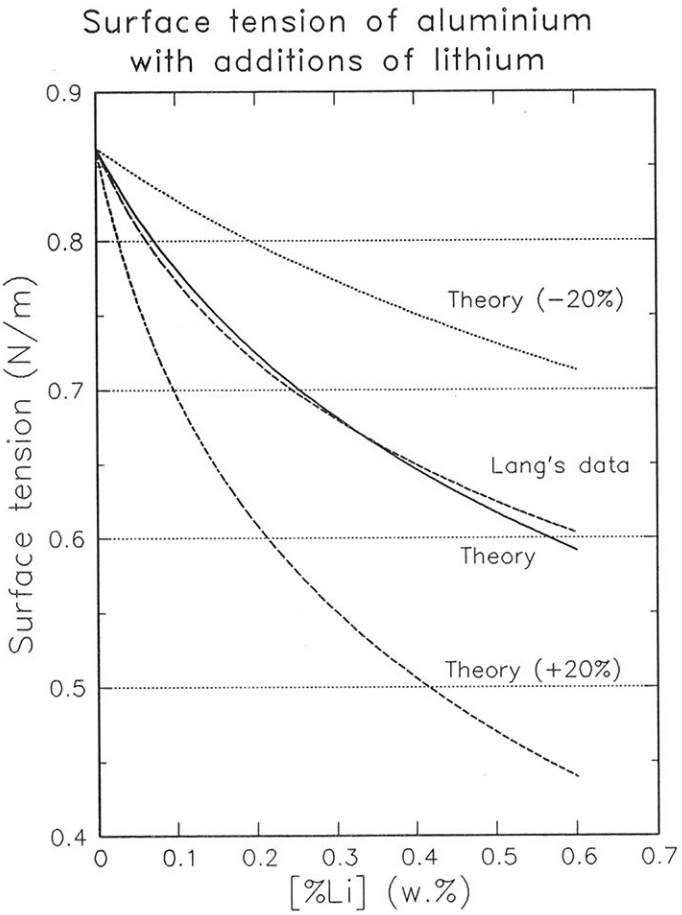

Figure 5.4 Surface tension of aluminium with lithium additions. Curves for free energy of adsorption 20 % too high and too low are shown.

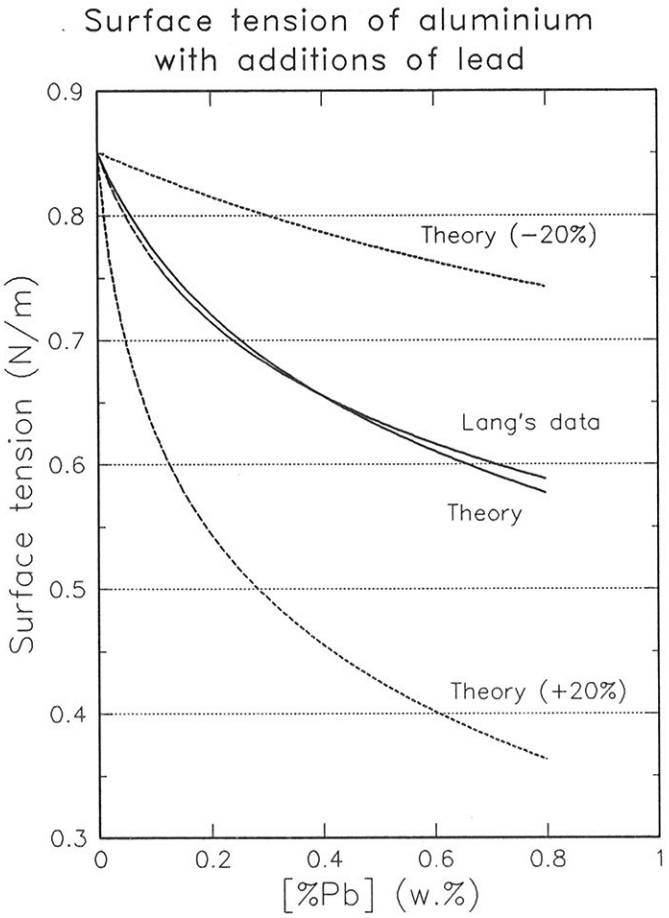

Figure 5.5 Surface tension of aluminium with lead additions. Curves for free energy of adsorption 20 % too high and too low are shown.

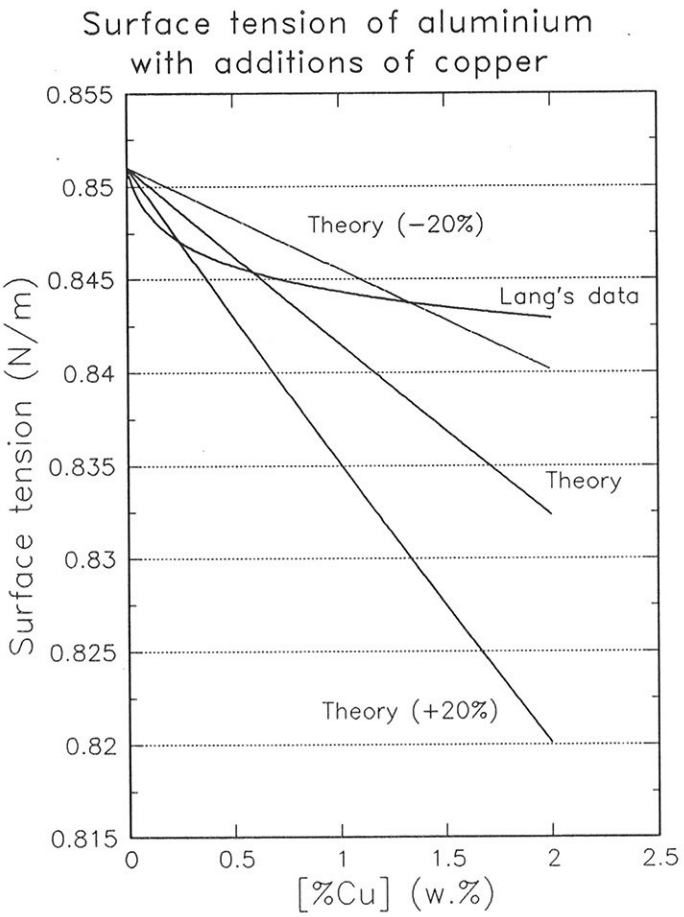

Figure 5.6 Surface tension of aluminium with copper additions. Curves for free energy of adsorption 20 % too high and too low are shown.

Elements with a higher electronegativity than aluminium are shown in Figure 5.10 as a function of the surface tension of the pure element at its melting point. Previously it was found that there are two possible values for zinc and copper, so both values are plotted . In the figure it is distinguished between elements with a metallic radius less than or larger than copper. Depending on which value is correct copper belongs to either group. For elements larger than copper it is seen that the free energy of adsorption increases with decreasing surface tension of the pure element, when the surface tension of the pure element is less than the surface tension of pure aluminium.

In conclusion we may say that elements with a **lower electronegativity** than aluminium are driven to the surface because there they may find free electrons. This is valid for elements of all sizes even though the elements larger than aluminium are the less willing to be hemmed in by the smaller aluminium atoms in the bulk melt. If the surface tension of the pure element is lower than for pure aluminium increased amounts of this element at the surface of the binary aluminium melt will contribute to lowering the surface tension. The surface looks more and more like the surface of the added element.

For elements with a **higher electronegativity** than aluminium the size of the element becomes important. Elements with a metallic radius less than copper (1.28 Å) fit easily in between the aluminium atoms in the bulk. Also , due to their higher affinity for electrons, they prefer the bulk. Elements with a metallic radius higher than 1.28 Å are driven to the surface because of their size. The free energy of adsorption increases with decreasing surface tension of the pure added element at its melting point for the same reason as mentioned above.

We may now estimate the effect of "unknown" metallic elements on the surface tension of aluminium. All the information needed is

the electronegativity, less than or higher than 1.61 (Pauling's scale), and the metallic radius, less than or higher than 1.28 Å, and the surface tension of the pure element at its melting point.

As an example estimate the free energy of adsorption of sodium. Sodium has an electronegativity of 0.93, i.e. less than aluminium. Figure 5.9 should be used. The metallic radius does not matter in that case. Sodium has a surface tension of 0.191 N/m at its melting point. An estimated free energy of adsorption would then be about -100 000 J/mol. Another example could be gold with r_{met} = 1.44 Å, electronegativity = 2.54, and surface tension of pure element = 1.169, giving $\Delta G^{\circ} \approx$ -20 000 J/mol.

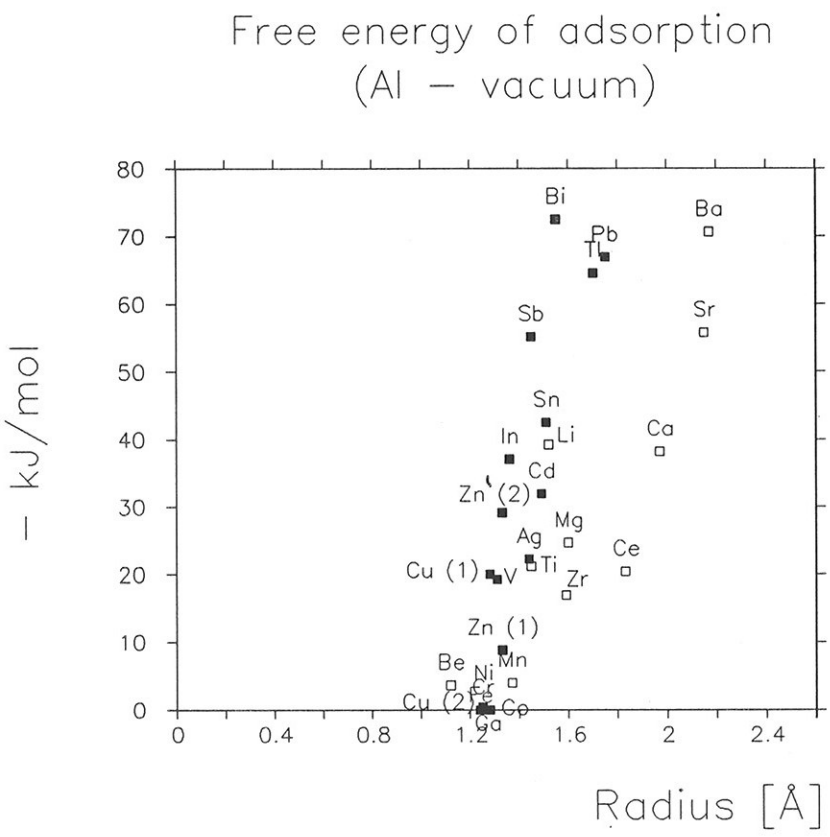

Figure 5.7 **Free energy of adsorption as a function of metallic radius. Filled markers denote elements with electronegativity higher than aluminium. Non-filled markers elements with electronegativity lower than aluminium.**

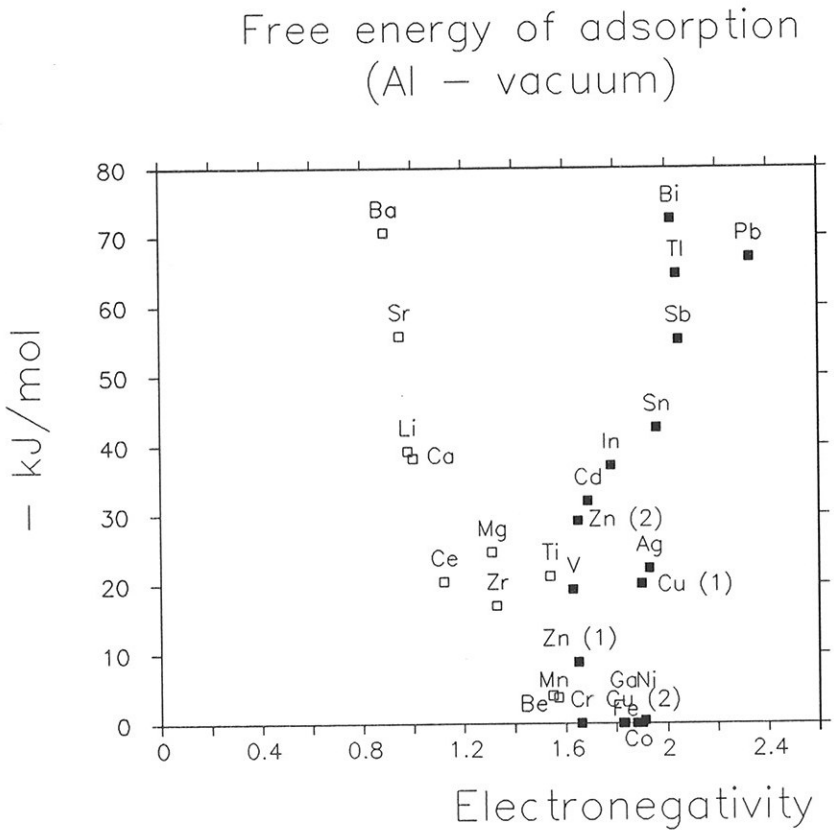

Figure 5.8 Free energy of adsorption as a function of electronegativity. Filled markers denote elements with electronegativity higher than aluminium. Non-filled markers elements with electronegativity lower than aluminium.

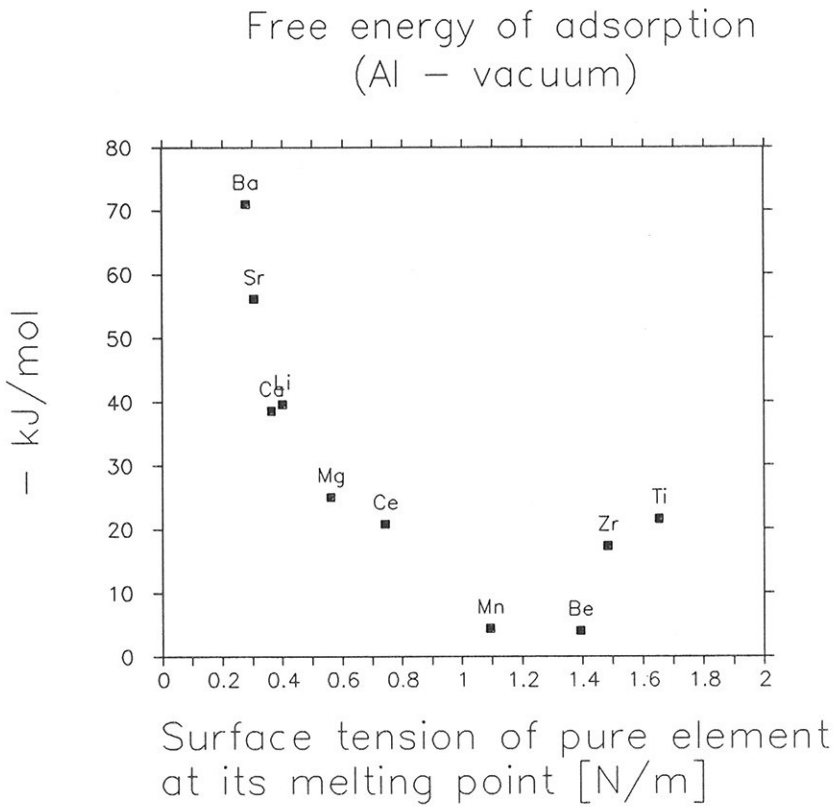

Figure 5.9 **Free energy of adsorption as a function of surface tension of pure element. Elements with lower electronegativity than aluminium.**

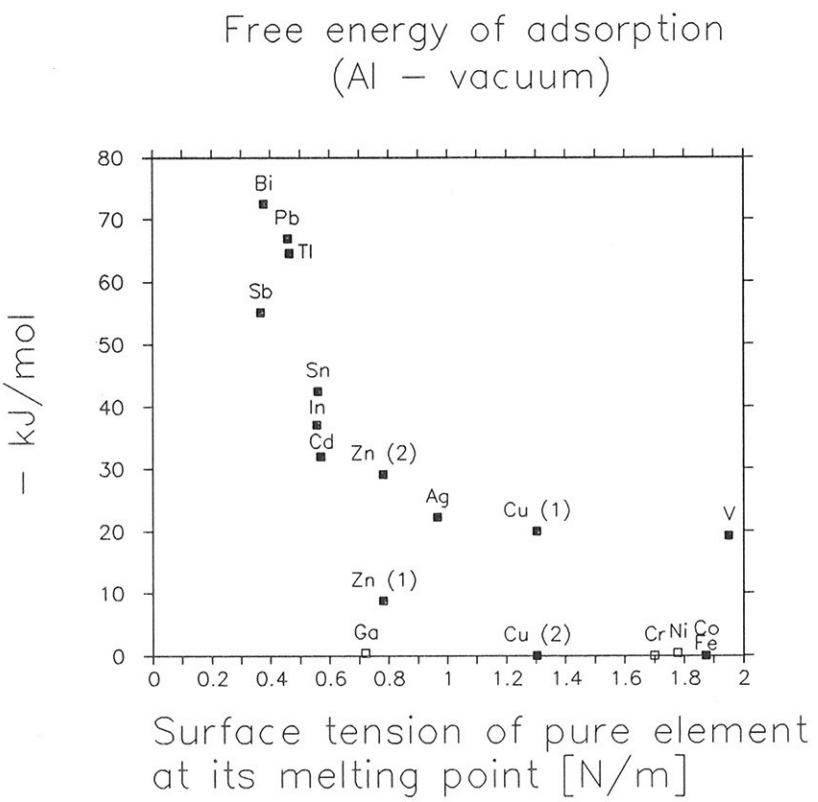

Figure 5.10 Free energy of adsorption as a function of surface tension of pure element. Elements with higher electronegativity than aluminium. Filled markers denote elements with metallic radius larger than copper. Non-filled markers elements with metallic radius less than copper.

5.3 Interfacial tensions of "contaminated" systems

Interfacial tensions between a metal and a solid are usually measured indirectly via the contact angle (wetting angle). σ_{sl} must then be determined from Young's equation:

$$\sigma_{sl} = \sigma_{sv} - \sigma_{lv} \cdot \cos\theta \qquad (2.53)$$

This means that the surface tension of the crystal and the surface tension of the melt must be known. We investigate the system alumina in contact with aluminium. In this case the surface tension of the crystal is given by Eq. (5.1). At 870°C this gives σ_{sv} = 0.788 N/m and at 950°C σ_{sv} = 0.778 N/m. The temperature dependence of the surface tension of aluminium is also taken from Rhee (1972):

$$\sigma_{lv}^{p} = 0.999 - 2.02 \cdot 10^{-4} \cdot T(°C) \quad N/m \qquad (5.2)$$

The effect of the added element on the surface tension of aluminium will be taken from Lang (1973, 1974) at 700°C. Effects of temperature and added elements are added algebraically.

Only a few investigators have looked at binary systems of aluminium in contact with alumina: Wolf et al. (1966), at 870°C, and Köhler (1975), at 950°C. Tertiary and higher systems have been investigated by Lijun et al. (1990).

Table V.6 gives the experimental contact angles measured by Wolf et al. and Köhler. The interfacial tension between alumina and aluminium has been calculated according to the above presented procedure. Wolf et al. measured the contact angle at 870°C and a vacuum of 10^{-4} torr. The lowest contact angle was obtained with the aluminium-magnesium alloy melted in a vacuum of $5 \cdot 10^{-5}$ torr (Mg(b) in Table V.6).

TABLE V.6 The interfacial tension for some binary systems of aluminium in contact with alumina at 870°C (* at 950°C)

Element	w. %	σ_{lv} (N/m)	θ (°)	σ_{sl} (N/m)
Cu	0.54	0.812	119	1.182
Mg (a)	0.85	0.781	118	1.155
Mg (b)	0.85	0.781	94	0.842
Zr	0.44	0.827	118	1.176
Pb	0.15	0.703	139	1.319
V	0.49	0.823	139	1.409
Mn	1.07	0.816	137	1.385
Bi	0.92	0.456	134	1.105
Cu *	1.00	0.810	76	0.582

We need to know the surface tension of "pure" aluminium in contact with alumina before we can calculate the free energy of adsorption. Wolf et al. measured a contact angle of 139° and Köhler 88° for pure aluminium. Using Young's equation it is found that:

$$\sigma_{sl}^{p} = 1.578 \ N/m \qquad (Wolf \text{ et } al.)$$

$$\sigma_{sl}^{p} = 0.750 \ N/m \qquad (Köhler)$$

Eq. (2.72) is then used to determine the free energy of adsorption, ΔG°, empirically. The results are presented in Table V.7.

The number of data points are much lower than in the case with the surface tension, but if we treat the free energy of adsorption in the same manner as in the previous section we see the same trends. Figures 5.11 - 5.14 show the free energy of adsorption

TABLE V.7 The free energy of adsorption for some binary systems of aluminium in contact with alumina at 870°C (* at 950°C)

Element	ΔG° (J/mol)	$[\%2]^{\circ}$ (%)
Cu	-69 088	74.2
Mg (a)	-61 528	56.5
Mg (b)	-77 606	87.6
Zr	-79 002	89.1
Pb	-90 133	96.3
V	-55 927	41.9
Mn	-51 246	30.6
Bi	-82 935	92.5
Cu *	-53 733	28.3

as a function of radius, electronegativity, and surface tension of the pure element at its melting point. The analogy with Figures 5.7 - 5.10 can be seen.

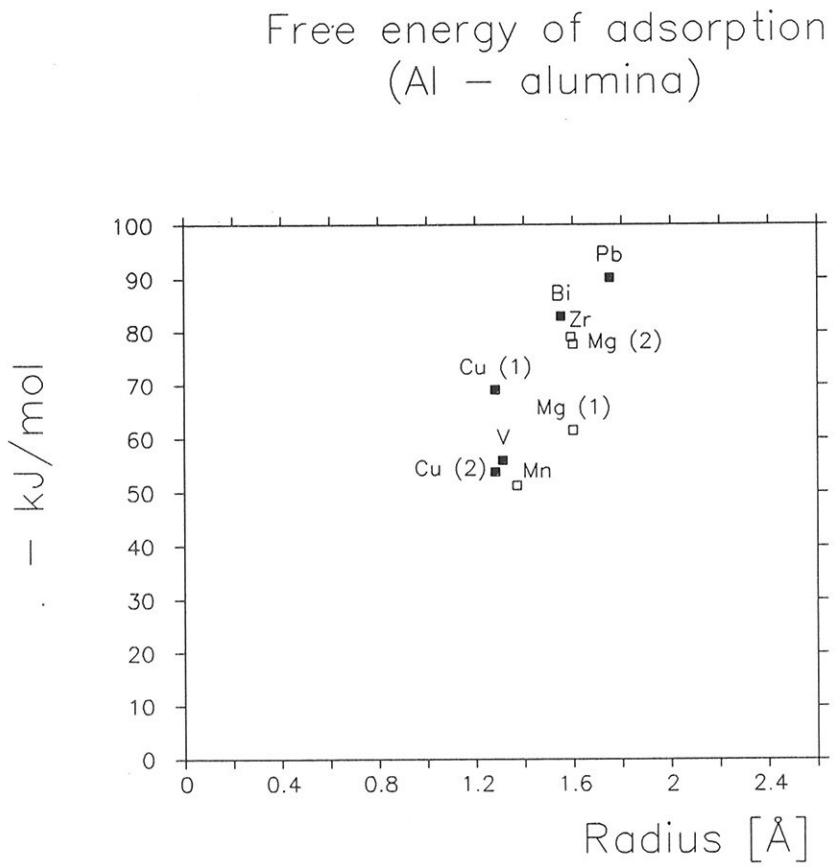

Figure 5.11 Free energy of adsorption as a function of metallic radius. Filled markers denote elements with electronegativity higher than aluminium. Non-filled markers elements with electronegativity lower than aluminium.

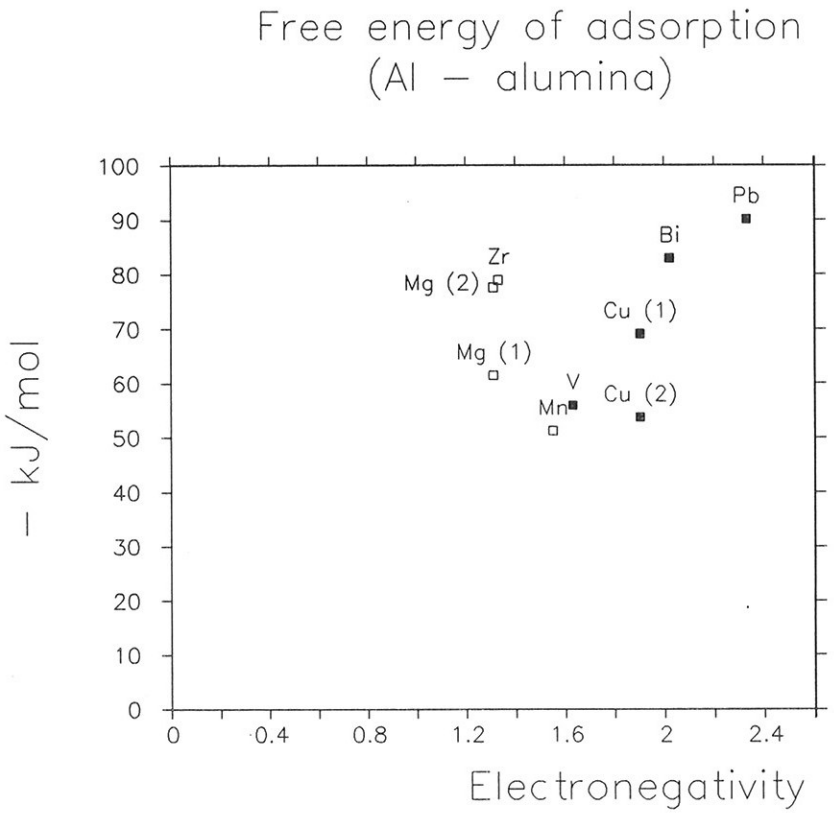

Figure 5.12 Free energy of adsorption as a function of electronegativity. Filled markers denote elements with electronegativity higher than aluminium. Non-filled markers elements with electronegativity lower than aluminium.

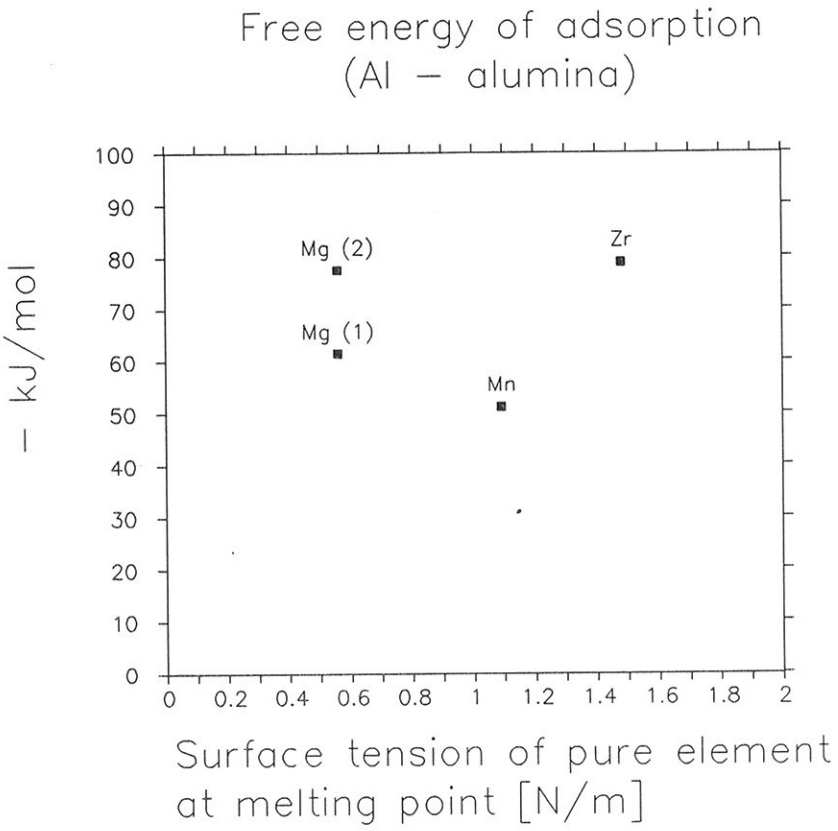

Figure 5.13 Free energy of adsorption as a function of surface tension of pure element. Elements with lower electronegativity than aluminium.

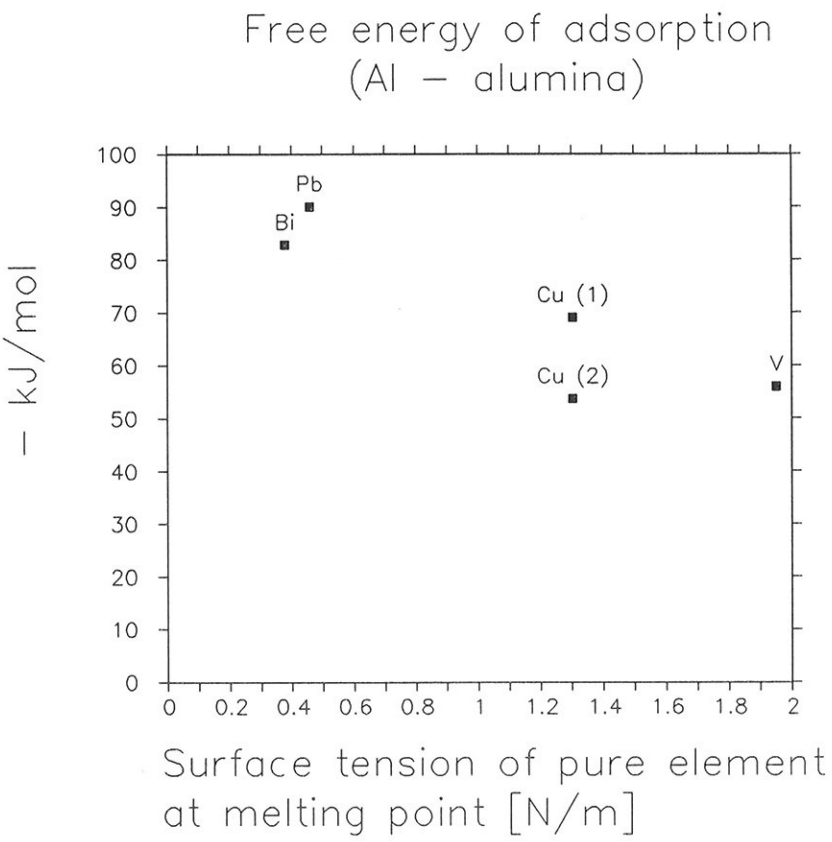

Figure 5.14 Free energy of adsorption as a function of surface tension of pure element. Elements with higher electronegativity than aluminium.

5.4 Solid-solid interaction

In the event of an inclusion resting on a filter surface we have to consider forces acting between two solids. There are two types of forces acting between the solids: (1) physical interactions which combine polarization and dispersion forces and (2) chemical forces, both ionic and homopolar. The basic difference, of significance here, between these two types of forces is their magnitude. The bond energies of physical (van der Waals) forces are functions or units of kJ/mol. The energies of chemical interaction equal tens and hundreds of kJ/mol (Naidich 1981).

Bowden and Young (1951) found that: "if surface layers are removed so that intimate contact occurs between the atoms of the two metal surfaces, we may expect the strength of the junction to approach that of the bulk metal". As soon as clean surfaces were allowed to touch each other, "complete seizure occurred even at room temperature." It seems reasonable that the same should happen if for example an oxide crystal intimately contacts another oxide.

Variables which influence the adhesion mechanisms are many. Corn (1961) reviewed adhesion process variables thought to be pertinent to small particle adhesion. Some of these effects that are believed to affect adhesion for particle and surface immersed in a melt are briefly presented below.

The London-van der Waals forces for a sphere adhering to a flat plate is

$$F = \frac{H \cdot r_p}{6 \cdot h^2}$$

Here H is the Hamaker constant, h is the separation distance, and r_p is the particle radius. The Hamaker constant is determined by the nature of the two interacting materials. According to van den Tempel (1972) the value of the Hamaker constant for any

given material must be obtained from atomic properties by means of not-to-well confirmed theory, and by using the assumption that these properties are not affected by combining the isolated atoms in a condensed material. No reliable theory is available for estimating the effective Hamaker constant in a system containing several different kinds of material.

Particle size, particle shape, and contact area affect adhesion. For example the contact area may be 1/10000 of the apparent area.

The effect of time of contact on adhesion has not been found for small particle adhesion. For a steel ball 0.32 cm in diameter on an indium block with 500 g load, Bowden and Tabor (1950) report full adhesion was reached in 2000 seconds. It is difficult to extrapolate these data to micron size particles where essentially no load is applied.

Buzagh (1930, 1931) allowed two to three micron quartz particles from a poly-disperse water suspension to settle on a tiltable glass plate. By inclining or inverting the plate the adhesion forces could be calculated from particle mass. The settled particles on the plate were observed to be in vivid random motion, due, presumably, to a buffer water film between particle and surface. Buzagh estimated the adhesion force for spherical particles to be $0.3 \cdot 10^{-3}$ N/m, which is lower than adhesion observed in air by many investigators.

6 DISCUSSION

6.1 Drag versus surfaces forces

In Section 2.4 an expression for the energy gained by moving an inclusion from suspension in the melt to a position on the filter surface is given. Rewritten in terms of a dimensionless length, $x = R_L/H_S$:

$$\begin{aligned}\Delta E_{tot} &= \pi R_L^2(\sigma_{sl} - \sigma_{sv})\frac{2x-1}{x^2} \\ &+ 2\pi R_L^2(\sigma_{pl} - \sigma_{pv})\frac{1}{x} \\ &- 2\pi R_L\frac{\sqrt{2x-1}}{x}\left(\frac{R_L}{x} + D\right)\sigma_{lv} \\ -(p_{atm} + \rho g H)&\left[\pi\frac{R_L^2}{x^2}\left(R_L - \frac{3}{2}\frac{R_L}{x}\right) + \pi R_L^2 D\frac{2x-1}{x^2}\right] \end{aligned} \quad (6.1)$$

The force pressing the particle against the filter is non-dimensionalised by diving with $2\pi R_L\sigma_{lv}$:

$$\frac{F}{2\pi R_L\sigma_{lv}} = -\frac{\sqrt{2x-1}}{x} - \frac{p_{atm}+\rho g H}{2\sigma_{lv}}R_L\frac{2x-1}{x^2} \quad (6.2)$$

Figure 6.1 shows this force as a function of x for a 5 μm radius particle. It is seen that at first it is a strongly decreasing function of x, but after x~=100 it is nearly constant. Another force acting on the particle is the drag force. Non-dimensionalised it becomes:

$$\frac{F_D}{2\pi R_L\sigma_{lv}} = 1.7009\cdot 3\ \frac{\mu v}{\sigma_{lv}} \quad (6.3)$$

Inserting numbers, using a melt flow velocity v = 1 cm/s, gives the non-dimensionalised drag force equal to $5.44 \cdot 10^{-5}$. This is several orders of magnitude smaller than the force pressing the particle towards the filter. In other words, if a four-phase contact between particle, filter, melt, and gas/vacuum is achieved the particle sticks to the wall. Larger forces than mere drag forces are necessary to remove it.

On the other hand it is well known that filter releases are common when filtering aluminium. One possible explanation is that it takes some time to establish the four-phase contact. In the mean time the particles "float" on a thin melt film between particle and filter. To establish the four-phase contact gas or vacuum or salt must be present. For example due to the presence of hydrogen in solution in the melt it may be possible to create a gas pocket. This means that the hydrogen must diffuse through the melt to the area occupied by the melt film.

Diffusion is a slow process. In the mean time the particles can be re-entrained into the melt by sudden filter surges or pressure variations or other sudden changes in flow conditions. Particles already in a four-phase contact exposed to the same filter surges will remain on the filter.

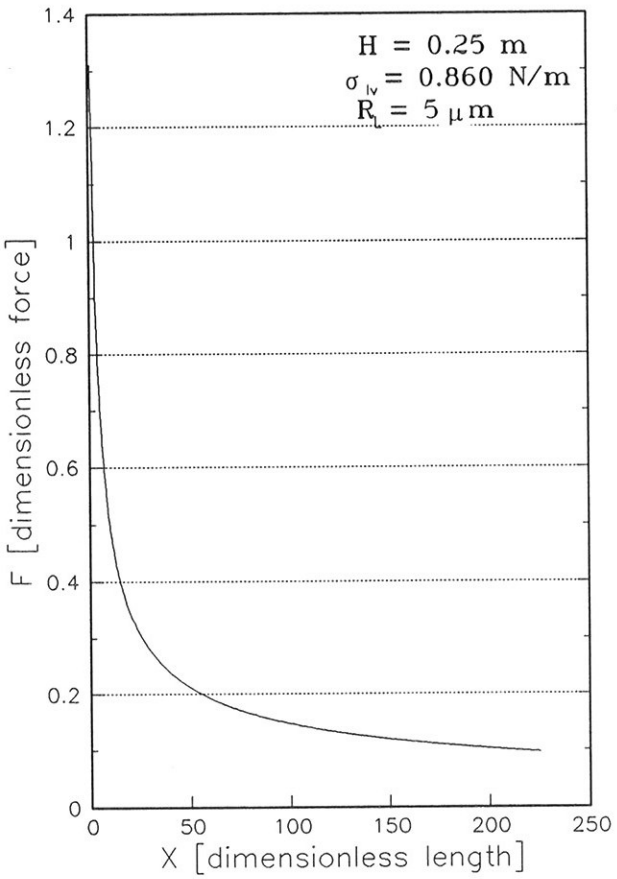

Figure 6.1 Force pressing particle against filter as a function of x (= R_L/H_s, Fig. 2.10).

6.2 Water model experiments

In order to study the interception mechanism "neutrally" buoyant polystyrene particles in water were used. Figure 6.2 shows the filtration efficiency for these particles as a function of approach velocity v. Figure 6.3 shows the filtration efficiency as a function of Reynolds number based on interstitial velocity, i.e.

$$Re = \frac{(v/\epsilon)\cdot d_c}{\nu}$$

It is seen that filtration efficiency drops with velocity in the lower velocity range below 0.6 cm/s. For this velocity range the filtration mechanism may be explained by buoyancy effects - in spite of the use of supposedly neutrally buoyant particles. Rough measurements give a settling velocity of 0.06 cm/s. A correction due to wall effects give a settling velocity 0.035 cm/s. Using the following theory 0.035 cm/s gives the "exponentially" decreasing filtration efficiency curve shown in Figure 6.2 for cylindrical collectors with a porosity of 0.61. The increasing filtration efficiency curve is the theoretical curve for removal by direct interception, where the effect of the boundary layer has been taken into account. On Figure 6.2 the measured filtration efficiencies for cylindrical collectors and collectors with a quadratic cross-section are shown. It is seen that these measurements lie below the calculated curve.

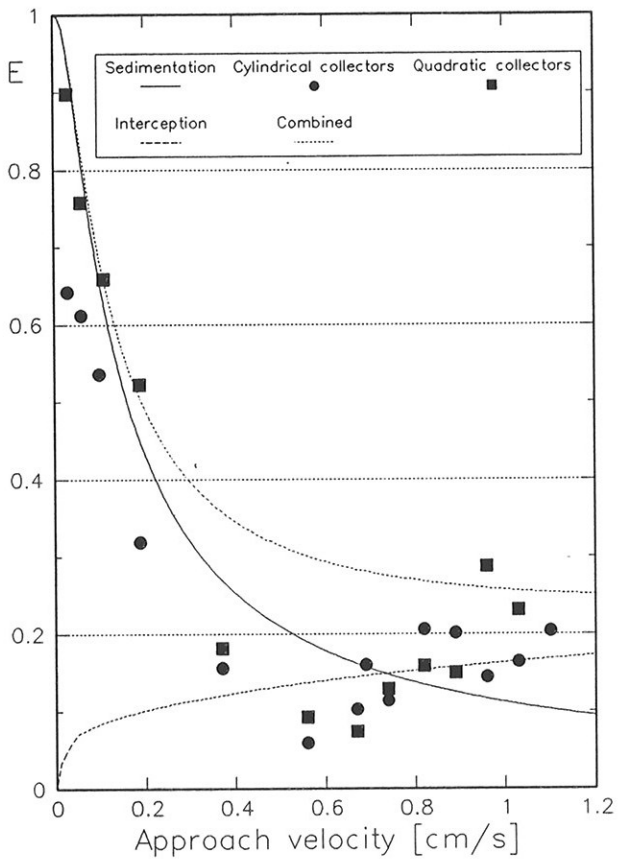

Figure 6.2 Filtration efficiency versus approach velocity

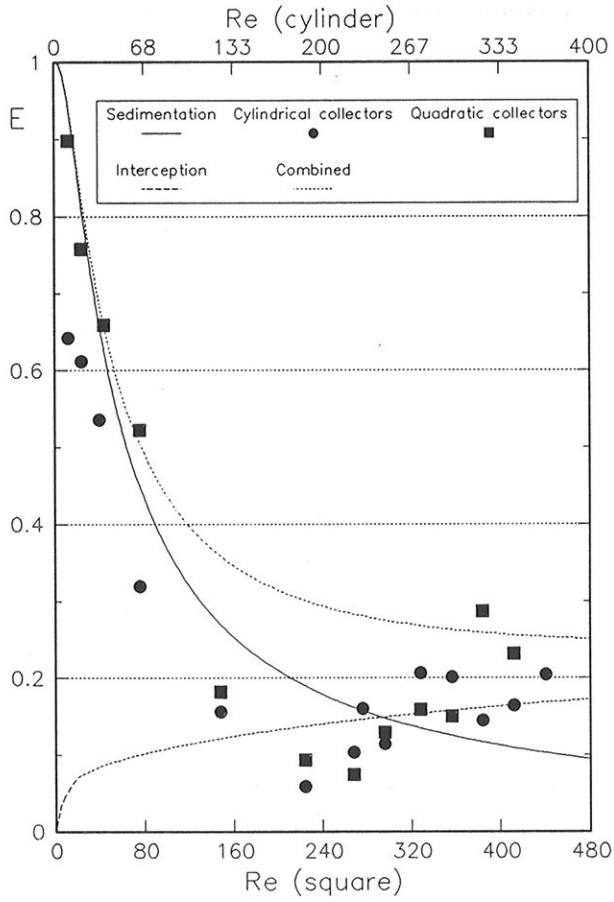

Figure 6.3 Filtration efficiency versus Reynolds number

The effects of buoyancy and direct interception on the filtration efficiency

The **collision** efficiency, η, is defined as the fraction of particles approaching the collector that will touch the collector. If an adhesion efficiency of 100% is assumed the **collection** efficiency equals the collision efficiency. Given a collection efficiency for the single collectors, the filtration efficiency, E, for the entire bed may be calculated.

In the case of the water model a simple statistical approach may be used. The probability for a particle of escaping the first collector is given by $(1-\eta_1)$ and the probability of escaping both the first and the second collector is given by $(1-\eta_1)(1-\eta_2)$ assuming statistical independence i.e. η_2 is not affected by the presence of the first collector. The probability of escaping the entire filter with 5 collectors in-line is then given by

$$(1 - E) = (1 - \eta_1)\cdot(1 - \eta_2)^4 \qquad (6.4)$$

where the same collision efficiency has been assumed for the last four collectors.

To determine the collision efficiency due to gravity or buoyancy, the velocity difference between fluid and particle, U_s, is introduced. U_s is Stoke's settling velocity

$$U_s = \frac{\Delta\rho g d^2}{18\mu} \qquad (6.5)$$

When the particles get close to a wall it will affect their settling velocity. O'Neill (1968) calculated the drag force on

a sphere in contact with a plane wall in a slow linear shear flow and got a correction factor 1.7009 in Stokes drag force. Using this correction factor the settling velocity becomes 0.035 cm/s. This is strictly valid for spherical particles only. It was observed that some of the particles had been deformed due to mechanical wear since the same particles were used in all experiments. Some of the particles had a shape rather more like a disc. Particles of this shape will have a lower settling velocity.

If the vertical projection of the collector is A_v and the projection normal to the mean particle flow direction is A then according to Engh:

$$\eta_g = \frac{A_v \cdot U_s}{A \cdot U_\infty + A_v \cdot U_s} \tag{6.6}$$

U_∞ is the velocity of the particles. The model geometry gives

$$\eta_{1,g} = \frac{U_s}{U_\infty + U_s} \tag{6.7}$$

$$\eta_{2,g} = \frac{U_s}{U_\infty/\epsilon + U_s} \tag{6.8}$$

Here ϵ is the bed porosity; $\epsilon = 0.61$ for the cylindrical collector bed and $\epsilon = 0.5$ for the bed with quadratic collectors.

To determine the collision efficiency due to direct interception we must take the boundary layer into account. In Subsection 2.2.4 we found the influence of boundary layers by calculating the ratio between the collision efficiency for boundary layer flow

and the collision efficiency due to potential flow as a function of a dimensionless parameter (of the form of a Reynolds number times a constant, i.e. depending on the velocity). This ratio is plotted on Figure 2.2 as discrete values. In order to calculate the ratio for any velocity value, a linear interpolation between the calculated discrete values is used. The filtration efficiency resulting from these calculations is given in Figure 6.2. It is zero at zero velocity and rises to approximately 0.18 at 1.2 cm/s.

In Figure 6.2 we have plotted the filtration efficiency due to the sum of the two collision efficiencies, i.e.

$$\eta_{tot} = \eta_g + \eta_i - \eta_g \cdot \eta_i$$

This way of summing the mechanisms gives a too high filtration efficiency because implicitly some particles are removed by both mechanisms, i.e. twice. Also the calculations do not take into account that there is a separation zone behind the collectors that would give rise to increased residence times, and thereby increased settling.

Discussion

It is seen from Figure 6.2 that the filtration efficiency drops with increasing velocity below 0.6 cm/s. Beyond 0.6 cm/s there is a tendency for efficiency to increase with velocity. In this higher velocity range there is a transition to unsteady flow. This was observed from colour tracer experiments. In this velocity region the interception mechanism starts to play a role. Due to the decreasing boundary layer thickness the collision efficiency increases with increasing velocity.

For the lower velocity region it is seen that the filtration efficiency is very high at low velocities. The explanation is that the particles have a very small, but still finite settling velocity. Thus at velocities of 0.1 cm/s removal is impressive in spite of our effort to employ neutrally buoyant particles. According to Netter and Conti (1986) most industrial units operate in the velocity range 0.03 - 1.00 cm/s (approach velocity). Our water model experiments indicate that in the lower half of this velocity range removal by settling will be the dominant mechanism and in the higher half removal by interception is the dominant mechanism.

From Figure 6.2 we see that there is a minimum in the measured filtration efficiency curve at approximately 0.5 cm/s. Our theory does not foresee such a minimum. The explanation seems to be that this is an effect of the symmetry of the water model. For a certain velocity range it may give rise to a situation where a number of particles that should have been removed by sedimentation miss the collectors repeatedly. Such an explanation should also give rise to a smaller minimum at higher velocities that are multiples of the first. For the cylindrical collectors a tendency for this appears at approximately 1.0 cm/s.

A rough estimate of this effect will be given here. Let the approach velocity be 0.5 cm/s. With a porosity of 0.5 the interstitial velocity is 1.0 cm/s according to Dupuit's law. If a particle is exactly between the two first collectors on the line through their centres, it will have to cover a distance of 17 cm to escape the filter. With a linear velocity of 1 cm/s this will take 17 s. The distance down to the collectors beneath is 1.0 cm. If the particle settles with a settling velocity of 0.06 cm/s (which is correct in the core-flow, but not close to the

collectors), it will settle a distance of 1.02 cm. Taking into account that the settling velocity used is somewhat high close to the collectors we see that particles may escape the water model filter due to this "symmetry" effect.

It is also observed that the square collectors give the highest filtration efficiencies at low flow velocities. This might be an effect of the sharp edges of the square collectors. They give rise to a very defined separation zone where settling will be increased. On the other hand it should be noted that the adjusted standard error is larger for the square collectors than for the cylinders (see Table III.5 and III.6).

6.3 Industrial measurements - filtration theory

In Chapter 4 the filtration efficiency for an industrial Alcoa 528 filter was found as a function of inclusion size. Melt volume flow approaching the filter were about 10 kg/s, giving melt flow velocities (inside the filter) around 2 cm/s (Re_{528} = 250). The water model studies indicate that removal should be by direct interception for this flow region.

Cast 1.2 and 2.1 were both with pure aluminium. (1-E) has been plotted as a function of inclusion size on Figure 6.4 where it is assumed that

$$1 - E = e^{-k \cdot r} \qquad (6.9)$$

k is estimated from each of the nine points different from zero. (It seems obvious that the measurement at 7 μm for cast 2.1 is an artifact (see Chapter 4).) From this we have calculated the mean of the constant k and its standard deviation

$$k = 0.56 \pm 0.22$$

Figure 6.4 shows exp(-kr), exp(-(k+s)r), and exp(-(k-s)r). It seems that Eq. (6.9) fits the experimental points.

In Chapter 2 we found that removal by direct interception (Eq. (2.24) with (2.30), (2.31), and (2.32) inserted) is given by

$$1 - E = e^{-\frac{9\cdot(1-\epsilon)\cdot s\cdot r}{\epsilon\cdot d_c^2}} = e^{-0.56\cdot r} \qquad (6.10)$$

where r is the inclusion radius (given in μm), d_c = 4 mm is the collector diameter, ϵ = 0.5 is the porosity, and s = 1 m is the length of the path through the filter. It is seen that the correspondence between experimental data and theory happens to be good.

For the Al-Mg-alloy, no relationship between (1-E) and r is evident (Figure 6.5). On the other hand , in this case it looks like the filtration efficiency is independent of inclusion size. Calculating a mean filtration efficiency; we get $\overline{E}$ = 0.99 for cast 3.1 and $\overline{E}$ = 0.84 for cast 4.1. An explanation for this could be the presence of salt. Salt droplets might have a large influence on the effective size of small inclusions. This will lead to a higher collision efficiency since:

$$\eta = \frac{3(r+\Delta r)}{d_c/2}$$

where r is the inclusion radius and Δr is the increase due to the salt. The effect, Δr, will depend on r and will be smaller for larger inclusions. The result could be that the filtration efficiency seems to be independent of inclusion size.

Chronologically cast 4.1 is after cast 3.1, but the filtration efficiency is lower. This could indicate filter releases, but data is too scarce to say anything definite.

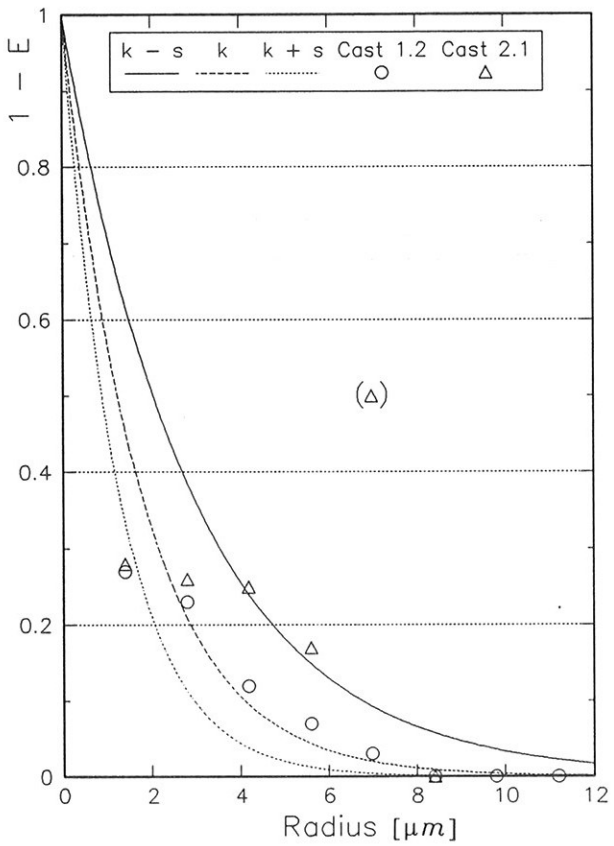

Figure 6.4 (1-E) for pure aluminium as a function of inclusion radius in μm.

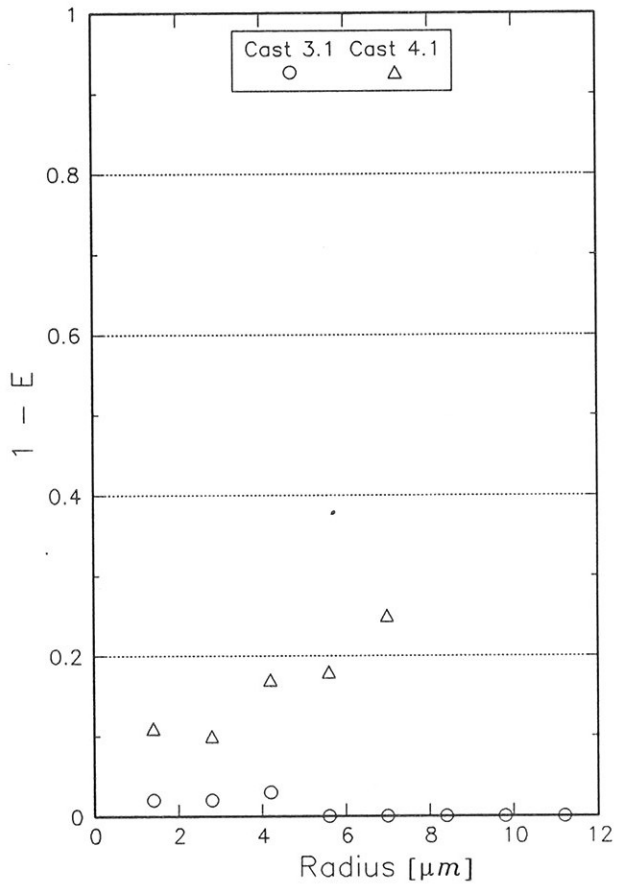

Figure 6.5 (1-E) for Al-Mg-alloy as a function of inclusion radius in μm.

6.4 Number size distribution

In Chapter 4 we saw that the number size distribution of aluminium carbides was exponential within the size range studied. This was true for distributions at different depths inside the sampling filters as well as for the total number size distributions.

If we assume spherical carbide inclusions with radius r, that an inclusion contains ρ_c carbide moles per unit volume and that the mass transfer coefficient for carbide is k_c, then Engh (Section 5.6) has found

$$\frac{df_N(r)}{f_N(r)} = -\frac{dr \cdot k_t \cdot A \cdot \rho_c \cdot 12 \cdot 100}{k_c \cdot \rho_m \cdot \Delta[\%C] \cdot V} \tag{6.11}$$

Here $\Delta[\%C]$ is the driving force for diffusion of carbon. V is volume of melt and ρ_m the density. $f_N(r) \cdot \Delta r$ is the number of inclusions per unit volume in the size interval r to r + Δr. k_t is the mass transfer coefficient for removal of an inclusion of size r. A is the contact area between melt and refractories and top slag.

If $\frac{k_t}{k_c}$ does not depend on r, integration gives

$$\frac{f_N(r)}{f_N(r_c)} = e^{-(r-r_c)\frac{k_t \cdot A \cdot \rho_c \cdot 12 \cdot 100}{k_c \cdot \rho_m \cdot \Delta[\%C] \cdot V}} \tag{6.12}$$

where $f_N(r_c)$ is the number of particles of size r_c. It is seen that this number size distribution of the inclusions is decreasing exponential.

In Section 6.3 we found that k_t (inside the filter) was proportional to r. According to Engh (Chapter 7) k_c may be independent of r. This will give $\frac{k_t}{k_c}$ depending on r. Then the number size distributions should also become steeper with increasing depth in the sampling filters since larger inclusions would be removed more efficiently. It is not possible to draw this conclusion based on our measurements. A possible explanation for this discrepancy is that there is re-entrainment of the larger inclusions.

7 CONCLUSIONS

Filtration mechanisms

A filtration theory has been proposed that takes into account the 3-dimensional nature of the filter. The theory is a development of previous theories.

From water model studies it has been found that removal of "neutrally" buoyant particles is controlled by sedimentation at approach velocities less than 0.6 cm/s. Theoretical curves lie above the measurements. Removal at velocities above 0.6 cm/s is controlled by direct interception. When taking the boundary layer into account, theory and measurements fit well. In an intermediate region the measurements lie below the theory due to symmetry effects in the water model.

Filtration efficiencies from industrial measurements may be explained by removal by direct interception. This conclusion is supported by the water model studies since the Reynolds number for the industrial measurements is 250, i.e. in the range where direct interception was found to be the dominating mechanism in the water model.

Industrial measurements

The number size distribution of inclusions can be determined metallographically from sampling filters employing image analysis. For the melts studied this distribution was found to be a decreasing exponential function of size (in the size-range studied).

For an Alcoa 528 filter the filtration efficiency as a function of particle size has been determined. As expected the efficiency increases with inclusion (Al_4C_3) size. The filtration efficiency obtained may be explained by removal of particles by interception with the filter grains.

Surface tension model

A theoretical model for the effect of dissolved elements on the surface tension and interfacial tension has been developed and calibrated against measurements found in the literature. With knowledge about three fundamental handbook quantities the effect of metallic elements on the surface tension of aluminium and interfacial tension between aluminium and alumina is determined. These quantities are metallic radius, electronegativity, and the surface tension of the pure added element.

Adhesion

It is felt that understanding the adhesion and the phenomena leading to adhesion between particle and filter immersed in melt is the key to a proper understanding of the problem of re-entrainment and filter long term behaviour.

8 INDUSTRIAL APPLICATIONS

There seems to be three possible ways to remove inclusions at high filtration efficiencies:

1. Use low melt velocities. This ensures a high removal by sedimentation and low probability of re-entrainment. The method is costly in terms of treatment time.

2. Assuming that no re-entrainment could be ensured, it would be possible to filter at high melt velocities, for example by using a rotor. This method would utilize the interception mechanism, i.e. a filtration efficiency E_1. But by recirculating the melt through the filter several times or by using several units in series, a very good efficiency could be obtained. If the melt were recirculated n times or sent through n units in series the filtration efficiency would be

$$E = 1 - (1 - E_1)^n$$

3. The sedimentation rate may possibly be increased by using electromagnetic fields. Higher flow velocities could then be used.

An efficient, but not always feasible method to ensure good removal is to increase the depth of the filter. A long residence time in the filter combined with good adhesion will always give high efficiency.

The most important remaining questions to be answered are:

a) How are inclusions re-entrained?

b) What effect do the inclusions have on the pressure drop?

c) How do a) and b) change with time (amount of metal filtered)?

With respect to choice of filter material it would seem that the melt and filter should not wet each other. Therefore there must be a third phase present, for instance gas, salt, or vacuum acting as a "glue". According to Luk et al. (1987) if liquid and filter do not wet there is a 33% reduction in pressure drop at low velocities.

REFERENCES

Adamson, A.W. (1982), "Physical chemistry of surfaces", John Wiley & Sons, Inc., 4th edition

Ali, S., D. Apelian, and R. Mutharasan (1985), "Refining of aluminium and steel melts by the use of multicellular extruded ceramic filters", Can. Met. Q. **24** (4), 311-318

Apelian, D. and R. Mutharasan (1980), "Filtration: A melt refining method" **32**, 14-19

Apelian, D., R. Mutharasan, C.A. Romanowski, R.E. Miller, and C.E. Eckert (1982), "Commercially available porous media for molten metal treatment: a property evaluation", Light Metals 1982, 935-968

Apelian, D., R. Mutharasan, and S. Ali (1985), "Removal of inclusions from steel melts by filtration", J. Mater. Sci. **20**, 3501-3514

Apelian, D., S. Luk, T. Piccone, and R. Mutharasan (1986), "Removal of liquid and solid inclusions from steel melts", Proc. Steelmaking Conf. 69 (Int. Iron Steel Congr. 5th, 1986, Bk), Book 1, 957-67

Aylward, G.H. and T.J.V Findlay (1978), "SI chemical data", John Wiley & Sons, Inc., 2nd edition

Bargalik, J. and Cz. Sajdak (1985), "Purification of liquid aluminium from non-metallic inclusions in the electromagnetic-field", Elektrowärme International **43**(B 2), B77-B80

Bathen, E. (1985a), "Investigation of inclusions in aluminium melts by image analysis", Paper presented at the International Seminar on Refining and Alloying of Liquid Aluminium and Ferro-Alloys, August 26-28, Trondheim, Norway, 174-191

Bathen, E. (1985b), "Investigation of inclusions in aluminium by image analysis/light microscopy on sampling filters", Report STF34 A85136 , SINTEF, Trondheim, Norway (In Norwegian)

Bathen, E. and T.A. Engh (1988), "Deposition of inclusions down through a sandwich type foam filter studied by automatic image analysis", Light Metals 1988, 423-430

Belton, G.R. (1976), "Langmuir adsorption, the Gibbs adsorption, and interfacial kinetics in liquid metal systems", MET. TRANS. B **7B**, 35

Bird, R.B., W.E. Stewart, and E.N. Lightfoot (1960), "Transport phenomena", John Wiley & Sons, Inc., New York

Blayden, L.C. and K.J. Brondyke (1974), "Alcoa 469 process", Journal of Metals, February 1974

Bondi, A. (1953), "Spreading of liquid metals on solid surfaces; Surface chemistry of high energy substances", Chem. Rev. **52** (2), 417-458

Bornand, J.-D. and K. Buxmann (1985), "DUFI: a concept of metal filtration", Light Metals 1985, 1249-1260

Bowden, F.P. and D. Tabor (1950), "The friction and lubrication of solids", Clarendon Press, Oxford, 307

Bowden, F.P. and J.E. Young (1951), "Friction of clean metals and the influence of adsorbed films", Proc. Roy. Soc. **A208**, 311

Brant, M.V., D.C. Bone, and E.F. Emley (1971), "Fumeless in-line degassing and cleaning of liquid aluminium", J. Metals, **23** (3), 48-53

Brennan, J.J., and J.A. Pask (1968), "Effect of nature of surfaces on wetting of sapphire by liquid aluminium", J. Amer. Ceram. Soc. **51** (10), 569-573

Bruce, R.H. (1965), "Science of ceramics", vol. 2, Edited by G.H. Stewart, Academic Press Inc., (London)

Buzagh, A. (1930), "Uber die haftfahigkeit mikroscopischer teilchen an wanden von gleicher beschaffenheit", Kolloidchem. Beih., **51**, 105

Buzagh, A. (1931), "Uber die haftfahigkeit und raumerfullung mikroscopischer teilchen", Kolloidchem. Beih., **32**, 114

Campbell, I.E. and E.M. Sherwood (1967), "High-Temperature Materials and Technology", John Wiley & Sons, Inc, New York, 272

Carnahan, R.D., L.T. Johnson, and C.H. Li (1958), "Some observations on the wetting of Al_2O_3 by aluminium", J. Am. Ceram. Soc. **41** (9), 343-347

Champion, J.A., B.J. Keene, and J.M. Sillwood (1969), "Wetting of aluminium oxide by molten aluminium and other metals", J. Mater. Sci. **4**, 39-49

Conti, C. (1983), "Contribution à lètude de la filtration profonde des métaux", Thèse de Doctorat, Faculté de Polytechnique de Mons, Belgique (In French)

Conti, C. and M. Jacob (1984), "Depth filtration of liquid metals: application of the limiting trajectory method to the calculation of inclusion deposition in open cell structure filters", Bulletin de la Société Chimique de France, no. 11-12, I297-I313

Cook, T.L. and F.H. Harlow (1986), "Vortices in bubbly two-phase flow", Int. J. Multiphase Flow **12** (1), 35-61

Corn, M. (1961), "The adhesion of solid particles to solid surfaces, I. A review", Journal of the Air Pollution Control Association, **11**(11), 523-528

Dawihl, W. and J. Federmann (1974a), Aluminium **50**, 574

Dawihl, W. and J. Federmann (1974b), Fachberichte der Tagung Verbundswerkstoffe, Konstanz, 450-468

Defay, R. and I. Prigogine, with the collaberation of A. Bellemans, translated from the French by D.H. Everett: "Surface tension and adsorption", 1966, Longmans, Green & Co Ltd., London

Delanney, F., L. Froyen, and A. Deruyttere (1987), "Review: The wetting of solids by molten metals and its relation to the preparation of metal-matrix composites", Journal of Materials Science **22**, 1-16

Eady, J.A., D.M. Smith, and J.F. Grandfield (1986), "Filtration of aluminium melts", Paper presented at Aluminium Technology '86, The Institute of Metals, London, 93-100

Eckert, C.E., R.E. Miller, D. Apelian, and R. Mutharasan (1984), "Molten aluminium filtration: fundamentals and models", Light Metals 1984, 1281-1304

Engh, T.A. "Principles of metal refining", Oxford University Press, Oxford, To be published

Engh, T.A. et al. (1972), "Si-deoxidation of steel by injection of slags with low SiO_2 activity", Scand. J. Metall. **1**, 103-114

Engh, T.A., B. Rasch, and E. Bathen (1986), "Deep bed filtration theory compared with experiments", Light Metals 1986, ed. R.E. Miller, TMS-AIME, 829-836

Eustathopoulos, E., J.C. Joud, P. Desré, and J.M. Hicter (1974), "The wetting of carbon by aluminium and aluminium alloys", J. Mater. Sci. **9**, 1233-1242

Farias, L.R. and D.G.C. Robertson (1982), "Physical modelling of gas-powder injection into liquid metals", Proceedings of 3rd Process Technology Conference, Pittsburgh, Mar 28-31, ISS of AIME, 206-220

Gauckler, L.J., M.M. Waeber, C. Conti, and M. Jacob-Dulière (1985), "Industrial application of open pore ceramic foam for molten metal filtration", Light Metals 1985, 1261-1283

Grandfield, J.F. (1989), "Sources of inclusions and defect they generate", Aluminium Melt Refining and Alloying - Theory and Practice, Melbourne, July 10-12, 1989, K-1 - K-6

Grjotheim, K., C. Krohn, M. Malinovský, K. Matiasovský, and J. Thonstad (1982), "Aluminium Electrolysis - Fundamentals of the Hall-Héroult Process", Aluminium-Verlag, Düsseldorf, Germany, 2nd edition, ISBN 3-87017-155-3

Groteke, D.E. (1983), "The reduction of inclusions in aluminium by filtration", Mod. Cast. **73** (4), 25-27

Gruesbeck, C. and R.E. Collins (1982), "Entrainment and deposition of fine particles in porous media", Soc. Petr. Eng. J., 847-856

Goumiri, L., J.C. Joud, and P. Desré (1979), Surf. Sci. **83**, 471

Goumiri, L. and J.C. Joud (1982), "Auger electron spectroscopy study of aluminium-tin liquid system", Acta metall. **30**, 1397-1405

Herzig, J.P., D.M. Leclerc, and P. le Goff (1970), "Flow of suspensions through porous media - application to deep filtration", Ind. and Eng. Chem. **62** (5), 8-35

Hicter, JM. H. (1983), "AlPur refining process", Light Metals 1983, 1005-1022

Iida, T. and R.I.L. Guthrie (1988), "The physical properties of liquid metals", Oxford University Press, Oxford

Johansen, S.T. and N.M. Anderson (1990), "A mathematical model for large scale filtration of aluminium", Paper presented at the 119th AIME Annual Meeting, Anaheim, California, February 19-22

John, H. and H. Hausner (1986), "Influence of oxygen partial pressure on the wetting behaviour in the system Al/Al_2O_3", J. Mater. Sci. **5**, 549-551

Kingery, W.D. (1960), "Introduction to ceramics", John Wiley & Sons, Inc., New York, 194

Korolkow, A.M. (1956), Izw. A. N., OTN. 2, 75

Korolkow, A.M. and A. Bytschkowa (1960), Issled. Splaw. Tswetn. Met. 2, 122

Korolkow, A.M. and A.A. Igumnowa (1961), Izw. A. N., OTN. 6, 95

Köhler, W. (1975), "Untersuchungen zur Benetzung von Al_2O_3- und SiC-Kristallen durch Aluminium und Aluminiumlegierungen", Aluminium **51** (7), 443-447 (In German)

Köhler, W., E. Van Rensen, and K. Sahm (1973), BMFT-Fortschungsbericht T73-14

Körber, K. and K. Löhberg (1971), Gießeriforschung **23**, 173

Lang, G. (1973), "Gießeigenschaften und Oberflächenspannung von Aluminium und binären Aluminiumlegierungen", Aluminium **49** (3), 231-238 (In German)

Lang, G. (1974), "Einfluß von Zusatzelementen auf die Oberflächenspannung von flüssigem Reinstaluminium", Aluminium **50** (11), 731-734 (In German)

Lang, G., P. Laty, J.C. Joud, and P. Desré (1977), "Messung der Oberflächenspannung einiger flüssiger Reinmetalle mit verschiedenen Methoden", Z. Metallk. **67**, 113-116 (In German)

Lijun, Z., W. Jinbo, Q. Jiting, N. Qiu, and Q. Peixiang (1990), "An investigation on wetting behaviour and interfacial reactions of aluminium - α-alumina system", Proceedings of the international conference on interfaces in metal-ceramics composites, TMS Annual Meeting, February 18-22, Anaheim, California

Livey, D.T. and P. Murray (1955), "The wetting properties of solid oxides and carbides by liquid metals", Plansee Proceedings, 2nd Seminar Reutte/Tirol, 375-404

Luk, S., R. Mutharasan, and D. Apelian (1987), "Experimental observations of wall slip: Tube and packed bed flow", Ind. Eng. Chem. Res. **26** (8), 1609-1616

Lupis, C.H.P. (1983), "Chemical thermodynamics of materials", North-Holland, New York, NY

Martin, J.-P. et al. (1988), "Settling phenomena in casting furnaces: a fundamental and experimental investigation", Light Metals 1988, 445-455

McLean, M. and E.D. Hondros (1971), "Grain-boundary grooving at the platinum/alumina interface", J. Mater. Sci. **6** (1), 19-24

Mehrotra, S.P. and A.C.D. Chaklader (1985), "Interfacial phenomena between molten metals and sapphire substrate", MET. TRANS. B **16B**, 567-575

Mutharasan, R., D. Apelian, and C. Romanowski (1981), "A laboratory investigation of aluminium filtration through deep-bed and ceramic open-pore filters", J. Metals, 12-17

Naidich, Yu.V., W.N. Eremenko, and L.F. Kiritschenko (1962), Sh. Neorg. Chim. 7, 333

Naidich, Yu.V. (1968), "Interfacial surface energies and contact angles of wetting of solids by liquid in equilibrium and non-equilibrium systems", Russsian Journal of Physical Chemistry **42** (8), 1023-1026

Naidich, Yu.V. (1981), "The wettability of solids by liquid metals", Progress in Surface and Membrane science, vol. 14, Edited by D.A. Cadenhead and J.F. Danielli, Academic Press, ISBN 0-12-571814-4, 353-484

Neff, D.V. and E.P. Stankiewicz (1986), "The Multicast filtration system", Light Metals 1986, 821-828

Netter, P. and C. Conti (1986), "Efficiency of industrial filters for molten metal treatment evaluation of filtration process model", Light Metals 1986 vol. 2, 847-860

N.N. (1988), "Molten metal filtration improves casting quality and machinability", FOUNDRY management & technology **116** (10), 44

O'Neill, M.E. (1968), "A sphere in contact with a plane wall in a slow linear shear flow", Chem. Engng. Sci. **23**, 1293-1298

Osawa, Y. and K. Mori (1983), "Bubbling-jetting phenomena in powder injection into liquid", Trans. ISIJ **23**, 671-675

Payatakes,A.C., C. Tien, and R.M. Turian (1973), A.I.Ch.E. Journal **1**, 58-67

Payatakes,A.C., C. Tien, and R.M. Turian (1974), "Trajectory calculation of particle deposition in deep bed filtration", A.I.Ch.E. Journal **9**, 889-905

Ranz, W.E. (1952), Chem. Eng. Prog. **48**, 247-253

Rasch, B. (1987), "Removal of inclusions from molten aluminium using gas purging and filtration", Dr.ing-thesis, The Norwegian Institute of Technology, Trondheim, Norway (In Norwegian)

Rasmussen, J.J. and R.P. Nelson (1971), "Surface tension and density of molten Al_2O_3", J. Amer. Ceram. Soc. **54** (8), 398-401

Rhee, S.K. (1970), "Wetting of ceramics by liquid aluminium", J. Am. Ceram. Soc. **53** (7), 386-389

Rhee, S.K. (1972), "Critical surface energies of Al_2O_3 and graphite", J. Am. Ceram. Soc. **55** (6), 300-303

Schlicting, H. (1968), "Boundary layer theory", Sixth Edition, McGraw-Hill Book Company, New York

Sebo, P., J. Ivan, L. Taborsky, and A. Havalada (1973), Kovore Mater. **2** (XI), 173

Simensen, C.J. and U. Hartvedt (1985), "Analysis of oxides in aluminium by means of melt filtration", Z. Metallkde, Bd. 76 H.6, 409-414

Szekeley, A.G., et al. (1976), "The removal of solid particles from molten aluminium in the spinning nozzle flotation process", MET TRANS B **78**, 259

van den Tempel, M. (1972), "Interaction forces between condensed bodies in contact", Advan. Colloid Interface Sci. **3**, 137-159

Wieser, P.F. (1984), "Filtration of liquid steel", TMS paper no. F84-4, 1984 AIME Meeting, Detroit, 1-18

Wolf, S.M., A.P. Levitt, and J. Brown (1966), "Whisker-metal matrix bonding", Chem. Engng. Prog. **62** (3), 74-78

Yatsenko, S.P., W.I. Kononenko and A.L. Schukman (1972), Tepl. Vysok. Temp. **10**, 66

APPENDIX A

Surface tension

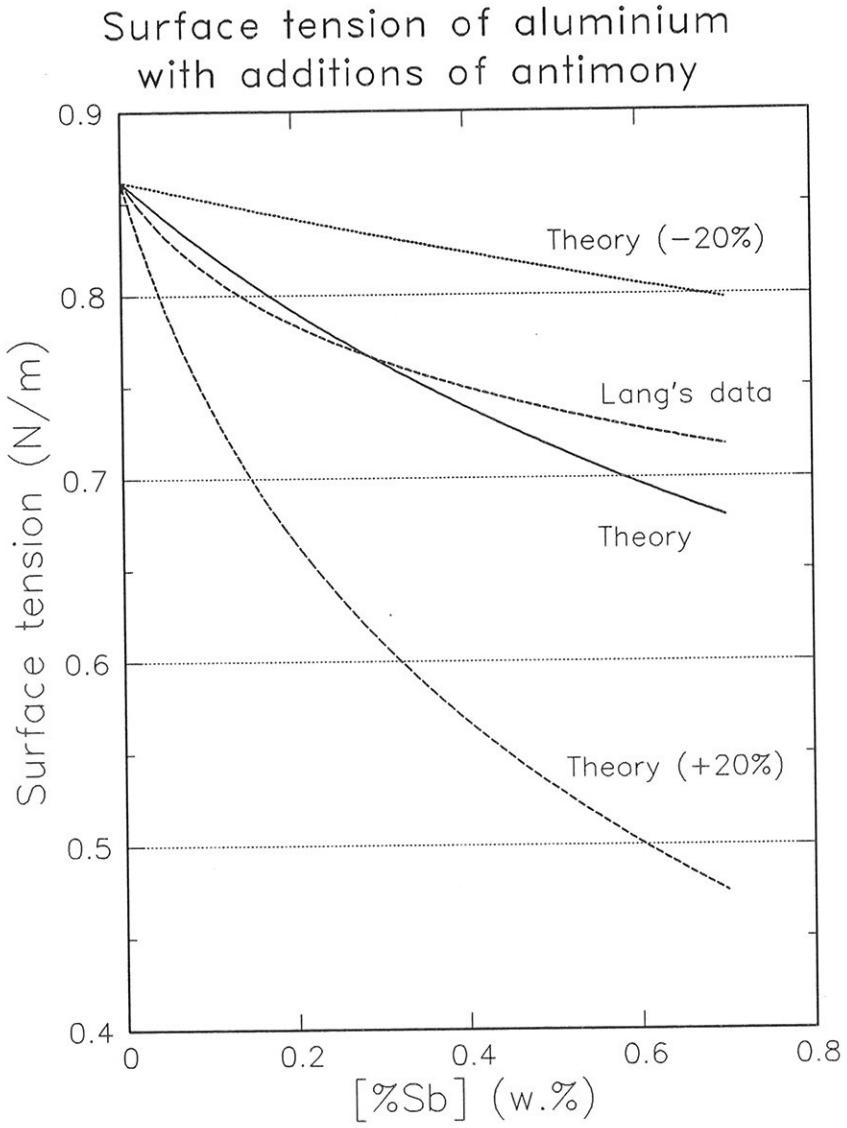

Figure A.1 Surface tension of aluminium with antimony additions. Curves for free energy of adsorption 20 % too high and too low are shown.

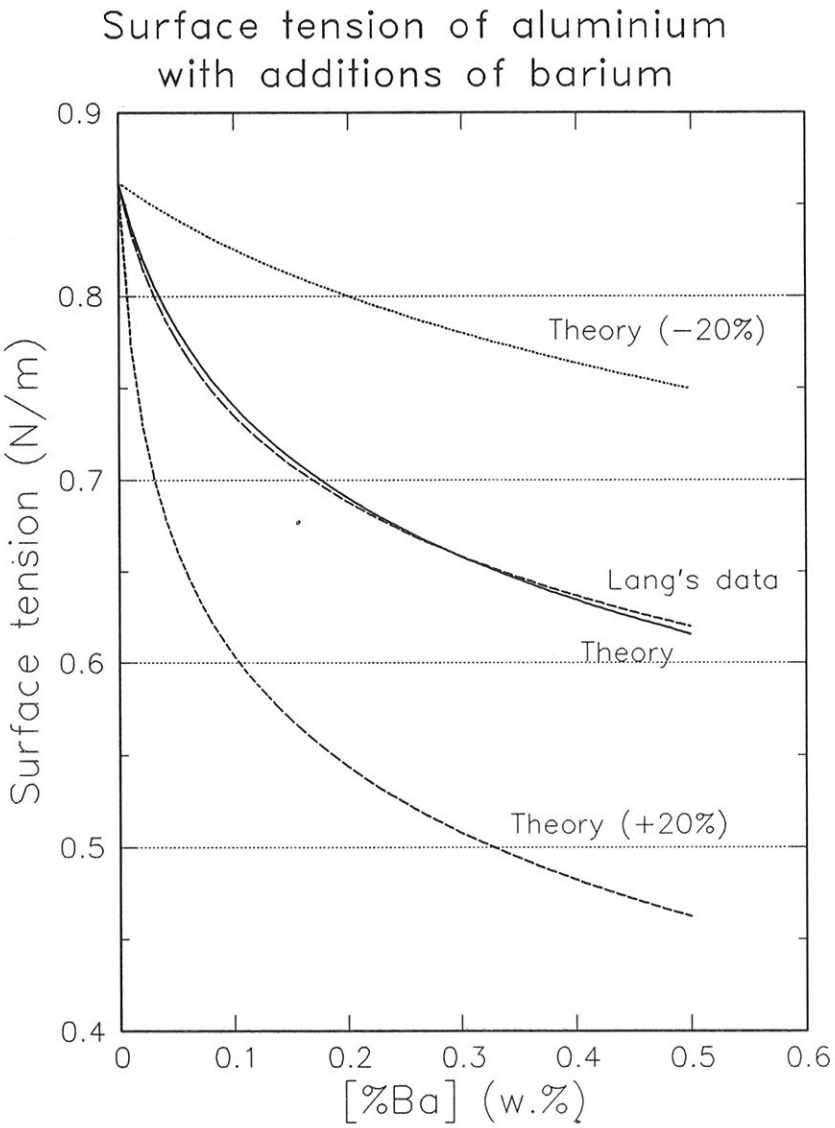

Figure A.2 Surface tension of aluminium with barium additions. Curves for free energy of adsorption 20 % too high and too low are shown.

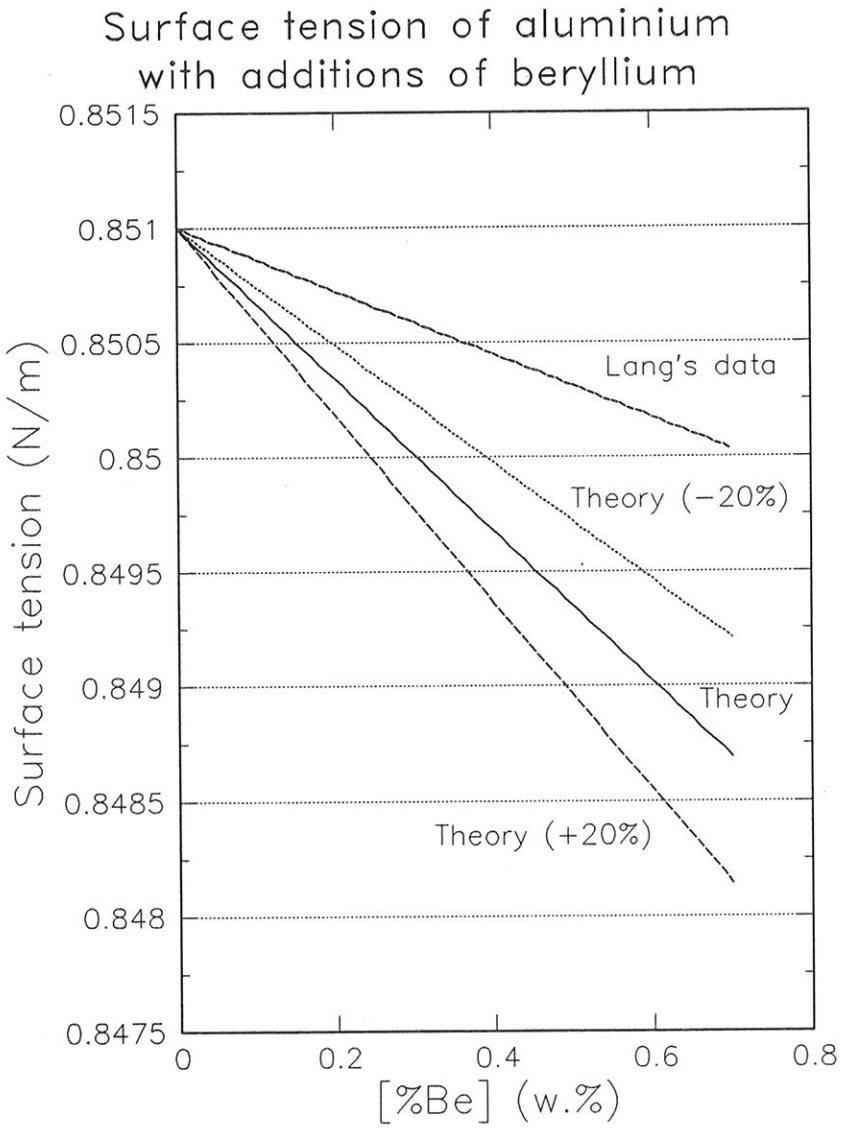

Figure A.3 Surface tension of aluminium with beryllium additions. Curves for free energy of adsorption 20 % too high and too low are shown.

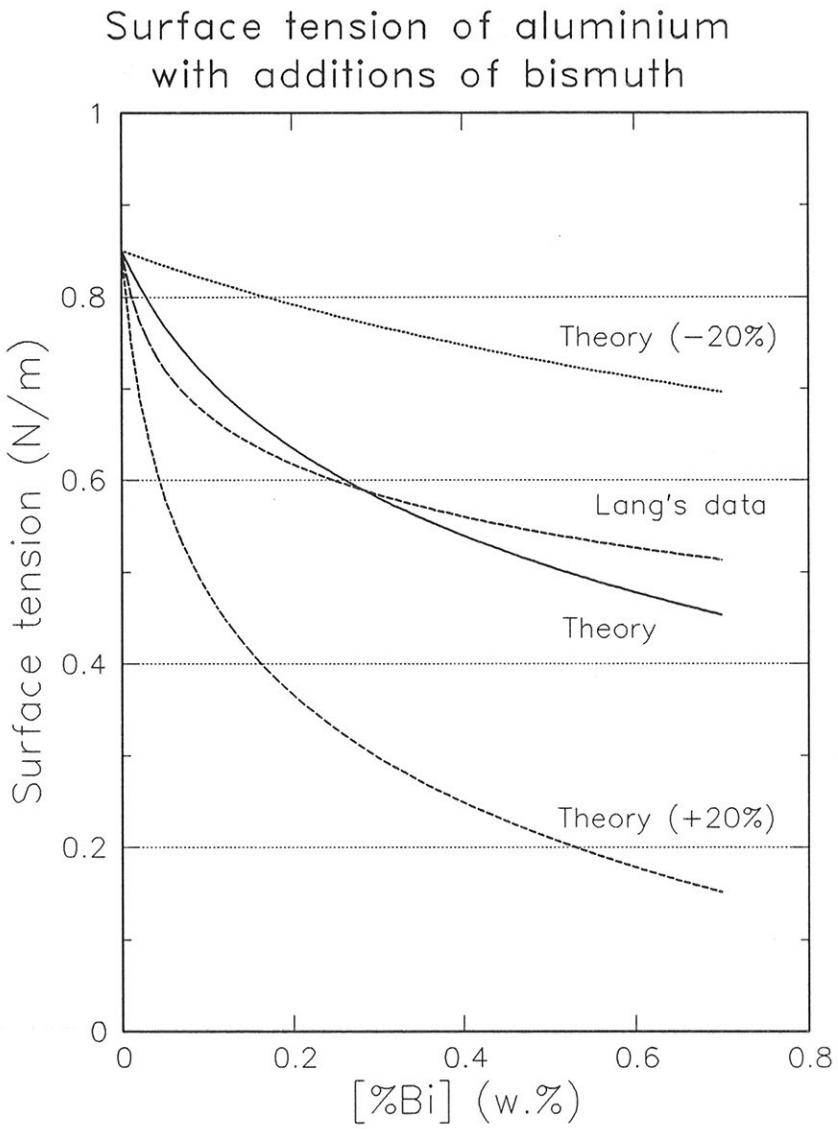

Figure A.4 Surface tension of aluminium with bismuth additions. Curves for free energy of adsorption 20 % too high and too low are shown.

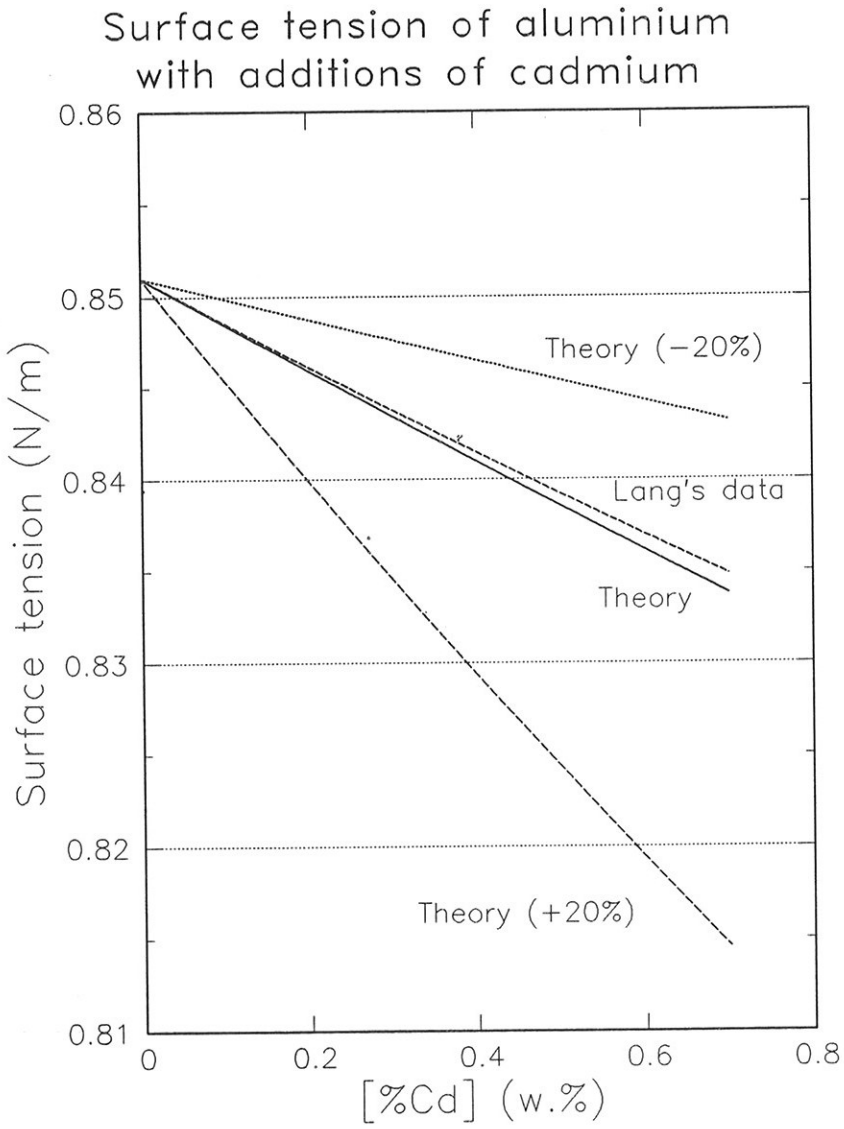

Figure A.5 Surface tension of aluminium with cadmium additions. Curves for free energy of adsorption 20 % too high and too low are shown.

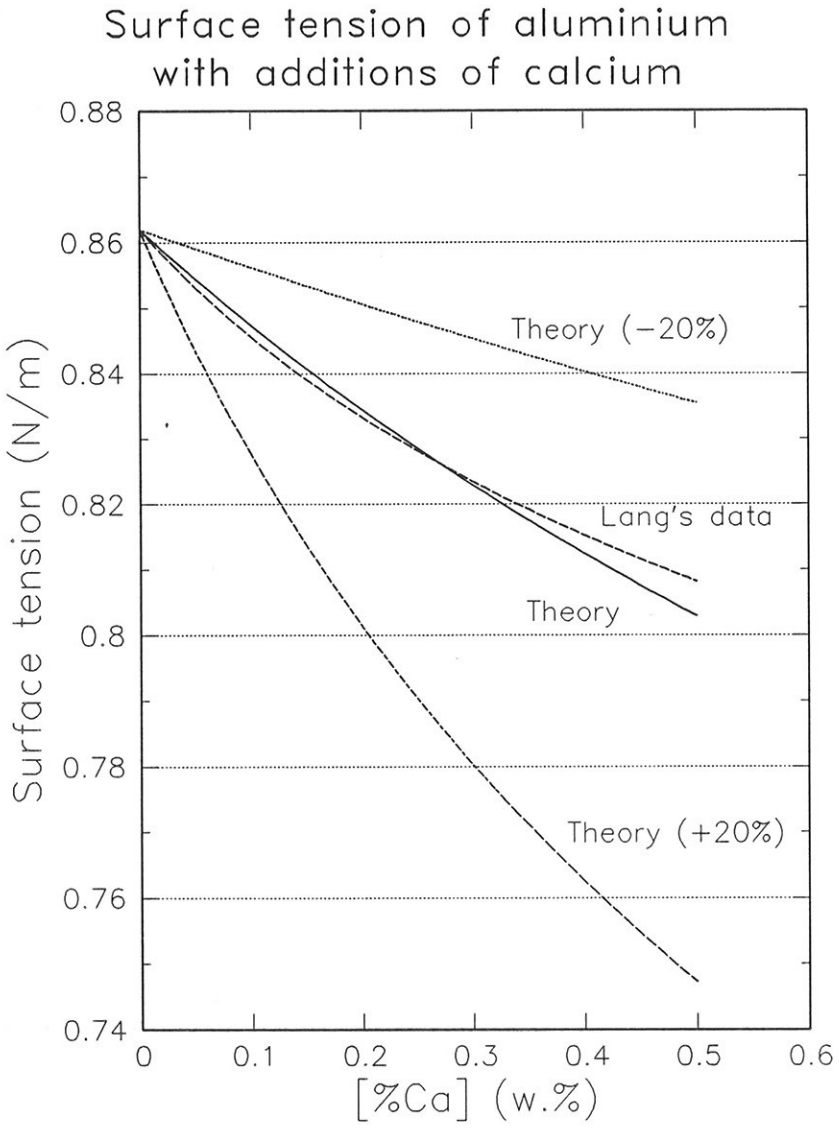

Figure A.6 Surface tension of aluminium with calcium additions. Curves for free energy of adsorption 20 % too high and too low are shown.

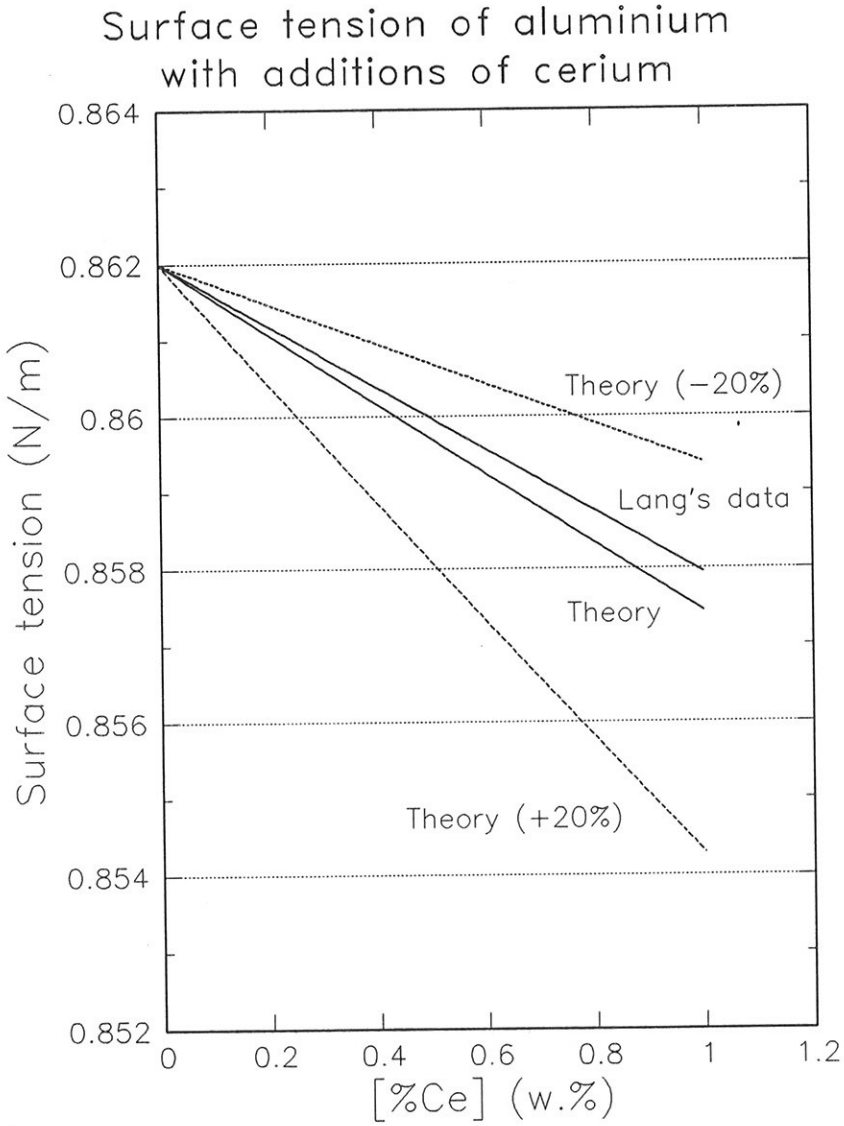

Figure A.7 Surface tension of aluminium with cerium additions. Curves for free energy of adsorption 20 % too high and too low are shown.

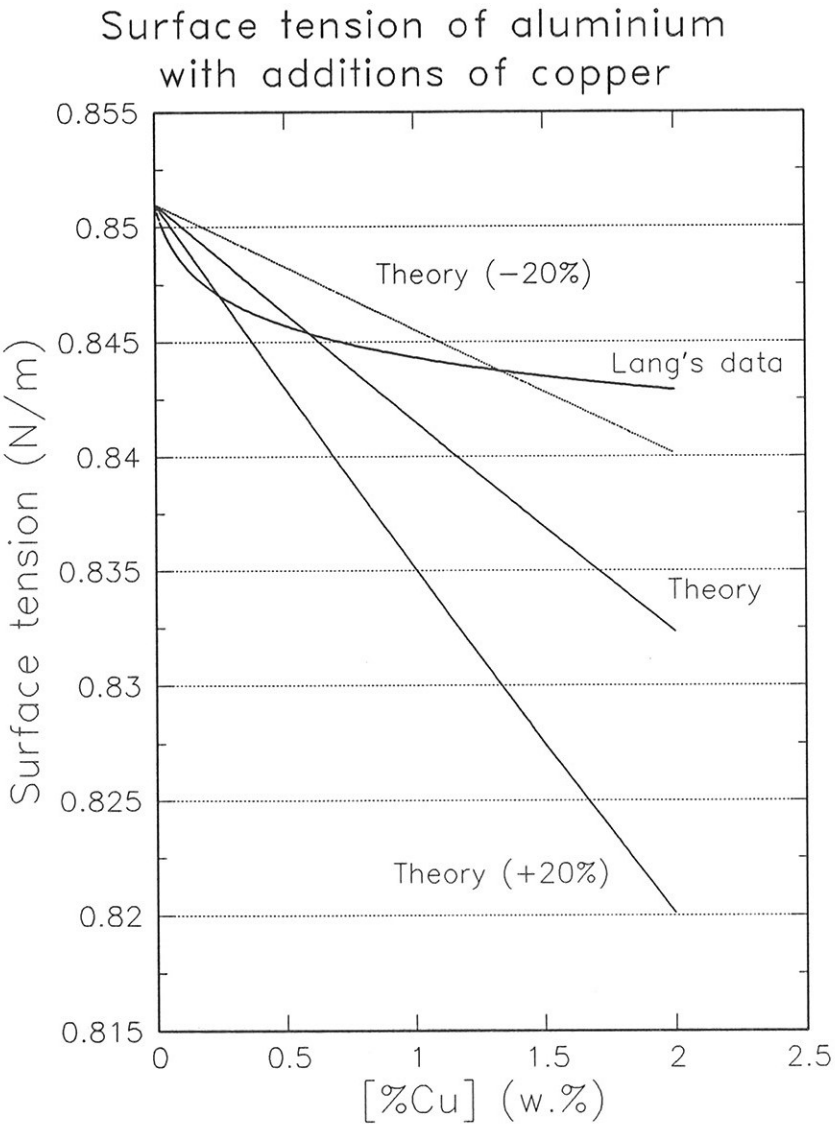

Figure A.8 Surface tension of aluminium with copper additions. Curves for free energy of adsorption 20 % too high and too low are shown.

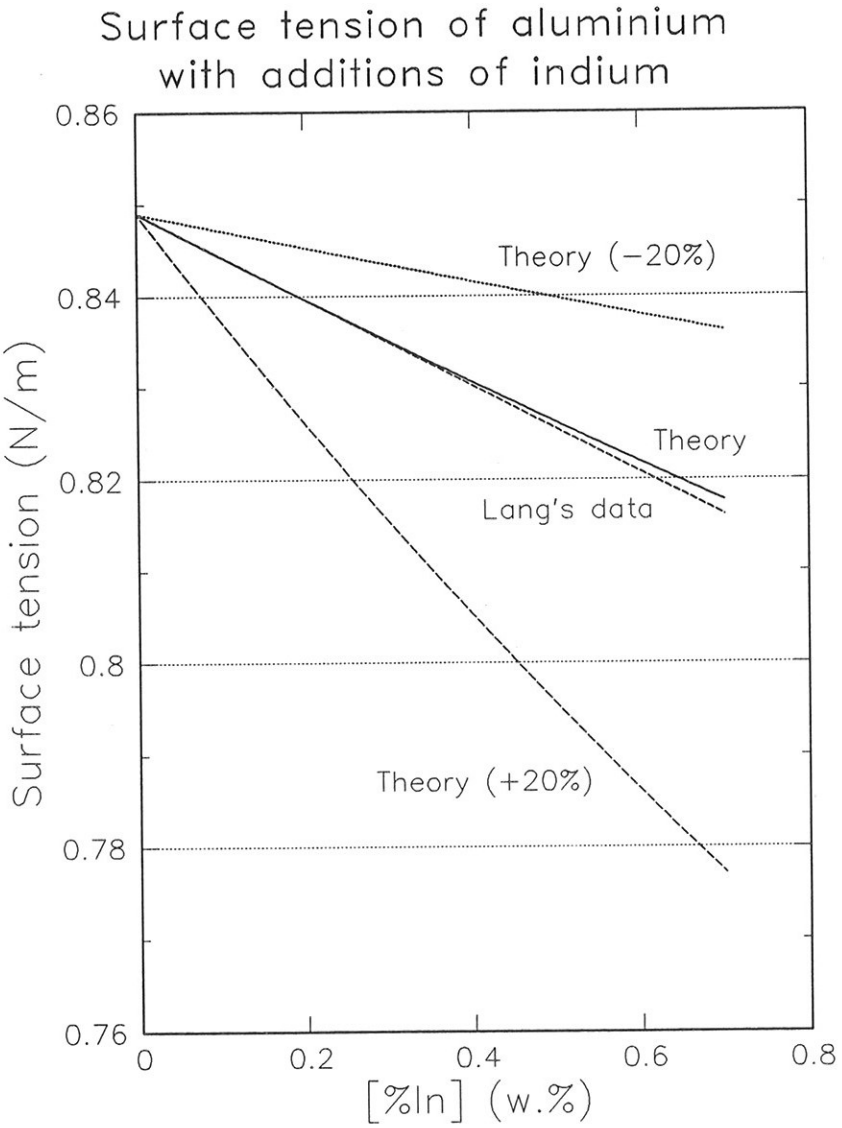

Figure A.9 Surface tension of aluminium with indium additions. Curves for free energy of adsorption 20 % too high and too low are shown.

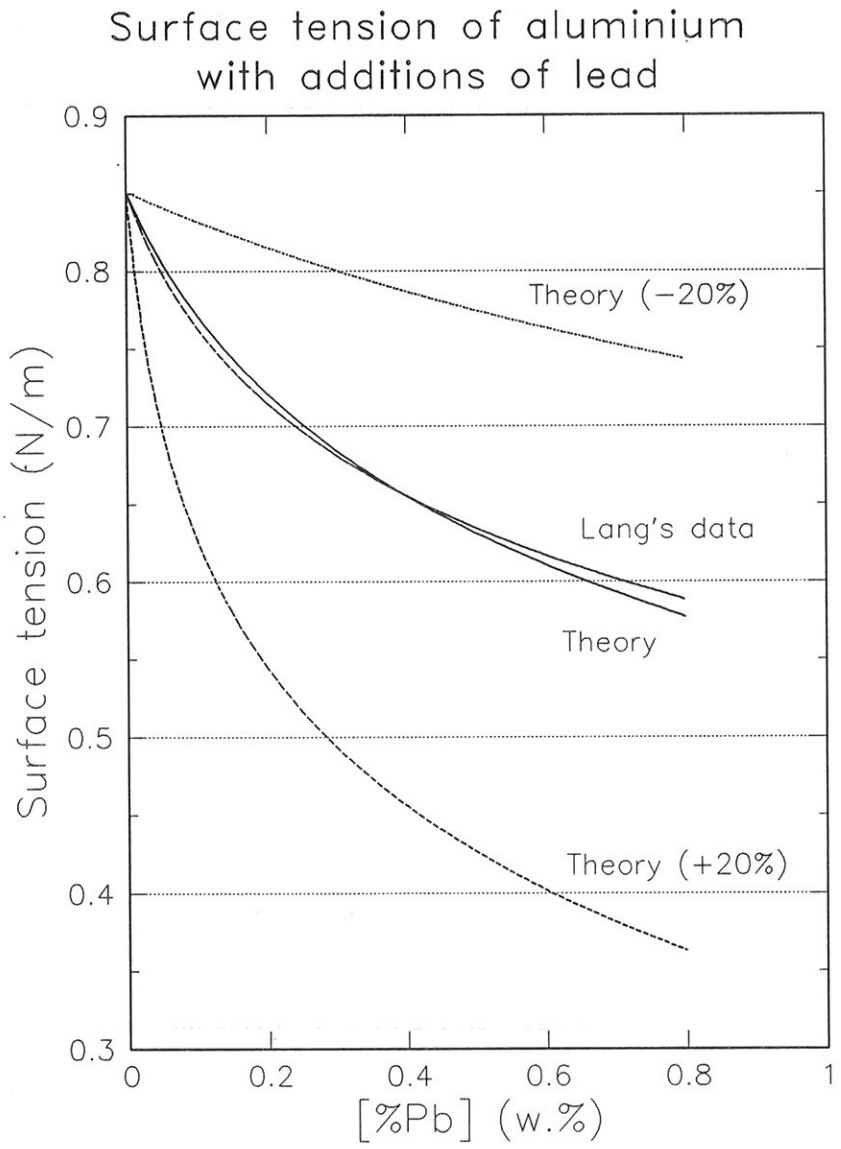

Figure A.10 Surface tension of aluminium with lead additions. Curves for free energy of adsorption 20 % too high and too low are shown.

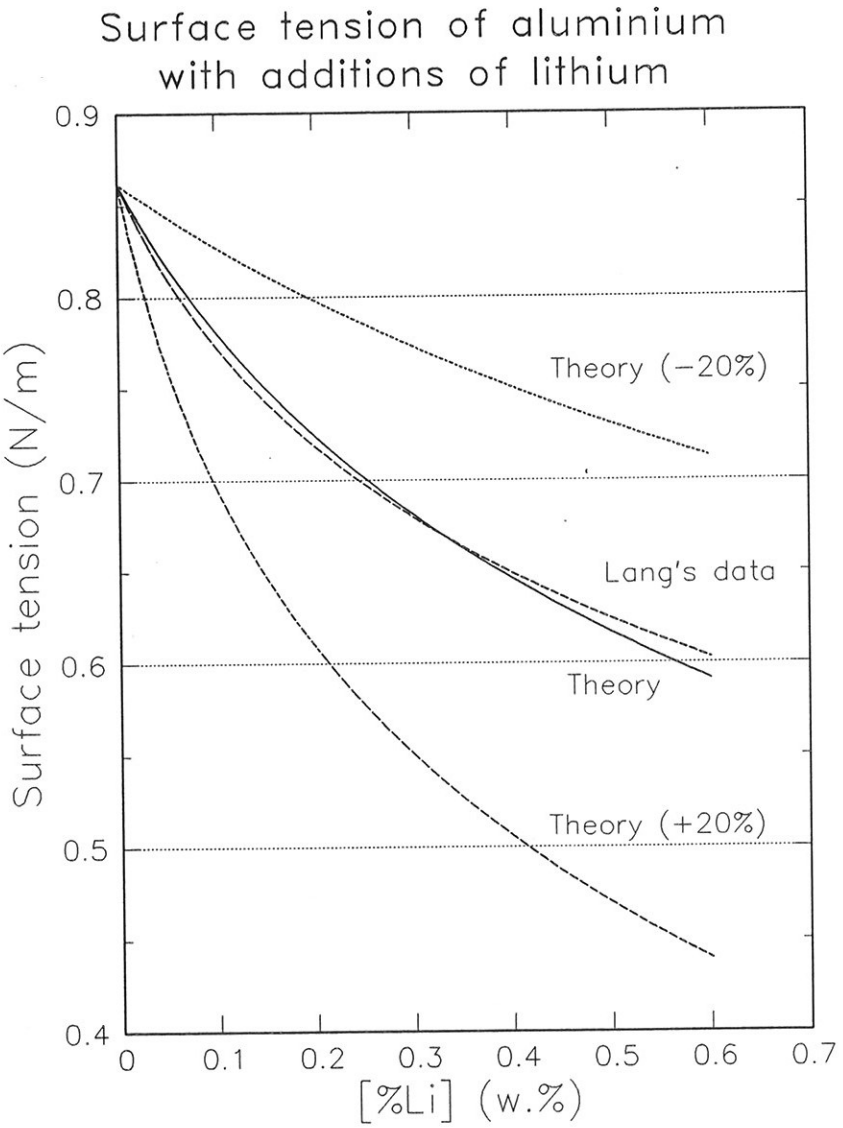

Figure A.11 Surface tension of aluminium with lithium additions. Curves for free energy of adsorption 20 % too high and too low are shown.

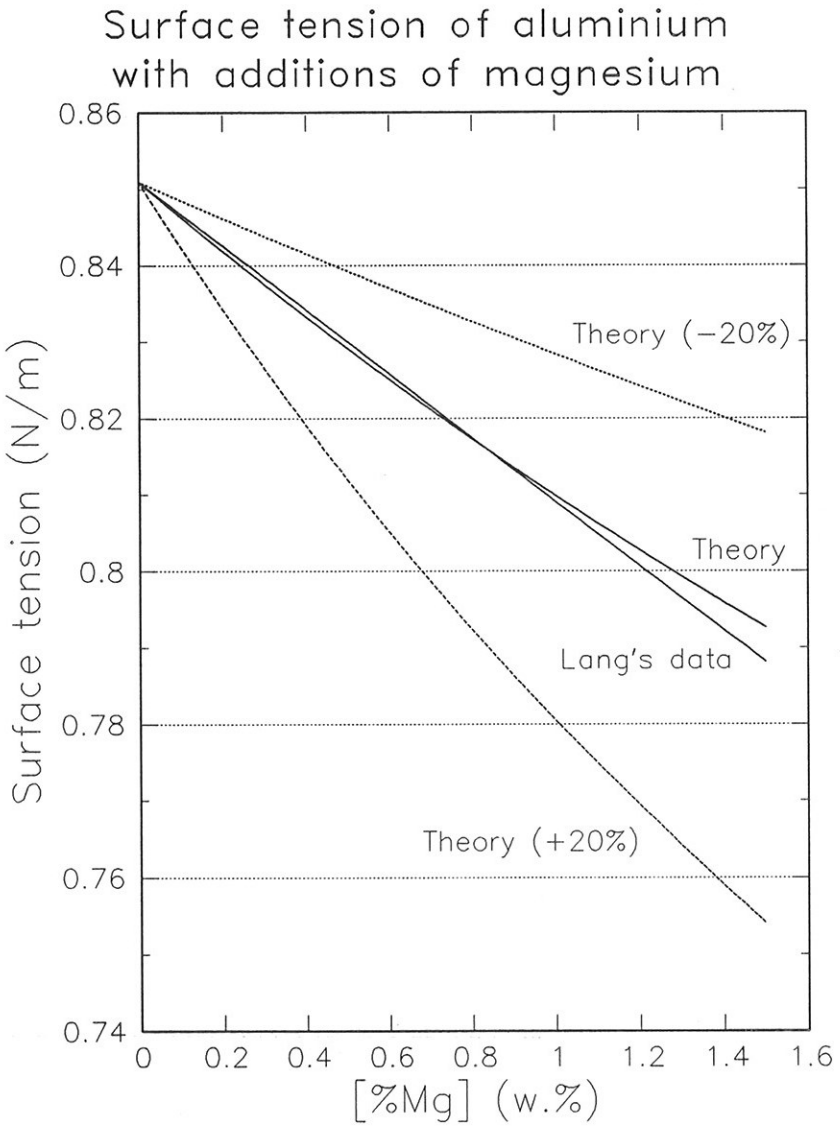

Figure A.12 Surface tension of aluminium with magnesium additions. Curves for free energy of adsorption 20 % too high and too low are shown.

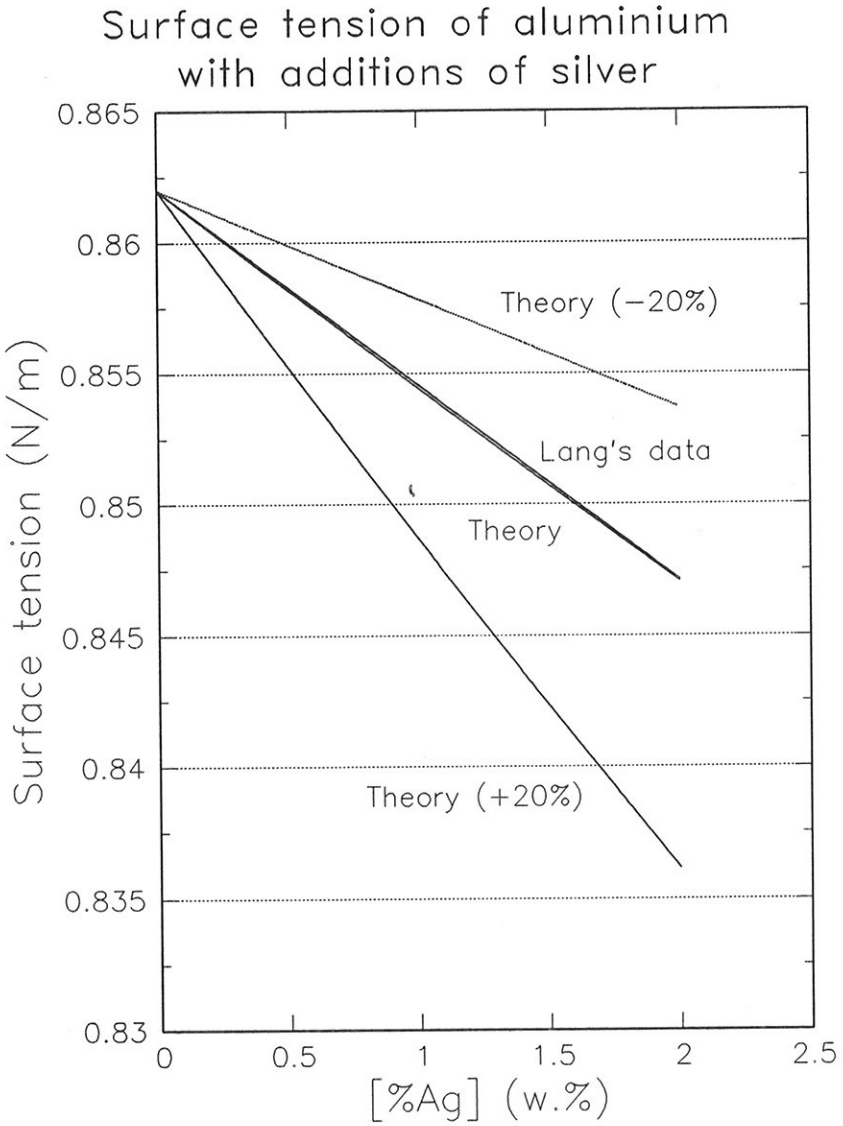

Figure A.13 Surface tension of aluminium with silver additions. Curves for free energy of adsorption 20 % too high and too low are shown.

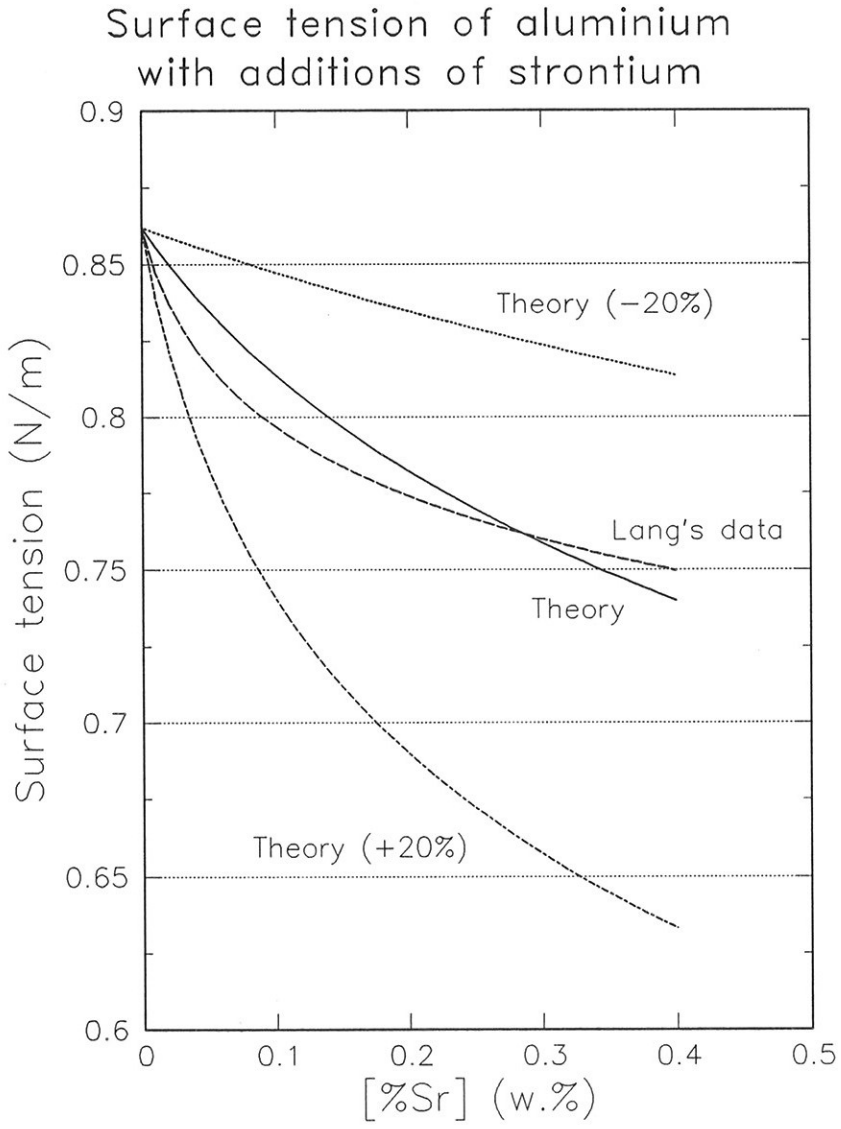

Figure A.14 Surface tension of aluminium with strontium additions. Curves for free energy of adsorption 20 % too high and too low are shown.

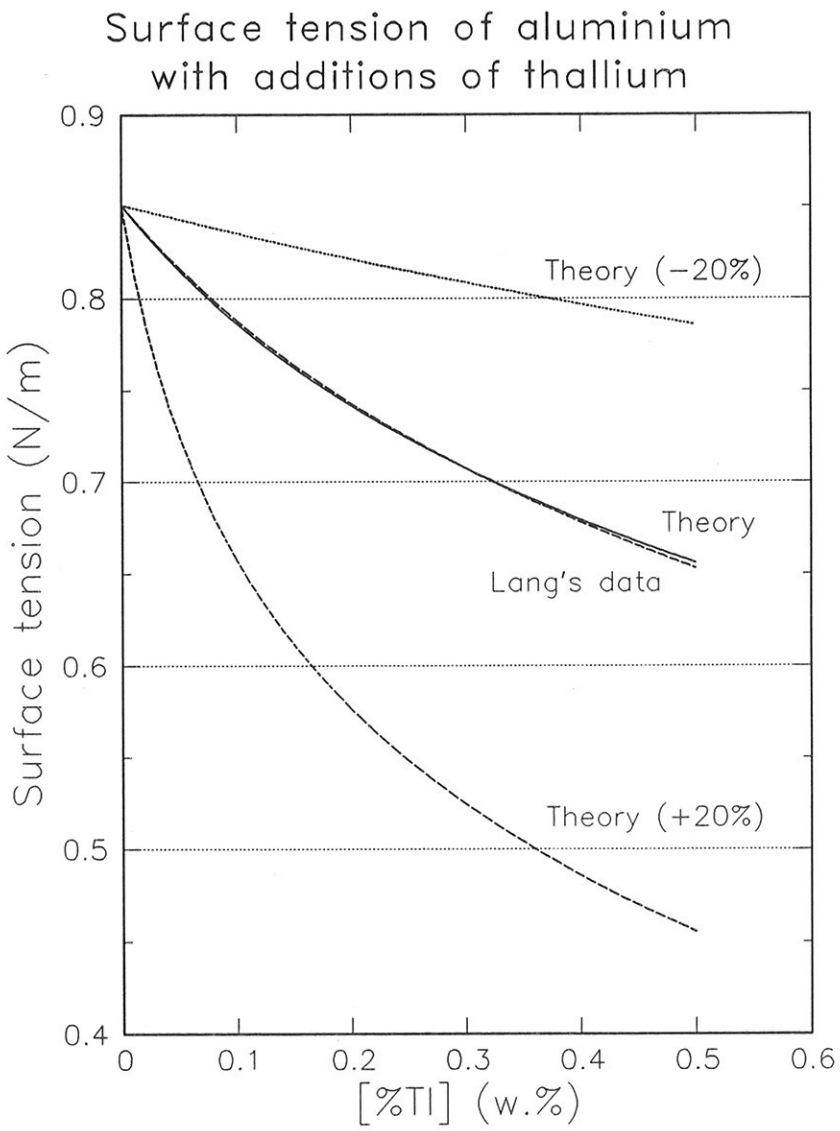

Figure A.15 Surface tension of aluminium with thallium additions. Curves for free energy of adsorption 20 % too high and too low are shown.

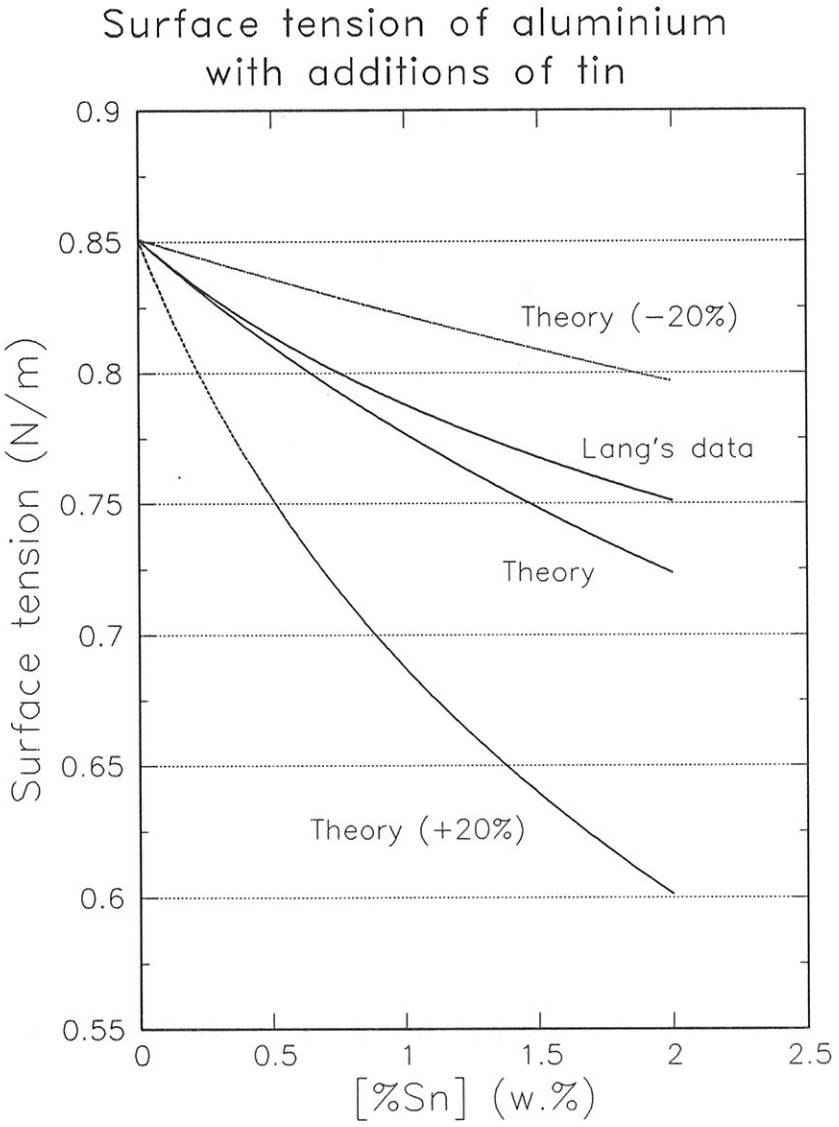

Figure A.16 Surface tension of aluminium with tin additions. Curves for free energy of adsorption 20 % too high and too low are shown.

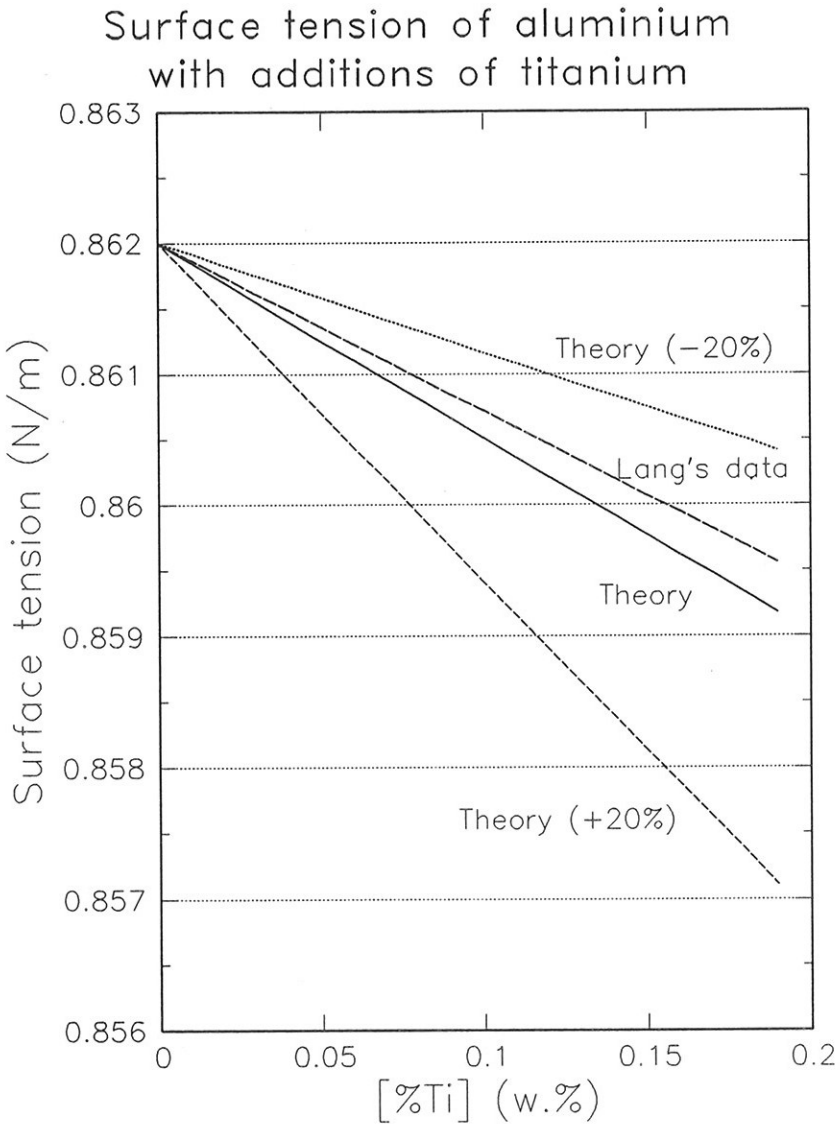

Figure A.17 Surface tension of aluminium with titanium additions. Curves for free energy of adsorption 20 % too high and too low are shown.

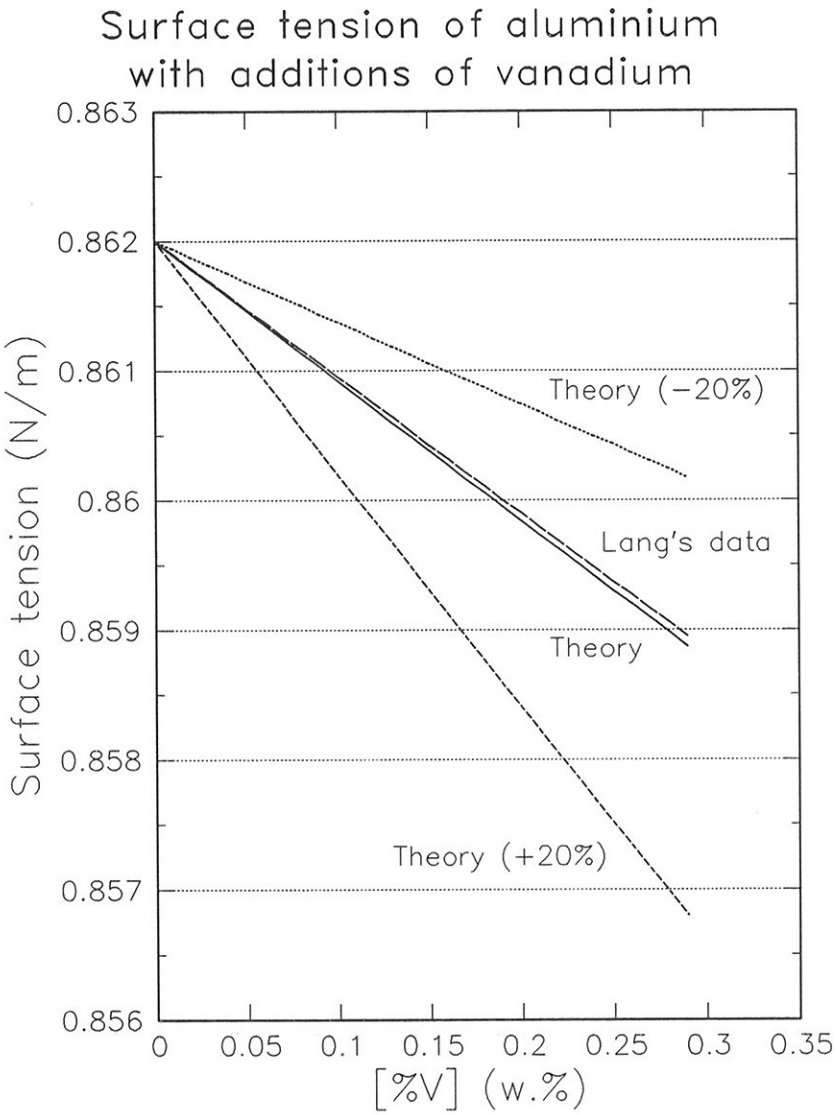

Figure A.18 Surface tension of aluminium with vanadium additions. Curves for free energy of adsorption 20 % too high and too low are shown.

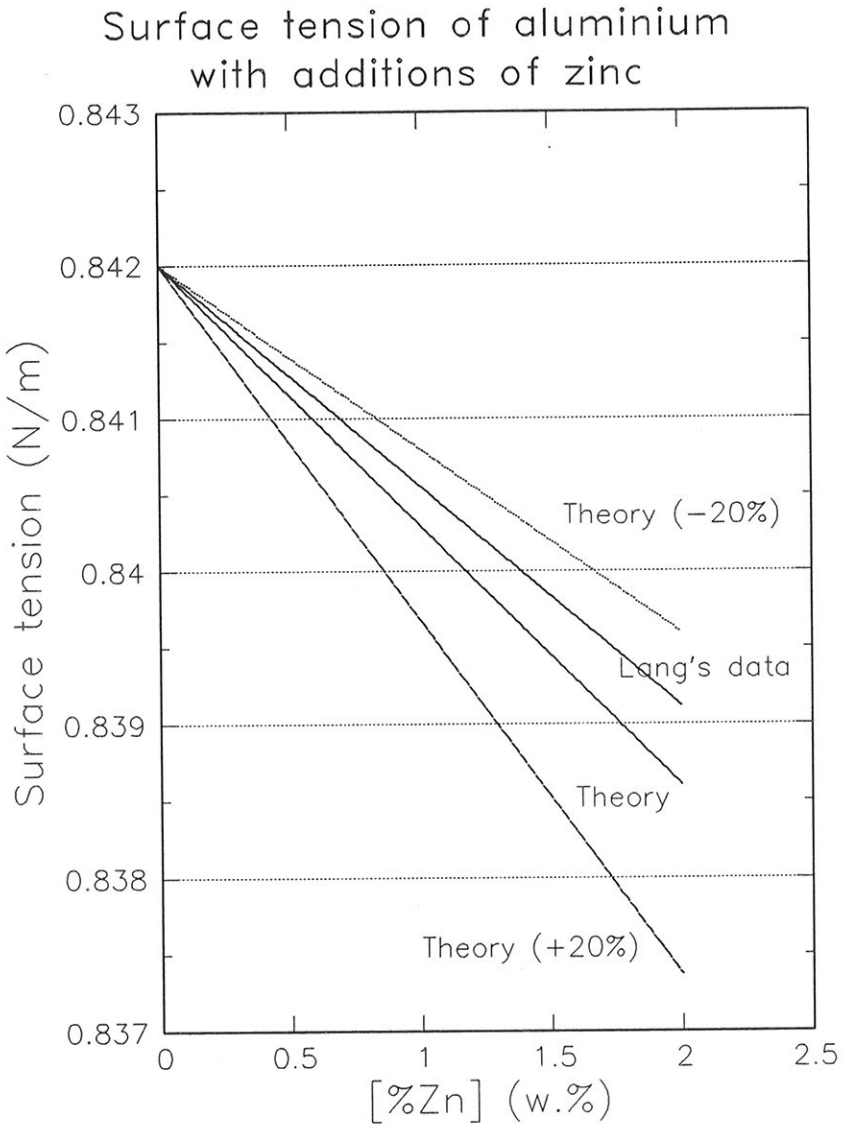

Figure A.19 Surface tension of aluminium with zinc additions. Curves for free energy of adsorption 20 % too high and too low are shown.

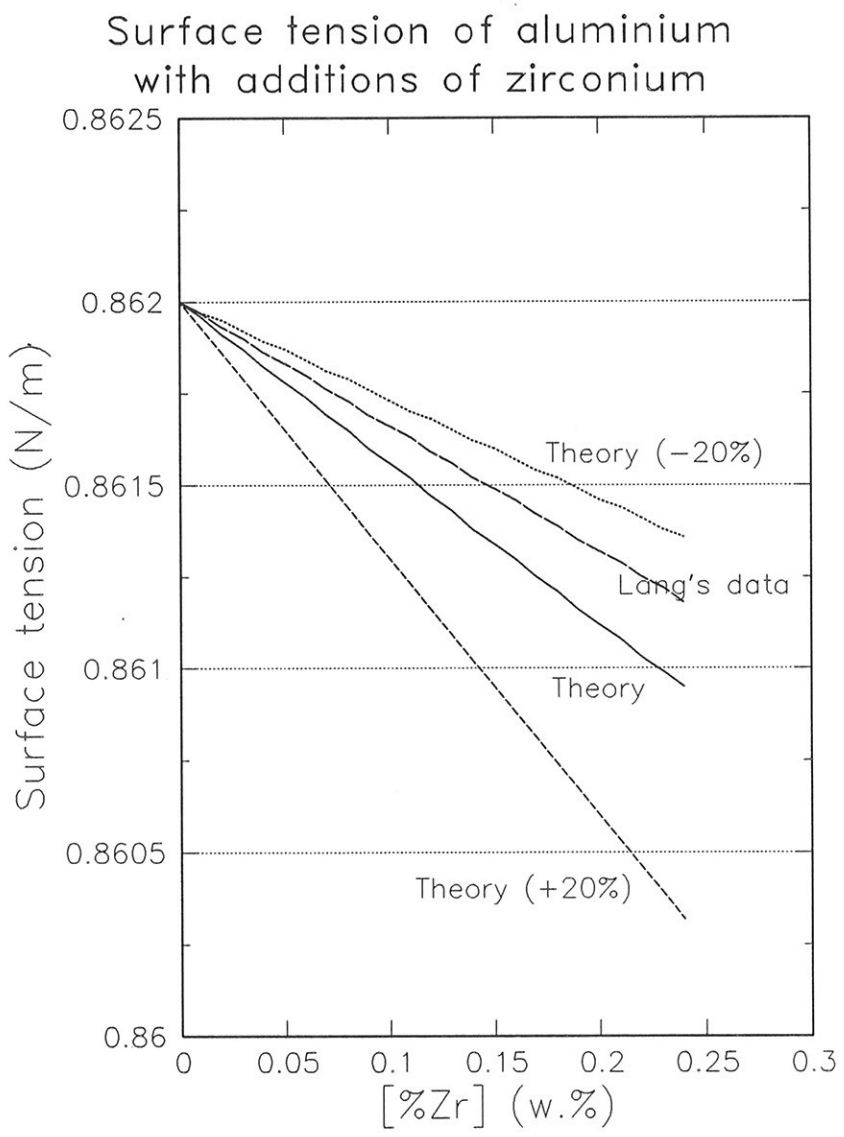

Figure A.20 Surface tension of aluminium with zirconium additions. Curves for free energy of adsorption 20 % too high and too low are shown.

APPENDIX B

Raw data from water model

This appendix contains the raw data from the water model experiments. On the first line the flow velocity is given. The second and third line contains the number of particles entering the filter and then the number of particles deposited on each of the ten collectors. Flow direction is from left to right.

CYLINDRICAL COLLECTORS

0.03 cm/s

53. 6. 6. 8. 2. 2. 6. 2. 3. 2. 0.

58. 3. 6. 6. 5. 4. 2. 2. 4. 1. 1.

0.06 cm/s

62. 11. 6. 6. 2. 2. 4. 2. 2. 1. 0.

70. 6. 9. 2. 10. 3. 6. 4. 4. 1. 0.

0.10 cm/s

70. 4. 4. 9. 3. 2. 5. 3. 2. 2. 5.

74. 4. 13. 6. 4. 2. 1. 3. 1. 2. 2.

0.19 cm/s

78. 4. 2. 2. 5. 1. 3. 3. 2. 0. 3.

79. 3. 5. 3. 3. 5. 1. 0. 2. 1. 2.

0.37 cm/s

87. 1. 2. 1. 2. 0. 5. 1. 1. 0. 2.

86. 2. 1. 1. 1. 1. 1. 2. 2. 0. 1.

0.56 cm/s

86. 1. 1. 0. 0. 0. 0. 0. 1. 1. 0.

86. 1. 0. 1. 3. 0. 0. 0. 1. 0. 0.

0.67 cm/s

83. 1. 2. 0. 0. 4. 0. 0. 2. 2. 0.

82. 1. 0. 0. 2. 0. 1. 0. 0. 2. 0.

0.74 cm/s

87. 0. 1. 0. 1. 0. 0. 1. 1. 1. 1.

88. 1. 0. 2. 2. 0. 4. 3. 1. 0. 1.

0.82 cm/s

72.	1.	1.	2.	4.	0.	3.	2.	1.	2.	2.
74.	2.	1.	0.	3.	1.	1.	0.	2.	0.	2.

0.89 cm/s

73.	1.	2.	0.	2.	1.	2.	3.	2.	1.	1.
76.	3.	2.	3.	2.	1.	1.	0.	2.	0.	1.

0.96 cm/s

74.	0.	3.	1.	1.	2.	0.	0.	1.	0.	1.
72.	1.	2.	2.	1.	1.	0.	1.	0.	1.	3.

1.03 cm/s

72.	1.	0.	2.	2.	1.	1.	1.	3.	2.	1.
75.	0.	5.	1.	1.	1.	0.	1.	0.	0.	1.

1.10 cm/s

63.	2.	2.	0.	0.	0.	4.	1.	0.	2.	3.
70.	1.	2.	1.	4.	0.	1.	1.	2.	0.	1.

SQUARE COLLECTORS

0.03 cm/s

30. 15. 5. 2. 2. 0. 2. 0. 0. 1. 0.
61. 24. 13. 6. 4. 0. 2. 1. 1. 0. 2.

0.06 cm/s

59. 13. 13. 5. 7. 1. 1. 1. 0. 0. 0.
61. 15. 14. 8. 4. 1. 3. 2. 2. 1. 0.

0.11 cm/s

79. 8. 6. 9. 6. 6. 4. 4. 2. 3. 3.
76. 11. 10. 6. 3. 6. 6. 1. 2. 5. 1.

0.19 cm/s

81. 4. 7. 3. 9. 6. 10. 2. 1. 0. 2.
74. 2. 6. 4. 3. 4. 3. 5. 4. 3. 3.

0.37 cm/s

82. 1. 0. 2. 1. 2. 1. 1. 1. 3. 2.
78. 2. 2. 2. 2. 3. 3. 1. 0. 0. 0.

0.56 cm/s

78. 1. 1. 1. 0. 1. 0. 1. 2. 0. 0.
83. 0. 0. 1. 0. 1. 1. 1. 1. 2. 1.

0.67 cm/s

80. 0. 0. 0. 0. 2. 0. 0. 1. 0. 0.
82. 0. 1. 2. 1. 0. 3. 0. 0. 2. 0.

0.74 cm/s

81. 2. 0. 2. 0. 1. 3. 0. 1. 1. 1.
82. 4. 2. 2. 1. 0. 0. 0. 1. 0. 0.

0.82 cm/s

59.	2.	3.	1.	0.	0.	1.	0.	1.	0.	0.
72.	3.	3.	4.	3.	0.	0.	0.	0.	0.	0.

0.89 cm/s

71.	2.	4.	3.	0.	0.	1.	0.	0.	1.	0.
62.	1.	5.	2.	0.	0.	0.	0.	0.	0.	1.

0.96 cm/s

66.	4.	4.	1.	0.	1.	1.	0.	0.	3.	2.
55.	2.	5.	3.	2.	1.	1.	0.	3.	0.	1.

1.03 cm/s

67.	5.	1.	3.	3.	1.	1.	0.	0.	1.	0.
63.	3.	2.	1.	2.	1.	2.	2.	1.	1.	1.